ISBN 0208 189X (print)
ISSN 1736-7492 (electronic)

Oil Shale

CONTENTS

2026 v.43 n.2

Tallinn 2026

International open access scientific journal
of the Estonian Academy of Sciences
published in collaboration with
Tallinn University of Technology
and the Geological Survey of Estonia

Published since 1984

OIL SHALE 2026, Vol. 43, No. 2

Abstracted/indexed in Science Citation Index Expanded (Web of Science), Current Contents – Engineering, Computing & Technology (Web of Science), Scopus, EBSCO, The Gale Group Inc., ProQuest LLC, Airiti Inc., Scilit, Directory of Open Access Journals (DOAJ)

Full texts available at www.eap.ee/oilshale

Executive Editor: Hedi Tõnso, hedi.tonso@eap.ee
Copyeditor: Kadri Põdra
Layout: Ulla Säre
Consultant: Peet M. Sööt (USA), peet@cmmenergy.com

The journal is published quarterly

Printed by Alfapress OÜ, Reti tee 8, 75312 Peetri, Estonia

Oil Shale, 2026, 43, 2, 117–142 https://doi.org/10.3176/oil.2026.2.01

Numerical investigation of oil shale combustion characteristics in a high-low differential velocity CFB boiler using the CPFD model

Hongpeng Liu[(a)], Xuexin Xiang[(a)], Shichao Li[(a)], Shuaishuai Cui[(a)], Chunxia Jia[(a)]*, Hong Qin[(a)], Qing Wang[(a)], Mingzhi Shan[(b)], Bin Liu[(b)], Wen Yang[(c)]

[(a)] Engineering Research Center of Oil Shale Comprehensive Utilization, Ministry of Education, School of Energy and Power Engineering, Northeast Electric Power University, 169 Changchun Road, Jilin 132012, China
[(b)] Victory Shale Oil Retorting Experimental Plant, Fushun Mining Group Co. Ltd., North side of Nanhuang Road, Fushun 113000, China
[(c)] Jiangxi Jianglian Heavy Industry Group Co. Ltd., 999 Aixihu Fourth Road, Nanchang 330000, China

Received 28 September 2025, accepted 8 April 2026, available online 16 April 2026

Abstract. *This study employs the computational particle fluid dynamic model to simulate a 65 t/h oil shale-fired high-low differential velocity circulating fluidized bed (CFB) boiler. The effects of the excess air ratio on furnace temperature, gas composition, particle residence time, and pollutant emissions were analyzed. Results show that an excess air ratio of 1.10 intensifies particle back-mixing, enhancing combustion while reducing NO and SO_2 emissions. The optimal condition combines this ratio with a 1.5:1 main/side bed air distribution, achieving the lowest emissions. This work provides valuable insights for optimizing CFB boiler operation.*

Keywords: *oil shale, high-low differential velocity CFB, gas-solid flow, combustion characteristics, gas pollutants, computational particle fluid dynamics.*

1. Introduction

The high-low differential velocity circulating fluidized bed (CFB) has a unique internal circulation flow and remarkable advantages. Studies show that using a differential air supply in different beds accelerates the disturbance and mixing of materials in the bed. It also has superior advantages, including

* Corresponding author, jiachunxia_215@126.com

wide fuel adaptability, low pollution, and low wear, especially when burning inferior fuels and biomass.

Traditional computational particle fluid dynamics (CPFD) studies have focused on conventional CFB with uniform structures. The innovative high-low differential velocity CFB, featuring differentiated main bed and side beds, enables unique internal circulation and stratified combustion. This represents a shift from homogeneous fluidization to directional flow control, offering new solutions for efficient combustion of low-grade fuels. Compared with conventional CFB, high-low differential velocity CFB has a higher internal mixing efficiency and a more complex internal process. In actual working conditions, large solid particles cannot pass the high-speed bed and enter the low-speed bed. This phenomenon originates from the height difference between the main bed and the side bed, so small fuel particles enter the low-speed bed and combust, thereby reducing the erosion of the flag-shaped heated surface of the buried pipe [1]. Fuel first enters the main bed through side inlets, where its combustion generates a large amount of flue gas and heat. This heat raises the bed temperature and carries most of the small particles into the adjacent low-speed bed. The particles may pass to the working substance in the buried pipe, and finally return to the main bed for heat exchange, while the remaining part of the particles is taken away by the flue gas [2]. This internal circulation process prolongs the residence time of the material in the bed, thereby reducing heat loss and improving combustion and boiler efficiency.

The Barracuda engineering software package is a commercial package, which is developed based on the CPFD method [3]. Compared with the conventional computation fluid dynamics calculation software, this package is mainly focused on the particle phase and can restore the movement of particles in real time. Moreover, CPFD is developed based on the multiphase particle-in-cell (MP-PIC) method [4–6], and Eulerian and Lagrangian methods are used to solve governing equations in fluid and particle phases, respectively.

Abbasi et al. [7] used the CPFD method to study the effects of various operating parameters on the fluid dynamics of the gasifier feed section. The results show that the CPFD method can better predict the particle flow behavior of the gasifier feed section and the gas composition in the furnace. Loha et al. [8] conducted a three-dimensional numerical simulation of a bubbling fluidized bed biomass gasifier using the CPFD method. By adjusting the gasification temperature, equivalence ratio, and the ratio of steam to biomass, the pressure distribution and gas composition were obtained. The results are in good agreement with the experimental data. Ma et al. [9] numerically simulated the influence of different operating conditions on gas hydrodynamics in a high-density CFB using the CPFD method, and found that the number of vents on the riser does not have considerable effect on the solid flux, but does affect the hydrodynamic stability in the riser. Tu et al. [10] used the CPFD method to simulate a complex CFB with six cyclone separators using the Barracuda software to study the gas-solid flow characteristics in

a large-scale system. The results show that the dense region is clear in the bubble state of multiple explosions. Chen et al. [11] used the CPFD method to simulate the risers of the CFB, thus capturing the axial and radial non-uniform flow structure in the risers, revealing the characteristics of the core-annulus flow in the CFB. The calculation results also show that CPFD is more accurate than the two-fluid model with the same drag model, which shows a stronger predictive ability. Liu et al. [12, 13], based on the Barracuda platform, used the CPFD method to simulate the cold and hot states of the CFB test bench, and obtained the gas-solid velocity distribution and temperature distribution. By changing the primary air rate and the mixing ratio of semi-coke and straw, the internal flow and combustion characteristics of the riser were studied, and the ideal operating conditions were obtained.

Wang et al. [14] used the CPFD method to simulate the gas-solid flow in a CFB and analyzed the influence of key model parameters on CPFD simulation in detail. For example, the effects of particle close-packing volume fraction, mesh number, and particle size distribution on the flow in the whole CFB loop were found.

Shi et al. [15, 16] studied the influence of different particle size distributions (PSD) on particle back-mixing behavior during gas-solid flow using the CPFD method, and found that PSD has a significant effect on particle flow behavior in the lower region of the riser tubes, while the PSD effect in the upper region is negligible. Yan et al. [17] proposed a new method to calculate the distribution of coal feed based on the pressure drop and heat balance of a cyclone separator. A 600 MW supercritical CFB boiler was numerically simulated using Barracuda software combined with experimental data. The results show that the method can better predict the combustion characteristics as a boundary condition. It is concluded that the deviation of solid concentration below the furnace caused by the secondary air jet may be the cause of the uneven distribution of primary air velocity in the furnace. Shen et al. [18] analyzed the gas-solid flow and the change of residual coke in a 350 MW CFB boiler under variable working conditions. The study found that, in the load-rising stage, the average value of residual coke in the furnace was significantly higher than that in the boiler start-up stage. In the load-drop stage, the average value of coke was lower than that in the load-rising stage. The combustion rate of residual coke does not match the coal feeding rate under variable load conditions.

The performed literature survey on CFB indicates that most CPFD simulations are focused on conventional CFB, and research on high-low differential velocity CFB boilers is scarce. Moreover, most research on CFB boilers is conducted using Ansys Fluent software. To this end, the CPFD method is applied to simulate the three-dimensional steady-state combustion of a high-low differential velocity CFB boiler. This study fills the gap in research on the combustion characteristics of oil shale fuel in both high- and low-temperature CFB boilers based on the CPFD model.

Unlike conventional CPFD–CFB models for homogeneous structures, this study develops a specialized model for a high-low differential velocity

CFB that reveals their unique particle back-mixing and internal circulation patterns. By coupling asymmetric flow fields with combustion reactions, the model demonstrates how this back-mixing enhances combustion efficiency while reducing pollutants, offering a new methodology and theoretical basis for optimizing such specialized CFB systems. The main contributions of this paper can be summarized as follows:

(1) Fuel combustion in the boiler under different excess air coefficients is analyzed, and the results are compared with those under actual working conditions. The distributions of temperature and gas composition, variations in chemical reactions, and the distribution of particle residence time are obtained, and the excess air coefficient is optimized. This article can provide a reference for studying fluidized bed boilers.

(2) Gas emissions of the boiler under different excess air coefficients are analyzed numerically. Furthermore, the influence of different air volume ratios of the main bed and side beds on the emission of NOx and other pollutant gases is explored. The obtained results are then analyzed under different working conditions to determine the optimal operating conditions.

2. Numerical simulation

2.1. Governing equations

Ignoring interphase mass transfer, the continuity equation for the gas phase can be expressed as follows:

$$\frac{\partial \theta_g \rho_g}{\partial t} + \nabla\left(\theta_g \rho_g u_g\right) = 0, \tag{1}$$

where ρ_g, u_g, and θ_g are the density, velocity, and volume fraction of the gas phase, respectively.

The momentum conservation equation for the gas phase is as follows:

$$\frac{\partial \theta_g u_g}{\partial t} + \nabla\left(\theta_g u_g u_g\right) = -\frac{1}{\rho_g}\nabla P - \frac{1}{\rho_g} F + \theta_g g + \frac{1}{\rho_g}\nabla \tau, \tag{2}$$

where P and F are the pressure and macroscopic stress tensor of the gas phase, respectively, and τ is the unit volume momentum exchange rate between the gas phase and the particle phase.

The stress tensor F can be calculated using the following expression:

$$F = \iiint f V_p \rho_p \left[D\left(u_g - u_p\right) - \frac{1}{\rho_p}\nabla P \right] dV_p d\rho du_p . \tag{3}$$

The momentum equation of the particle phase is as follows:

$$\frac{du_p}{dt} = D\left(u_g - u_p\right) - \frac{1}{\rho_p}\nabla P + g - \frac{1}{\theta_p \rho_g}\nabla \tau_p, \tag{4}$$

where u_p, ρ_p, and τ_p denote the velocity, density, and normal stress of the particle phase, respectively.

Equations (1–4) show the generated acceleration originating from the combined action of aerodynamic drag, pressure gradient, gravity, and normal stress gradient between particles. In each grid, the volume fraction of particles is as follows:

$$\theta_p = \iiint f V_p d\rho_p du_p. \tag{5}$$

In the present study, the interparticle collision is calculated using the normal stress model:

$$\tau = \frac{P_s \theta_p^{\beta}}{\max\left[\left(\theta_{cp} - \theta_p\right), \varepsilon\left(1 - \theta_p\right)\right]}, \tag{6}$$

where P_s is the material parameter, $2 < \beta < 5$ is the model parameter [19], θ_{cp} is the volume fraction of particle dense packing and ε is a quantity constructed to eliminate singular points in the model [20].

2.2. Calculation of particle properties

In the Barracuda software, it is assumed that particles are spherical, and the particle radius is calculated using the following expression:

$$r_{\text{particle}} = \left(\frac{3}{4\pi} V_{\text{particle}}\right)^{1/3}. \tag{7}$$

Due to the combustion of pulverized coal pyrolysis and volatile fraction, the particle density may change. Consequently, the following method is used in the calculations:

$$m_{\text{particle}} = \sum_i m_{\text{volatile},i} + \sum_i m_{\text{volatile},i}, \tag{8}$$

$$V_{\text{particle}} = \sum_i v_{\text{solid},i} + \sum_i v_{\text{volatile},i}, \tag{9}$$

where $m_{\text{volatile},i}$ and $v_{\text{volatile},i}$ are the mass and volume of the i-th volatile fraction, respectively. Moreover, $m_{\text{solid},i}$ and $v_{\text{solid},i}$ are the mass and volume of the i-th particle, respectively.

The particle density is defined as follows:

$$\rho_{\text{particle}} = \frac{m_{\text{particle}}}{V_{\text{particle}}}, \tag{10}$$

$$v_{\text{solid},\,i} = \frac{m_{\text{solid},i}}{\rho_{\text{solid},i}}. \tag{11}$$

It should be indicated that, during the volatilization process, the fuel releases a large amount of gas after heating. Based on the Arrhenius equation, the reaction rate can be expressed as follows:

$$k = c0T^{C1}P^{C2}\rho_f^{c3}\exp(-E/T + E_0), \tag{12}$$

where T is the temperature, P denotes the pressure, ρ_f is the fluid density, and E is the activation energy.

Meanwhile, the volatile fraction release rate can be calculated as follows:

$$\frac{\mathrm{d}m_{\text{volatile}}}{\mathrm{d}t} = -km_{\text{volatiles}}. \tag{13}$$

2.3. Drag model

The trapping forces of the fluid and particle phases are defined as follows:

$$D_{\text{s}} = C_{\text{d}}\frac{3}{8}\frac{\rho_g}{\rho_s}\frac{|u_{\text{f}} - u_{\text{s}}|}{r_{\text{s}}}, \tag{14}$$

where u_{f} and u_{s} are the velocity vectors of the fluid and particle phases, respectively, and D_{s} is the traction function.

In the Barracuda software, drag models include the WenYu model, the Ergun model, the WenYu–Ergun model, and the EMMS model. The EMMS model employs a non-uniform drag model, simplifying the actual complex particle clusters into sparse, regular spherical particle clusters. It is more suitable for Geldart Class A particles, achieving higher simulation accuracy for this particle type. However, the particle size distribution in CFB boilers more closely resembles that of Geldart Class B particles, making it difficult to form agglomerates similar to those of Geldart Class A particles. This may lead to reduced model accuracy, rendering the EMMS model unsuitable for CFB boiler simulations.

The WenYu–Ergun model combines the strengths of both the WenYu and Ergun models, offering excellent simulation accuracy for particles of varying sizes. It effectively simulates the distribution between the dense-phase and dilute-phase zones in CFB boilers. Therefore, the WenYu–Ergun gas–solid drag model is used for the calculations. This drag model can accurately predict the flow characteristics within the CFB 14.

The WenYu–Ergun drag model is expressed as follows:

$$\theta_p > 0.85\theta_{cp} \qquad D = D_p^2, \tag{15}$$

$$\theta_p < 0.75\theta_{cp} \qquad D = D_p^1, \tag{16}$$

$$0.85\theta_{cp} \geq \theta_p \geq 0.75\theta_{cp} \quad D = \frac{\theta_p - 0.85\theta_{cp}}{0.85\theta_{cp} - 0.75\theta_{cp}}\left(D_p^2 - D_p^1\right) + D_p^1, \tag{17}$$

where D_p^1 and D_p^2 are the coefficients of the WenYu and Ergun models, respectively.

2.4. Simulation of chemical reaction

Take the following chemical reaction as an example:

$$C(s) + H_2O \rightarrow CO + H_2, \tag{18}$$

$$R = 219\frac{m^3}{kg \bullet K \bullet s} T \exp(-\frac{22645\text{K}}{\text{T}})\rho_c[H_2O], \tag{19}$$

where T is the temperature, ρ_c is the density of carbon particles, and $[H_2O]$ denotes the volume concentration of H_2O.

The concentration changes of reactants and products in these reactions can be calculated by solving the following differential equations:

$$k_0 = 219\frac{m^3}{kg \bullet K \bullet s} T \exp(-\frac{22645K}{T})\rho_c, \tag{20}$$

$$\frac{d[C(s)]}{dt} = -219\frac{m^3}{kg \bullet K \bullet s} T \exp(-\frac{22645\text{K}}{\text{T}})\rho_c[H_2O], \tag{21}$$

$$\frac{d[H_2O]}{dt} = \frac{d[C(s)]}{dt} \qquad \frac{d[CO]}{dt} = -\frac{d[C(s)]}{dt}, \tag{22}$$

$$\frac{d[H_2]}{dt} = -\frac{d[C(s)]}{dt}. \tag{23}$$

The chemical reaction rate is as follows:

$$r = k_0[H_2O]. \tag{24}$$

The chemical reaction rate constant is the following:

$$k_0 = 219\frac{m^3}{kg \bullet K \bullet s} T \exp(-\frac{22645K}{T})\rho_c. \tag{25}$$

The equivalent chemical equation is as follows:

$$C(s) + H_2O \rightarrow CO + H_2. \tag{26}$$

2.5. Calculation of wall radiation heat transfer

In the Barracuda software, only the radiative heat transfer between the wall and the particles near the wall is considered in calculations, while the radiative heat transfer between particles and the radiative heat transfer between the fluid and the wall are ignored. This can be expressed as follows:

$$q_{\mathrm{wp}} = A_{\mathrm{w}} F_{\mathrm{wp}} \varepsilon_{\mathrm{wp}} \sigma (T_{\mathrm{w}}^4 - T_{\mathrm{p}}^4) \ , \tag{27}$$

where A_{w} is the wall area, T_{w} is the wall temperature, T_{p} denotes the average particle temperature within a calculation cell, F_{wp} is the calculated view factor, σ is the Boltzmann constant, and $\varepsilon_{\mathrm{wp}}$ is the effective emissivity between wall and particle.

The expression for $\varepsilon_{\mathrm{wp}}$ is as follows:

$$\varepsilon_{\mathrm{wp}} = (\frac{1}{\varepsilon_{\mathrm{p}}} + \frac{1}{\varepsilon_{\mathrm{w}}} - 1)^{-1} \ , \tag{28}$$

where ε_{w} is the wall emissivity and ε_{p} denotes the volume-weighted average particle emissivity.

2.6. Calculation of convective heat transfer

The convective heat transfer coefficient between the wall and the fluid, the heat transfer coefficient in the dense-phase region, and the heat transfer coefficient between the fluid and the particles are calculated using the following equations.

The convective heat transfer coefficient between the fluid and the wall is as follows:

$$h = (1 - f_d) h_1 + f_d h_d \ , \tag{29}$$

where h_1 and h_d are the heat transfer coefficients of the dilute phase and the particle phase, respectively, f_d is the time-averaged proportion of the wall surface covered by the particle phase, k_f is the thermal conductivity of the fluid, L is the length of a single grid, and μ_f is the fluid viscosity.

The above-mentioned parameters can be determined using dimensionless numbers [21]:

$$\frac{h_1 L}{k_f} = Nu_1 = 0.546 \mathrm{Re}_1 + 3.66 \ , \tag{30}$$

$$\mathrm{Re}_1 = \frac{\rho_g u_g L}{\mu_f} . \tag{31}$$

The convective heat transfer coefficient in the dense phase is given by the following:

$$\frac{h_d d_p}{k_f} = Nu_d = 0.525 \mathrm{Re}_1^{0.75} , \tag{32}$$

$$f_d = 1 - e^{-10 \frac{\theta_p}{\theta_{cp}}} . \tag{33}$$

The convective heat transfer coefficient between the particles and the gas is given as follows [22]:

$$\frac{h_p d_p}{k_f} = Nu_p = 0.37\,\mathrm{Re}_p^{0.6} + 0.1, \tag{34}$$

$$\mathrm{Re}_p = \frac{\rho_g u_g d_p}{\mu_f}. \tag{35}$$

3. Boiler structure, initial conditions, and boundary conditions

In the present study, a 65-t/h high-low differential velocity CFB is considered as the research object. The simulation model is shown in Figure 1.

The model mainly consists of a boiler chamber, two feed ports, 16 secondary air nozzles, and a water wall. It uses primary and secondary air flows to supply high- and low-speed beds, respectively. Furthermore, it consumes Maoming oil shale as fuel. The results of the proximate and ultimate analyses of the fuel are shown in Table 1.

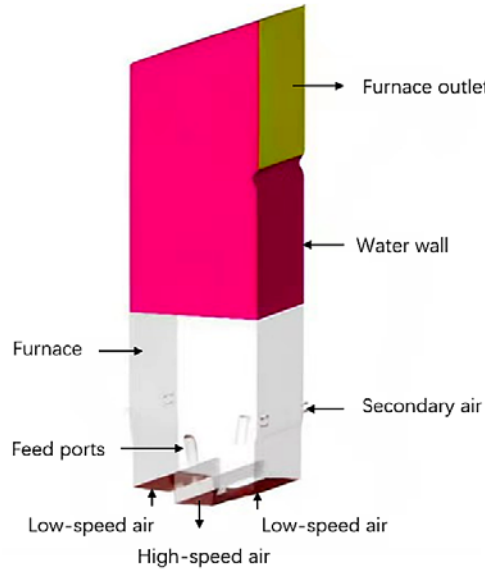

Fig. 1. Schematic diagram of the computational model.

Table 1. Proximate and ultimate analyses of Maoming oil shale

Proximate analysis, %				Low heat value, MJ/kg	Ultimate analysis, %				
M_{ar}	V_{ar}	A_{ar}	FC_{ar}	$Q_{net,ar}$	C_{ar}	H_{ar}	O_{ar}	N_{ar}	S_{ar}
18.10	16.51	62.99	2.40	4.1	9.70	1.65	6.12	1.08	0.36

Abbreviations: M_{ar} – moisture, as-received basis; V_{ar} – volatile matter, as-received basis; A_{ar} – ash content, as-received basis; FC_{ar} – fixed carbon, as-received basis; $Q_{net,ar}$ – net calorific value, as-received basis; C_{ar} – carbon, as-received basis; H_{ar} – hydrogen content, as-received basis; O_{ar} – oxygen content, as-received basis; N_{ar} – nitrogen content, as-received basis; S_{ar} – sulfur content, as-received basis.

The particle size distribution is shown in Figure 2. The bed material is shale ash with a height of 400 mm. In the initial phase, the material accumulates at the bottom of the furnace. The oil shale enters the high-speed bed through both sides of the furnace, while the airflow enters the furnace from the bottom of the bed. The bed material begins to fluidize, and the bed material is continuously discharged from the outlet simultaneously. Finally, the furnace reaches steady-state conditions. Figure 3 shows the variations of the gas mass fraction at the furnace outlet. It is observed that fluctuations of the gas mass fraction at the outlet are small after 25 seconds. Accordingly, the results are averaged over the time period of 25–45 s. The time-averaged values of the corresponding physical quantities are used to analyze the results.

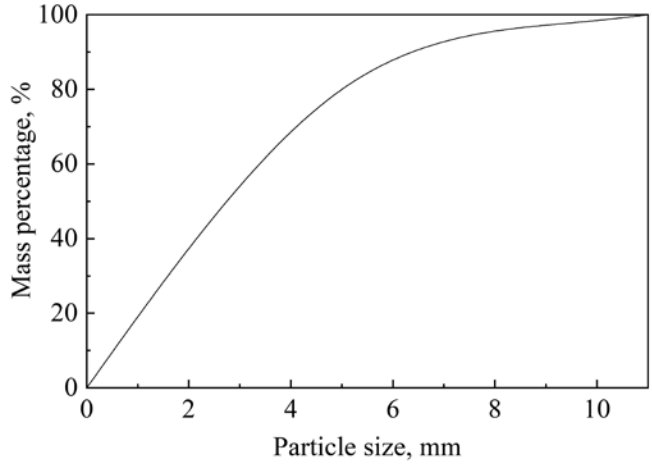

Fig. 2. Particle size distribution of Maoming oil shale.

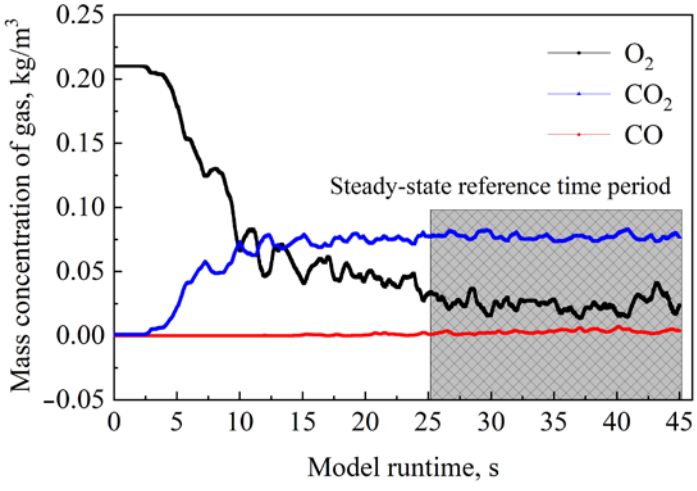

Fig. 3. Outlet gas mass concentration vs time.

The simulated operating conditions are shown in Table 2. The chemical reactions and rate equations are presented in Table 3 [23–27].

Table 2. Simulation conditions

Case	Excess air coefficient a	Feed quantity, kg/h
1	1.10	39265
2	1.15	39265
3	1.20	39265

Table 3. Chemical reaction equations and reaction rates

Reaction equations	Reaction rate, $mol \cdot m^{-3} \cdot s^{-1}$
Heterogeneous reaction	
$C(s) + H_2O \rightarrow CO + H_2$	$r_1 = 1.272 m_s T \exp(-22645/T)[H_2O]$
$C + CO_2 \rightarrow 2CO$	$r_2 = 1.272 T \exp(-22645/T)[CO_2]$
$2C(s) + O_2 \rightarrow 2CO$	$r_3 = 1.47 \times 10^5 \theta_p T \exp(-13590/T)[O_2]$
$CO + H_2 \rightarrow C(s) + H_2O$	$r_4 = 1.04 \times 10^{-4} m_s T^2 \exp(-6319/T - 17.29)[CO][H_2]$
$2CO \rightarrow CO_2 + C(s)$	$r_5 = 1.04 \times 10^{-4} m_s T^2 \exp(-2363/T - 20.92)[CO]$
Homogeneous gas phase reaction	
$CO + 0.5O_2 \rightarrow CO_2$	$r_6 = 5.62 \times 10^{12} \exp(-16000/T)[CO][O_2]$
$CO + H_2O \rightarrow CO_2 + H_2$	$r_7 = 7.68 \times 10^{10} \exp(-36640/T)[H_2O][CO]$
$CH_4 + O_2 \rightarrow CO_2 + 2H_2$	$r_8 = 3.552 \times 10^{11} T^{-1} \exp(-15700/T)[CH_4][O_2]$
Reaction of nitrides with sulfides	
$H_2S + 1.5O_2 \rightarrow SO_2 + H_2O$	$r_1 = 5.2 \times 10^8 \exp(-2321/T)[H_2S][O_2]$
$NH_3 + 1.25O_2 \rightarrow NO + 1.5H_2O$	$r_2 = 3.1 \times 10^8 \exp(-25000/T)[NH_3][O_2]$
$NO + CO \rightarrow 0.5N_2 + CO_2$	$r_3 = K_3 \dfrac{K_{3a}[NO](K_{3b}[CO] + K_{3C})}{K_{3a}[NO] + K_{3b}[CO] + K_{3C}}$ $K_3 = 1.952 \times 10^7 \exp(-25000/T)$ $K_{3a} = 18.26\ K_{3b} = 7.86\ K_{3c} = 0.002531$
$HCN + 0.75O_2 \rightarrow CNO + 0.5H_2O$	$r_4 = 2.14 \times 10^8 \exp(-10000/T)[HCN][O_2]$

Continued on the next page

Table 3. *Continued*

Reaction equations	Reaction rate, mol·m^{-3}·s^{-1}
CNO + 0.5O_2 → NO + CO	$r_5 = K_5 \frac{K_{5a}}{K_{5a} + K_{5b}[NO]}[HCN][O_2]$ $K_5 = 2.14 \times 10^8 \exp(-10000/T)$ $K_{5a}/K_{5b} = 1.02 \times 10^{12} \exp(-25499/T)$
CNO + NO → N_2O + CO	$r_6 = K_6[HCN][O_2]\frac{K_{6a}[NO]}{K_{6a} + K_{6b}[NO]}$ $K_{6a}/K_{6b} = 1.02 \times 10^{12} \exp(-25499/T)$
N_2O + CO → N_2 + CO_2	$r_7 = 1.24 \times 10^9 \exp(-5913/T)[N_2O][CO]$
N_2O + 0.5O_2 → N_2+O_2	$r_8 = 1.5 \times 10^{11} \exp(-20159/T)[N_2O][O_2]$
NH_3 + 0.75O_2 → 0.5N_2 + 1.5H_2O	$r_9 = 4.96 \times 10^8 \exp(-10000/T)[NH3][O_2]$
2NH_3 + 3NO → 2.5N_2 + 3H_2O	$r_{10} = 1.1 \times 10^{12} \exp(-27676/T)[NH3]^{0.5}[O_2]^{0.5}[NO]^{0.5}$
N_2O + C → N_2 + CO	$r_{11} = 2.9 \times 10^9 \exp(-1711/T)[N_2O]$
NO + C → 0.5N_2 + CO	$r_{12} = 5.85 \times 10^7 \exp(-12000/T)[NO]$
NO + 0.5C → 0.5N_2 + 0.5C_O2	$r_{13} = 1.3 \times 10^5 \exp(-1712/T)[NO]$

The performance of the developed model can be evaluated by comparing the numerical results of Case 2 with the field test data. A grid-independent test is conducted based on three mesh sizes, and the comparison between the calculated T_{ll}, T_{rl}, and T_h (T_{ll} denotes left low-speed bed, T_{rl} denotes right low-speed bed, T_h denotes high-speed bed) and the measured values are shown in Table 4.

Table 4. Comparison of simulated and experimental temperatures for different grids

Grid category	Mesh number	Simulated value T_{ll}	Test value T_{ll}	Simulated value T_h	Test value T_h	Simulated value T_{rl}	Test value T_{rl}	Average error
Coarse	67452	687 °C	760 °C	689 °C	747 °C	679 °C	761 °C	9.3%
Medium	85932	707 °C	760 °C	711 °C	747 °C	695 °C	761 °C	8.2%
Fine	95172	716 °C	760 °C	718 °C	747 °C	698 °C	761 °C	5.9%

On-site test data exhibit a certain degree of measurement uncertainty. The uncertainty in thermocouple temperature measurements primarily stems from the thermocouple's inherent accuracy (±2.5 °C), radiation errors, and temperature fluctuations within the furnace. The combined uncertainty is estimated to be approximately ±15 °C. However, the overall error remains within the specifications outlined in the test procedures.

Table 4 presents the comparison between simulated temperatures and measured values under three mesh configurations. As the number of mesh cells increased from 67452 to 95172, the simulated main bed temperature (T_{ll}) rose from 687 °C to 716 °C, while the deviation from the measured value (760 °C) decreased from 9.6% to 5.8%. This indicates that the simulation results exhibit sensitivity to grid resolution, particularly when capturing complex gas–solid flow in the dense-phase zone at the bottom. The ultimately selected medium grid scheme (85932) significantly conserves computational resources while maintaining accuracy, with an average error of 8.2%, within an engineering-acceptable range.

4. Results and discussion

4.1. Combustion characteristics

4.1.1. Temperature distribution

Figures 4 and 5 show the time-averaged temperature distribution of gas and particles with an excess air coefficient of 1.15. It is observed that the fluid temperature near the feed ports in the dense-phase zone of the furnace

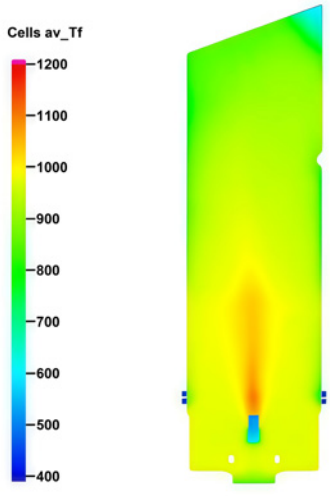

Fig. 4. Time-averaged temperature distribution of the combustion gas (showing higher temperatures near the feed ports in the dense-phase zone).

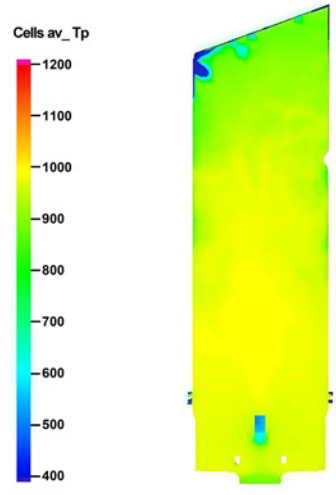

Fig. 5. Time-averaged temperature distribution of particles (illustrating lower temperatures than the surrounding gas near the feed ports).

is higher than the particle temperature, with the maximum temperature difference reaching 100 °C. In the dilute-phase region, the fluid temperature and particle temperature are relatively uniform, with a temperature difference of approximately 20 °C. This is because the oil shale contains fewer volatile components, so combustion occurs in the gas phase. Due to the lower specific heat capacity of gas, its temperature increases faster. In this regard, Table 4 indicates that the calculated furnace temperature is lower than the actual operating temperature. Meanwhile, the measured temperature from thermocouples has some uncertainties. The calculation error is within the allowable range, so the model is verified to predict temperatures with reasonable accuracy.

4.1.2. Chemical reaction rate

In order to simplify the calculations, a simplified model is used to simulate the chemical reactions. Figure 6(a)–(i) shows the reaction rates of different simplified models in the fluidized bed furnace with an excess air coefficient of 1.15. It is found that all heterogeneous reaction rates in the reactor at a height of 4 m, at the bottom of the bed, and at the oil shale inlet approach 0. The C–O_2 combustion provides heat for gasification, so the rates of the gasification reactions C–H_2O and C–CO_2 are relatively large. For the homogeneous reaction rate, the combustion reactions of CO and CH_4 are the most stable in the whole furnace, and these reactions mainly occur at heights near the feed ports.

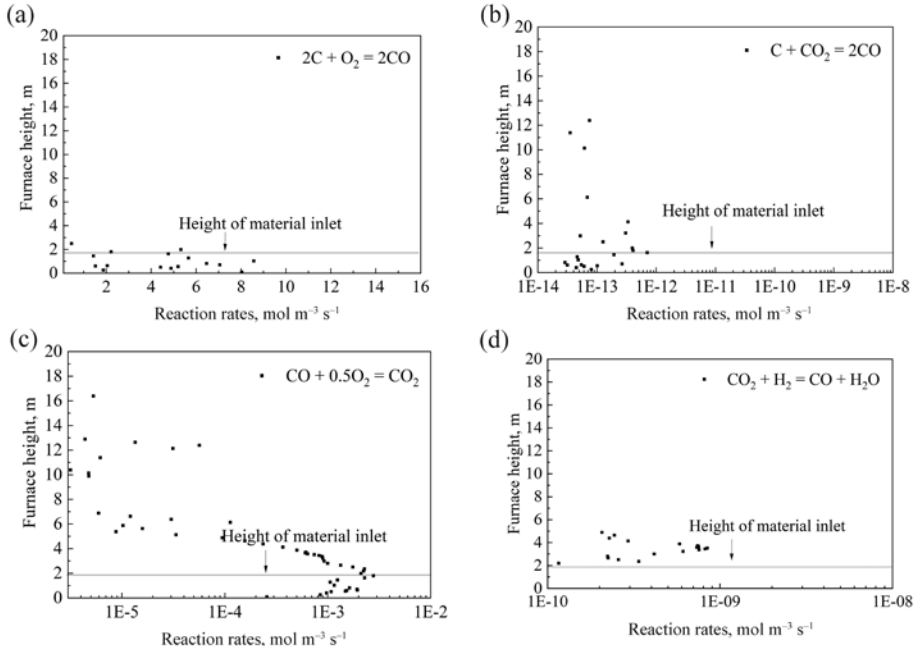

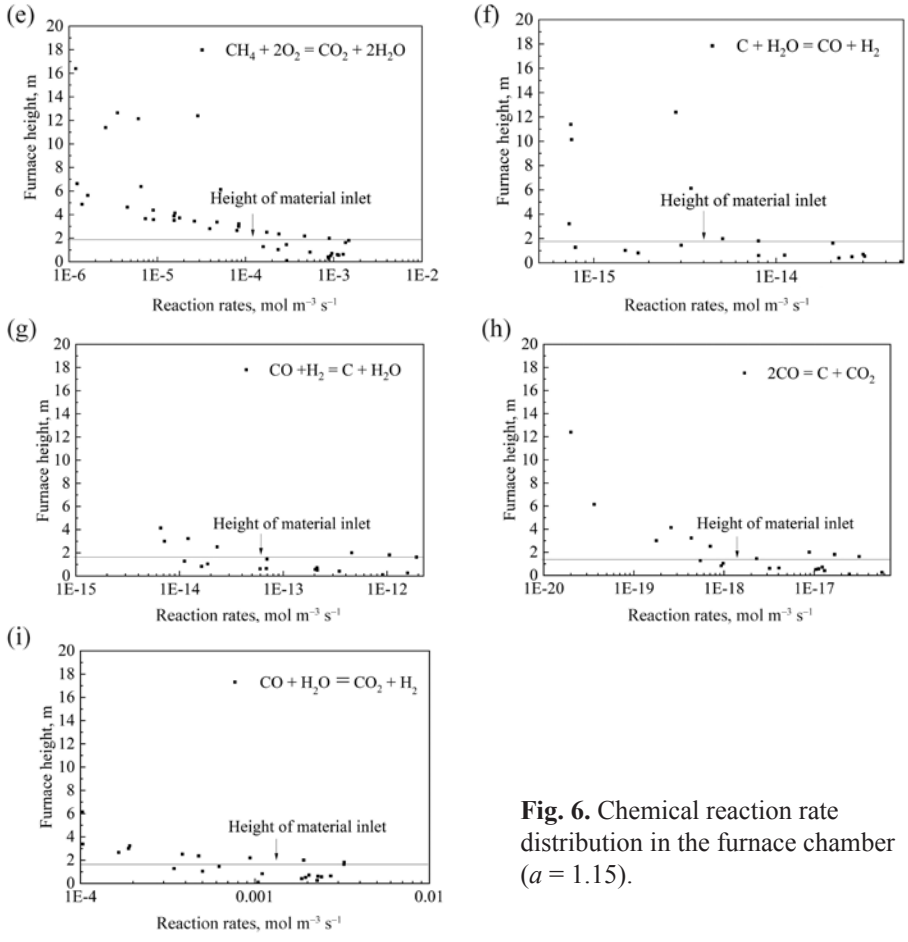

Fig. 6. Chemical reaction rate distribution in the furnace chamber (a = 1.15).

4.1.3. Particle residence time

In order to obtain the degree of particle back-mixing, the residence time distribution (RTD) density function E(t) of particles in the furnace under different excess air ratios is shown in Figure 7. It is observed that the distribution has a spike and also exhibits a certain trailing phenomenon, which indicates that the particles are close to plug flow. However, due to the exchange between particles, the average residence time is larger than that of plug flow. Considering the strong downward flow of particles at the bed wall, the residence time distribution has a late peak and pronounced trailing [16].

When a is small (1.10), the primary air volume is relatively low, resulting in a lower gas velocity in the dense-phase zone at the bed bottom. This makes it more difficult to lift large particles, facilitating the formation of intense

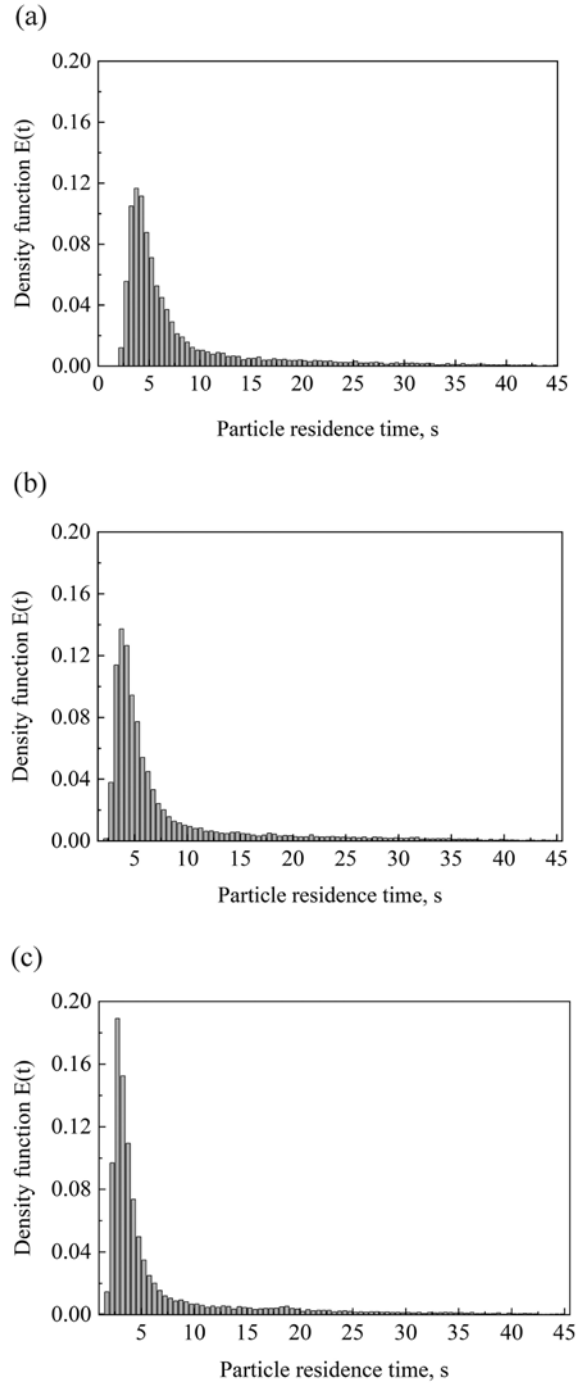

Fig. 7. Particle residence time distribution under different excess air ratios: a = 1.10 (a); a = 1.15 (b); a = 1.20 (c).

vortices and recirculation at the bottom, which leads to more severe back-mixing. When *a* is large (1.20), the primary air volume increases, raising the overall gas velocity. The enhanced penetration of the gas flow allows more particles to be directly entrained upward, reducing the opportunity for particles to linger and circulate at the bottom. Consequently, the degree of back-mixing is mitigated.

Figure 8 illustrates the spatial distribution of particle residence time. It is challenging to compare the spatial distribution of particle residence times based solely on figures. For example, particles in the dense-phase zone of the bed have a higher residence time, while particles in the dilute-phase zone have a lower residence time. This is mainly because the large particles in the dense-phase zone require more time to transition to the dilute-phase zone. Particles with smaller sizes in the dilute-phase zone leave the furnace quickly, and the residence time of particles just entering the fuel inlet is relatively short.

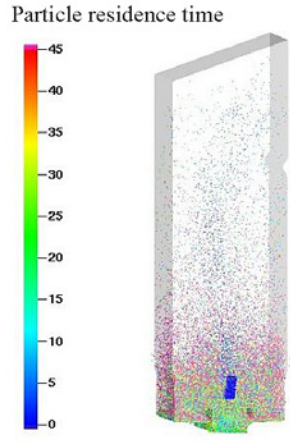

Fig. 8. Spatial distribution of particle residence time (a = 1.15).

Figure 9 show the cumulative distribution function F(t) curves of particle residence time under different excess air ratios. It is worth noting that the ideal plug-flow F(t) curve is a vertical line, and the smaller the slope of the F(t) curve, the higher the degree of back-mixing [28]. The results indicate that when a = 1.10, the back-mixing behavior is more intense and more favorable for combustion. Therefore, it is recommended to use 10% excess air in engineering processes.

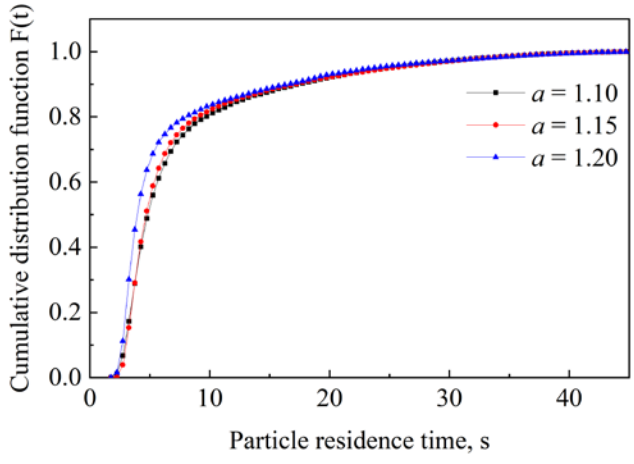

Fig. 9. Cumulative distribution of particle residence time.

4.1.4. Gas distribution

Figure 10 shows the concentration distribution of O_2 and CO_2 in the furnace at different excess air ratios after the model has run for 45 s. Inside the furnace, a small portion of CO_2 gas originates from the primary and secondary air, while the main part is produced by combustion. In the dense zone at the bottom of the furnace, a large number of oil shale particles burn, which results in areas with low O_2 concentrations and relatively high CO_2 concentrations. Although the injection of secondary air in the dilute-phase zone increases the O_2 concentration along the furnace height, its weak diffusion results in poor mixing efficiency, consequently forming a low-temperature zone near the air inlet.

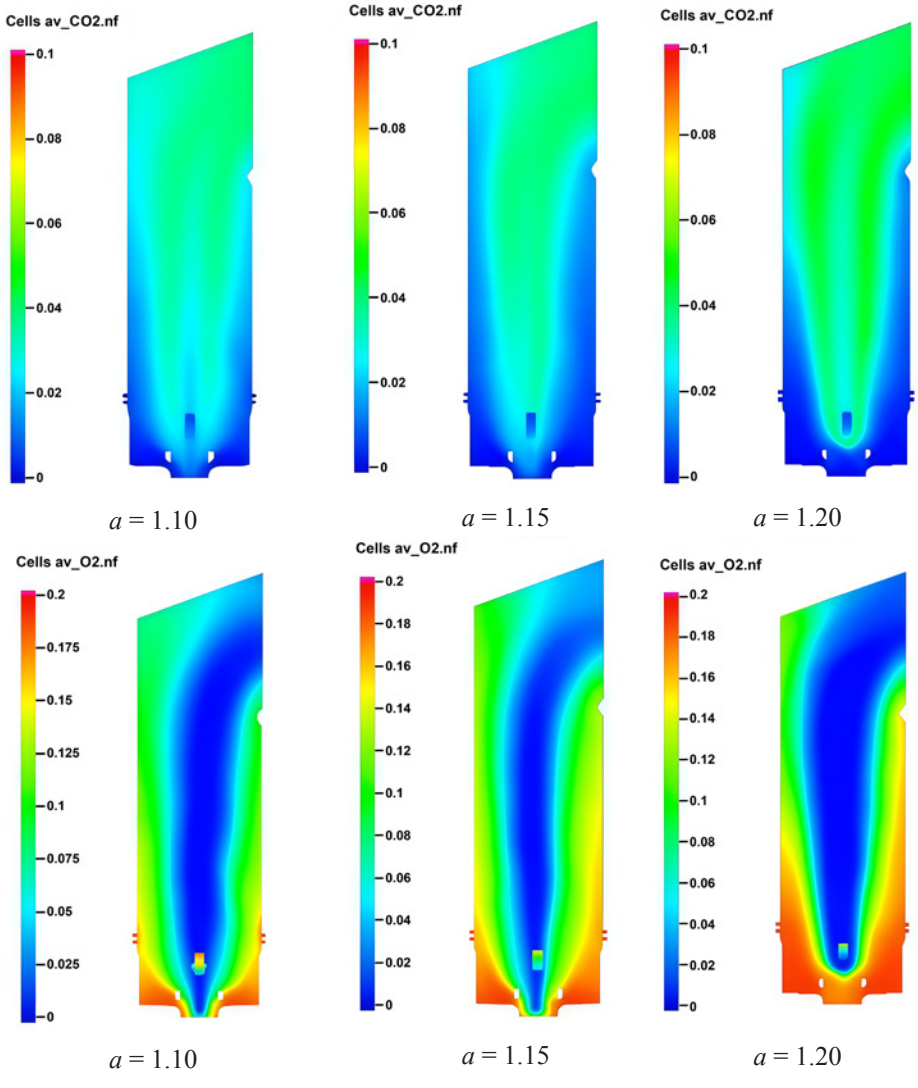

$a = 1.10$ $a = 1.15$ $a = 1.20$

$a = 1.10$ $a = 1.15$ $a = 1.20$

Fig. 10. Distribution of O_2 and CO_2 concentrations under different excess air ratios.

Table 5 shows the mass fraction of the gas composition at the outlet. The test values were obtained using a flue gas analyzer at the center of the boiler outlet pipe under stable operating conditions at the boiler's rated load (65 t/h) and an excess air coefficient of 1.15. During the measurement period, the feed rate was maintained at 39265 kg/h. It is observed that the concentrations of O_2 and CO_2 at the outlet are lower than the experimental values. Figure 3 indicates that there is an intermediate product, CO, in the flue gas at the outlet, demonstrating that the oil shale in the furnace is not fully burned, so the CO_2 concentration is 27% lower than the measured value.

The decrease in the O_2 concentration at the outlet is affected by the secondary airflow. Figure 10 confirms that the oxygen content in the center of the furnace is relatively low. This is due to the insufficient diffusion of the secondary airflow, which makes the oxygen inside the furnace anoxic. This phenomenon not only leads to insufficient combustion in the furnace and decreases the CO_2 concentration, but also reduces the O_2 concentration at the outlet and leads to a deviation between the calculated concentrations and the measured values. It is worth noting that the deviation between the two gases is less than 25%. It is concluded that the calculated results are in good agreement with the experiment, and the developed model can be used to simulate the combustion in CFB boilers.

Table 5. Mass fraction of main gas components at the outlet, %

Gas	Numerical calculation result	Test value	Deviation
O_2	2.9	3.7	21
CO_2	7.8	10.8	27

4.2. Simulation of pollutant gases

4.2.1. Effects of different excess air ratios on the emission of pollutant gases

Figure 11 shows the molar fraction of the pollutant gases (CO_2, CO, NO, and SO_2) at the outlet of the high-low differential velocity CFB with an excess air ratio of 1.15. It is observed that the deviation between the calculated values and the experimental results is within a reasonable range, which reflects the accuracy of the model.

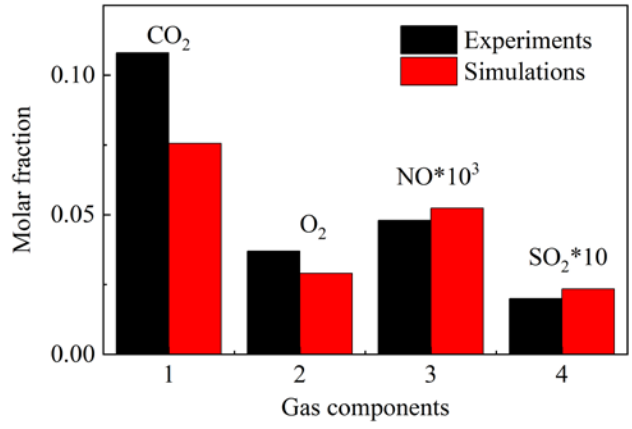

Fig. 11. Molar fraction of gases at the outlet (a = 1.15).

Figures 12 and 13 show the time-averaged distribution of NO and N_2O concentrations along the furnace height, respectively. In the bottom region, the formation of NO gas mainly originates from coke combustion. Near the feed opening, coke combustion and volatile fraction release rapidly increase the concentration of NO until a peak is reached above the feed opening, where the generation and reduction reactions reach equilibrium. NO then reacts with CO or coke, and N_2 is produced. Therefore, the NO concentration decreases along the height of the furnace. More specifically, NO concentration decreases to 52 ppm at the outlet.

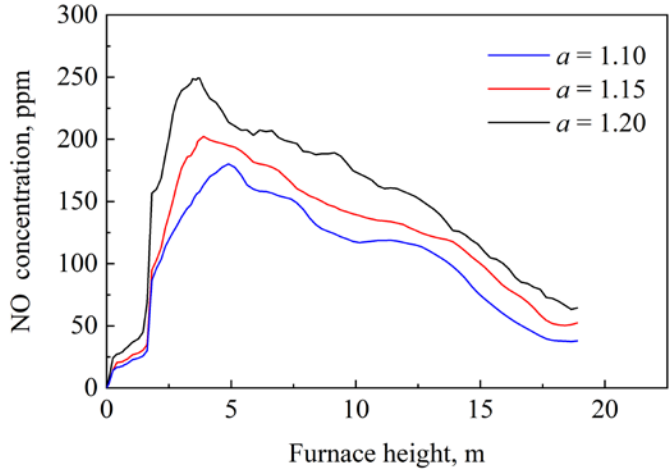

Fig. 12. Time-average distribution of NO gas concentration along the height of the furnace chamber.

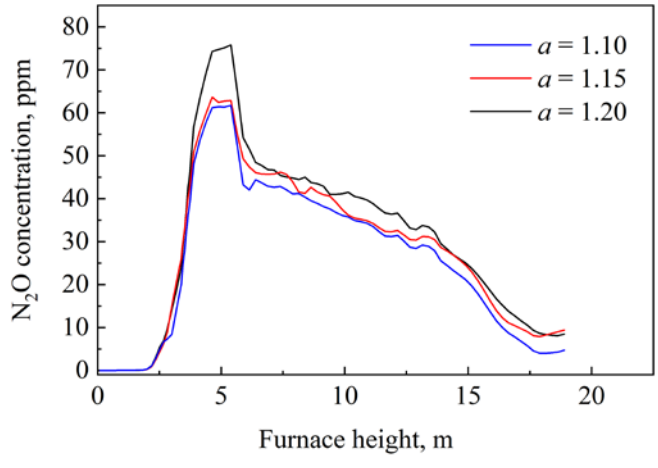

Fig. 13. Time-averaged distribution of N_2O gas concentration along the height of the furnace chamber.

N_2O is mainly derived from the reaction between NO and CNO, and its concentration increases with increasing NO concentration. At a certain position above the feed opening, N_2O production is balanced by the reduction reaction. At this point, the N_2O concentration reaches its maximum and then decreases along the furnace height.

As the excess air ratio increases, NO concentration also increases gradually, which is mainly due to the reaction between HCN and NH_3. Consequently, the simultaneous decrease in char and CO weakens the reduction of NO, leading to higher NO concentrations [29].

Figure 14 illustrates the time-averaged distribution contour of the combustion gas. In the vicinity of the feed port, the NO concentration reaches its

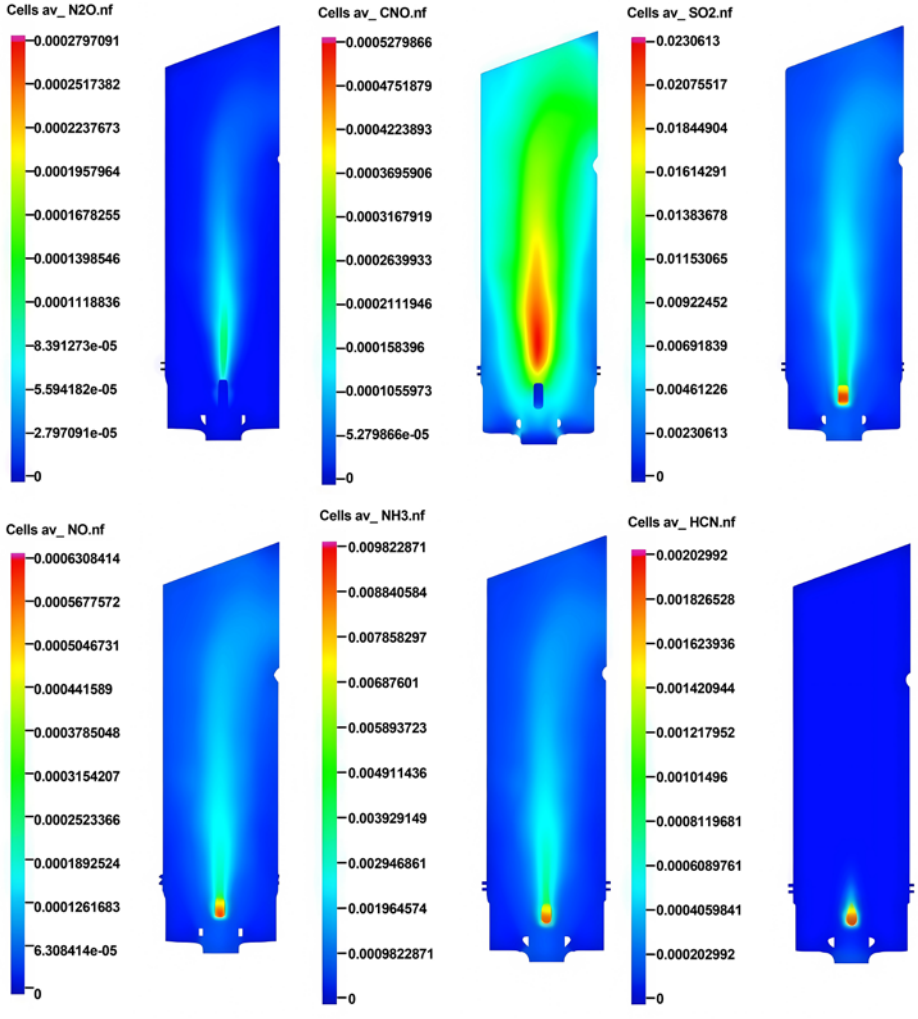

Fig. 14. Contours of the time-averaged distribution of gas components (a = 1.15).

maximum, indicating the oxidation of nitrogen. During the pyrolysis process, NH_3 is released into the furnace, and HCN is quickly converted to CNO, most of which is produced near the feed port. Moreover, N_2O is mainly produced from the reaction between CNO and NO. Consequently, the N_2O concentration is relatively high above the feed port.

As shown in Figures 12 and 14, the NO concentration peaks near the feed inlet, primarily originating from two competing pathways: rapid oxidation of fuel nitrogen (mainly present as HCN and NH_3 in volatile matter) in the high-temperature zone, and oxidation of carbon nitrogen. However, the unique flow structure of the high-low differential velocity CFB plays a crucial role. Intense particle recirculation creates localized zones rich in coke and CO within the furnace, establishing ideal conditions for both heterogeneous reduction (e.g., $NO + C \rightarrow 0.5N_2 + CO$) and homogeneous reduction (e.g., $NO + CO \rightarrow 0.5N_2 + CO_2$) of NO. Consequently, along the furnace height, the NO concentration exhibits a decreasing trend after reaching its peak.

4.2.2. Effect of different air distribution volumes in the main bed and side beds on the emission characteristics of pollutant gases

The CFB staged combustion technology can achieve low emissions of nitrogen and sulfur oxides to a certain extent. In a 65-t/h high-low differential velocity CFB, the fuel is supplied to the main bed from both sides of the furnace, and the airflow enters the main bed and side beds, respectively. This segmented air supply reduces NOx and other gas emissions. Figure 15 shows the NO and SO_2 emissions at the furnace outlet under different air volume ratios of the main bed and side beds with an excess air ratio of 1.10. It is observed that the lowest pollution can be achieved when the air volume ratio of the main bed and side beds is 1.5:1. This is the optimal operating condition to minimize pollution emissions in actual operation.

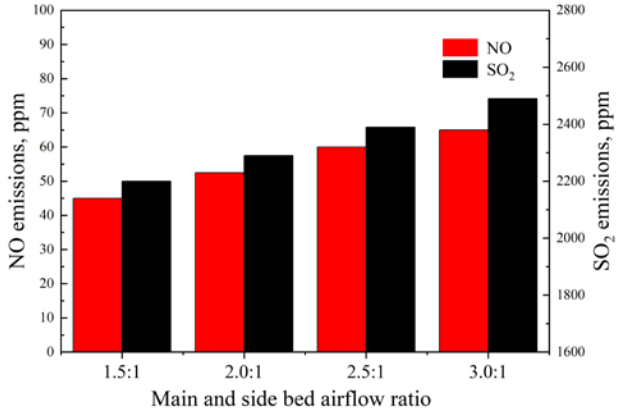

Fig. 15. Emissions of NO and SO_2 at different air distribution volumes in the main bed and side beds.

5. Conclusions

This study reveals that enhanced particle recirculation behavior, achieved by optimizing operational parameters such as a low excess air coefficient and a specific main/side bed airflow ratio in high-low differential velocity circulating fluidized beds, is crucial for achieving efficient fuel combustion and deep NOx suppression. The CPFD-predicted particle back-mixing correlates strongly with NO_X suppression efficiency. In the present study, the combustion characteristics in a 65-t/h high-low differential velocity CFB boiler were numerically simulated. Different excess air ratios and air volume ratios were considered to obtain the best working conditions. Based on the obtained results and analyses, the main conclusions can be summarized as follows:

1. This study demonstrates that the unique structural design of the high-low differential velocity circulating fluidized bed induces intense particle remixing. This hydrodynamic characteristic serves as the key intrinsic mechanism for achieving synergistic enhancement of efficient combustion and low pollutant emissions. Simulation results indicate that a moderate excess air coefficient (a = 1.10) maximizes this remixing effect.
2. Pyrolytic HCN and NH_3 peak near the feed ports and then decrease along the furnace height. Similarly, N_2O and NO concentrations also show peak values near the feeding zone under all tested excess air ratios.
3. Condition comparisons reveal that an excess air ratio of 1.10 promotes intense particle back-mixing and efficient combustion. Furthermore, at this optimal excess air ratio, the air volume ratio between the main bed and side beds significantly influences NO_x and SO_2 emissions, with a ratio of 1.5:1 yielding the lowest emissions.

Data availability statement

All data generated or analyzed during this study are contained within the article.

Acknowledgments

The authors appreciate the support of the Jilin Provincial Science and Technology Development Program (20200403162SF) and Jiangxi Jianglian Heavy Industry Group Co., Ltd. The publication costs of this article were partially covered by the Estonian Academy of Sciences.

References

1. Qing, W., Liu, H., Bai, J., Qin, H., Yang, W. Application of high-low bed CFB combustion technology to oil shale combustion. *Oil Shale*, 2013, **30**(2), 147–156. https://doi.org/10.3176/oil.2013.2.05
2. Wang, Q., Xiao, J. B., Liu, H. P. 2D CFD simulation of hydrodynamics of the dense zone of a 65 t/h high-low bed CFB. *Advanced Materials Research*, 2012, **614–615**, 596–599. https://doi.org/10.4028/www.scientific.net/AMR.614-615.596
3. Zhao, P. (P.), O'Rourke, P. J., Snider, D. Three-dimensional simulation of liquid injection, film formation and transport, in fluidized beds. *Particuology*, 2009, **7**(5), 337–346. https://doi.org/10.1016/j.partic.2009.07.002
4. O'Rourke, P. J., Zhao, P. (P.), Snider, D. A model for collisional exchange in gas/liquid/solid fluidized beds. *Chemical Engineering Science*, 2009, **64**(8), 1784–1797. https://doi.org/10.1016/j.ces.2008.12.014
5. Snider, D. M., Clark, S. M., O'Rourke, P. J. Eulerian–Lagrangian method for three-dimensional thermal reacting flow with application to coal gasifiers. *Chemical Engineering Science*, 2011, **66**(6), 1285–1295. https://doi.org/10.1016/j.ces.2010.12.042
6. O'Rourke, P. J., Snider, D. M. An improved collision damping time for MP-PIC calculations of dense particle flows with applications to polydisperse sedimenting beds and colliding particle jets. *Chemical Engineering Science*, 2010, **65**(22), 6014–6028. https://doi.org/10.1016/j.ces.2010.08.032
7. Abbasi, A., Ege, P. E., de Lasa, H. I. CPFD simulation of a fast fluidized bed steam coal gasifier feeding section. *Chemical Engineering Journal*, 2011, **174**(1), 341–350. https://doi.org/10.1016/j.cej.2011.07.085
8. Loha, C., Chattopadhyay, H., Chatterjee, P. K. Three dimensional kinetic modeling of fluidized bed biomass gasification. *Chemical Engineering Science*, 2014, **109**, 53–64. https://doi.org/10.1016/j.ces.2014.01.017
9. Ma, Q., Lei, F., Xiao, Y. Numerical analysis of operating conditions for establishing high-density circulating fluidized bed by CPFD method. *Powder Technology*, 2018, **338**, 446–457. https://doi.org/10.1016/j.powtec.2018.07.012
10. Tu, Q., Wang, H. CPFD study of a full-loop three-dimensional pilot-scale circulating fluidized bed based on EMMS drag model. *Powder Technology*, 2018, **323**, 534–547. https://doi.org/10.1016/j.powtec.2017.09.045
11. Chen, C., Werther, J., Heinrich, S., Qi, H.-Y., Hartge, E.-U. CPFD simulation of circulating fluidized bed risers. *Powder Technology*, 2013, **235**, 238–247. https://doi.org/10.1016/j.powtec.2012.10.014
12. Liu, H., Li, J., Wang, Q. Three-dimensional numerical simulation of the co-combustion of oil shale retorting solid waste with cornstalk particles in a circulating fluidized bed reactor. *Applied Thermal Engineering*, 2018, **130**, 296–308. https://doi.org/10.1016/j.applthermaleng.2017.10.107
13. Liu, H., Li, J., Wang, Q. Simulation of gas–solid flow characteristics in a circulating fluidized bed based on a computational particle fluid dynamics

model. *Powder Technology*, 2017, **321**, 132–142. https://doi.org/10.1016/j.powtec.2017.07.040

14. Wang, Q., Yang, H., Wang, P., Lu, J., Liu, Q., Zhang, H. et al. Application of CPFD method in the simulation of a circulating fluidized bed with a loop seal, part I—determination of modeling parameters. *Powder Technology*, 2014, **253**, 814–821. https://doi.org/10.1016/j.powtec.2013.11.041
15. Shi, X., Lan, X., Liu, F., Zhang, Y., Gao, J. Effect of particle size distribution on hydrodynamics and solids back-mixing in CFB risers using CPFD simulation. *Powder Technology*, 2014, **266**, 135–143. https://doi.org/10.1016/j.powtec.2014.06.025
16. Lan, X., Shi, X., Zhang, Y., Wang, Y., Xu, C., Gao, J. Solids back-mixing behavior and effect of the mesoscale structure in CFB risers. *Industrial & Engineering Chemistry Research*, 2013, **52**(34), 11888–11896. https://doi.org/10.1021/ie3034448
17. Yan, J., Lu, X., Xue, R., Lu, J., Zheng, Y., Zhang, Y. et al. Validation and application of CPFD model in simulating gas-solid flow and combustion of a supercritical CFB boiler with improved inlet boundary conditions. *Fuel Processing Technology*, 2020, **208**, 106512. https://doi.org/10.1016/j.fuproc.2020.106512
18. Shen, X., Jia, L., Wang, Y., Guo, B., Fan, H., Qiao, X. et al. Study on dynamic characteristics of residual char of CFB boiler based on CPFD method. *Energies*, 2020, **13**(22), 5883. https://doi.org/10.3390/en13225883
19. Auzerais, F. M., Jackson, R., Russel, W. B. The resolution of shocks and the effects of compressible sediments in transient settling. *Journal of Fluid Mechanics*, 1988, **195**, 437–462. https://doi.org/10.1017/S0022112088002472
20. Snider, D. M. An incompressible three-dimensional multiphase particle-in-cell model for dense particle flows. *Journal of Computational Physics*, 2001, **170**(2), 523–549. https://doi.org/10.1006/jcph.2001.6747
21. Jalali, P., Hyppänen, T. Momentum transport between two granular phases of spherical particles with large size ratio: two-fluid model versus discrete element method. *Powder Technology*, 2015, **273**, 13–18. https://doi.org/10.1016/j.powtec.2014.12.026
22. Lanza, A., Islam, M. A., de Lasa H. CPFD modeling and experimental validation of gas–solid flow in a down flow reactor. *Computers & Chemical Engineering*, 2016, **90**, 79–93. https://doi.org/10.1016/j.compchemeng.2016.04.007
23. Snider, D. M., Clark, S. M., O'Rourke, P. J. Eulerian–Lagrangian method for three-dimensional thermal reacting flow with application to coal gasifiers. *Chemical Engineering Science*, 2011, **66**(6), 1285–1295. https://doi.org/10.1016/j.ces.2010.12.042
24. de Souza-Santos, M. L. Comprehensive modelling and simulation of fluidized bed boilers and gasifiers. *Fuel*, 1989, **68**(12), 1507–1521. https://doi.org/10.1016/0016-2361(89)90288-3
25. Goel, S. K., Morihara, A., Tullin, C. J., Sarofim, A. F. Effect of NO and O_2 concentration on N_2O formation during coal combustion in a fluidized-bed combustor: modeling results. *Symposium (International) on Combustion*, 1994, **25**(1), 1051–1059. https://doi.org/10.1016/S0082-0784(06)80743-5

26. Liu, H., Feng, B., Lu, J., Zheng, C. Coal property effects on N_2O and NO_x formation from circulating fluidized bed combustion of coal. *Chemical Engineering Communications*, 2005, **192**(11), 1482–1489. https://doi.org/10.1080/009864490896043
27. Kilpinen, P., Kallio, S., Konttinen, J., Barišić, V. Char-nitrogen oxidation under fluidised bed combustion conditions: single particle studies. *Fuel*, 2002, **81**(18), 2349–2362. https://doi.org/10.1016/S0016-2361(02)00176-X
28. Shi, X., Wu, Y., Lan, X., Liu, F., Gao, J. Effects of the riser exit geometries on the hydrodynamics and solids back-mixing in CFB risers: 3D simulation using CPFD approach. *Powder Technology*, 2015, **284**, 130–142. https://doi.org/10.1016/j.powtec.2015.06.049
29. Zhong, W., Xie, J., Shao, Y., Liu, X., Jin, B. Three-dimensional modeling of olive cake combustion in CFB. *Applied Thermal Engineering*, 2015, **88**, 322–333. https://doi.org/10.1016/j.applthermaleng.2014.10.086

Oil Shale, 2026, 43, 2, 143–164 https://doi.org/10.3176/oil.2026.2.02

Heat transfer optimization in oil shale rotary retorting via DEM and BP neural network

Sitong Liu[(a)], Naying Yuan[(a)], Chunhua Wang[(a)]*, Yubaodan Sun[(b)], Ninging Li[(a)]*, Yue Yue[(a)], Haodan Pan[(a)], Zhiyong Hu[(a)], Lei Zhao[(a)]

[(a)] College of Mechanical Engineering, Liaoning Petrochemical University, Fushun, 113001, China

[(b)] Hubei Institute of Aerospace Chemotechnology, Xiangyang, 441003, China

Received 3 August 2025, accepted 8 April 2026, available online 16 April 2026

Abstract. *To enhance heat transfer between shale ash and oil shale particles in a rotary retorting furnace, this study coupled the discrete element method (DEM) with a particle heat conduction model to simulate mixing and heat transfer, examining the effects of particle filling ratio, furnace rotational speed, and baffle structures. A backpropagation neural network (BP-NN) model was built from simulation data to map furnace operation time with key parameters, and a genetic algorithm was used to optimize parameters to minimize operation time. The research results show that lower filling degrees and higher rotation speeds significantly strengthen particle mixing and heat exchange, which accelerate the system's stabilization, improve temperature field uniformity, and reduce the temperature standard deviation. The mixing and heat transfer effect of the straight baffle is between that of the right-angle baffle and the inclined baffle, but it causes the largest temperature standard deviation. In contrast, the right-angle baffle demonstrates stronger advantages in heat transfer uniformity during particle lifting and throwing. The constructed BP-NN prediction model achieves a relative error accuracy within 0.25%, effectively solving the long computation time problem of DEM simulation. The optimized parameter combination provides a theoretical basis for the development of high-efficiency and energy-saving rotary retorting furnaces.*

Keywords**:** *oil shale, rotary retorting furnace, DEM, BP-NN.*

1. Introduction

Oil shale is a type of sedimentary rock containing a substance known as kerogen, which can be converted to liquid hydrocarbons through thermal treatment [1, 2]. Despite its low energy density and high production cost, oil shale, as

* Corresponding authors, wangchunhua@lnpu.edu.cn, lining773239@163.com

a non-conventional oil source, is rich in reserves and widely distributed [3, 4]. This is of strategic importance, as it can effectively supplement traditional fossil energy, reduce dependence on imported oil, enhance energy security, and promote the diversification of the energy structure. At present, Estonia, Brazil, the United States, and other countries have advanced oil shale processing technologies and have realized its industrial utilization. China has also carried out oil shale processing in Fushun, Xinjiang, and Gansu, among which Fushun has the largest annual production of shale oil [5].

The operational performance of an oil shale rotary retorting furnace (abbreviated as a rotary furnace here), as an efficient thermal conversion equipment, directly depends on the synergistic optimization of particle mixing and heat transfer efficiency [6–8]. Studies have shown that conventional operating parameters such as rotational speed, particle filling degree, and baffle shape have a significant effect on the particle flow pattern and heat transfer characteristics in the furnace [9–11]. Zhang et al. [12] experimentally investigated the mixing behavior of unequal particle size oil shale and solid heat carrier particles in a rotary furnace. They found that, when convective mixing was predominant, the mixing degree was better under the condition of using a right-angle baffle with a 20% filling degree and an inclination angle of 3.24° than under other corresponding conditions. Herz et al. [13] experimentally investigated the influence of rotational speed and filling degree on the contact heat transfer coefficient in rotary furnaces, revealing that the heat transfer coefficient increased with higher rotational speeds and lower filling degrees.

The optimization of reactor structure is equally crucial for enhancing processing efficiency and enabling the treatment of diverse feedstocks. Liang et al. [14] demonstrated the feasibility of an indirect-heating rotary kiln for pyrolyzing small-particle oil shale in an engineering experiment, highlighting its advantages such as low dust carry-over and stable operation, which provides a valuable reference for the industrial application of rotary kiln technology. Furthermore, in the context of global carbon reduction efforts, the exploration of alternative energy sources and reducing agents has become a key research direction. In a related metallurgical field, Nabilah et al. [15] investigated the reduction of saprolite nickel ore using a methane-argon gas mixture in a laboratory-scale simulated rotary kiln, exploring the feasibility of this low-carbon fuel as an alternative to traditional carbon-based reductants, thereby underscoring the potential for efficient and clean operation through parameter and energy structure optimization.

To delve into the parameter optimization mechanism, researchers have widely used numerical simulation methods such as the discrete element method (DEM) [16]. The application of DEM has proven highly effective in simulating particle systems within rotary equipment. Hu et al. [17] proposed a robust DEM framework for efficiently simulating heat generation in long-duration recurrent granular flows, providing a powerful numerical tool for

complex thermo-mechanical processes. Similarly, Wu et al. [18] combined experimental methods with computational fluid dynamics and the discrete element method (CFD-DEM) to study the drying characteristics of soil in large-scale rotary kilns, validating the applicability of DEM in coupled multiphysics field analyses. Building on this foundation, studies specific to oil shale retorting have yielded significant insights. Arntz et al. [19] used DEM to simulate the mixing and segregation inside the rotary furnace, systematically analyzing the effects of filling rate, rotational speed, and other factors on the mixing process. Wang et al. [20] combined DEM with a particle heat transfer model to study the mixing and heat transfer process of shale ash particles and oil shale particles. They used the mixing index, particle average temperature, and temperature standard deviation as evaluation indexes to analyze the influence of the filling rate, the furnace rotational speed, and the form of the baffle on the mixing and heat transfer characteristics of particles. Wang et al. [21] proposed a comprehensive heat transfer model including conduction and radiation, and used DEM to deeply analyze the effects of rotational speed and filling rate on the heating time. Xie et al. [22] employed DEM simulations to investigate rotary furnaces, revealing that the specific heat transfer coefficient of particle flows increased with rotational speed.

While DEM studies effectively reveal underlying mechanisms, they rely on complex, computationally intensive physical modeling. This makes real-time optimization of numerous coupled variables challenging. Additionally, experimental studies are limited by equipment scale and operating conditions, making it difficult to fully cover the complex working conditions under the interaction of multiple parameters.

In recent years, the rapid development of artificial intelligence (AI) technology has provided new ideas to break through the above bottlenecks. Neural-network-based prediction models can quickly establish a nonlinear mapping relationship between operating parameters and mixing and heat transfer performance by learning from a large amount of numerical simulation or experimental data. Currently, neural network algorithms are increasingly widely used in the research of rotary furnaces. By learning a large amount of simulation data and experimental data, neural networks can establish a complex relationship model between operating parameters, structural parameters, and particle mixing and heat transfer effects, and then realize the effective prediction of the performance of the rotary furnace [23, 24]. Neural networks, when integrated with intelligent algorithms such as genetic algorithms or particle swarm optimization (PSO), can achieve multi-objective parameter co-optimization [25, 26]. By establishing optimization objectives that represent mixing efficiency and heat transfer performance, these intelligent optimization algorithms can identify optimal solutions from numerous parameter combinations, thereby enabling the efficient operation of rotary furnaces.

2. Heat transfer analysis and modeling

The heat transfer between particles within the rotary furnace primarily occurs through direct contact conduction and intra-particle conduction, while the influence of interstitial fluid and radiation is considered negligible in the oxygen-free retorting environment, consistent with our previous study [27]. Therefore, a simplified particle heat conduction model, focusing on contact heat transfer, was employed in the DEM simulations.

To balance computational accuracy and efficiency, the following key assumptions were adopted: (1) particles are spherical with constant thermophysical properties; (2) the furnace wall is adiabatic; (3) the heat loss through the wall and the effect of pyrolysis volatiles on interparticle heat transfer are neglected; (4) periodic boundary conditions were applied at both ends of the reactor to simulate the axial behavior of an infinitely long rotary kiln and avoid end effects.

Based on the particle diameters (4 mm for oil shale particles and 3 mm for shale ash particles), material thermal conductivities (0.6 $W \cdot m^{-1} \cdot K^{-1}$ for oil shale and 0.9 $W \cdot m^{-1} \cdot K^{-1}$ for shale ash), and the typical effective inter-particle contact heat transfer coefficient reported in the literature (50–400 $W \cdot m^{-2} \cdot K^{-1}$) [28], the estimated Biot number ranges from approximately 0.03 to 0.44. This result indicates that the internal conductive resistance of the particles is relatively small compared to the external contact resistance between particles.

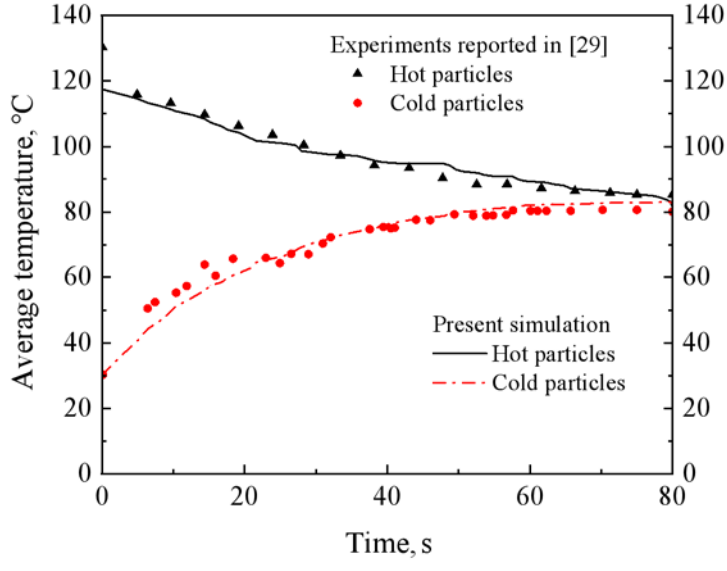

Fig. 1. Comparison between numerical simulation and experimental results for model validation.

Therefore, although the strict criterion for the lumped capacitance method (Bi << 1) is not fully satisfied at the upper end of this range, the simplified "one-temperature-per-particle" assumption employed in the present DEM model represents a reasonable and acceptable approximation for capturing system-level macroscopic heat transfer dynamics. This conclusion is further supported by experimental data from the literature [29], as shown in Figure 1. The simulated temperature evolution of the binary particle system (quartz sand and glass beads) showed good agreement with the experimental data, with the maximum relative error controlled within 9%. This confirms the model's capability to accurately capture the dynamics of particle contact heat transfer. Detailed information regarding the validation setup and material properties can be found in [27].

3. Research objects and simulation matrix

A scaled-down rotary furnace model was constructed for the DEM simulations, with key structural dimensions illustrated in Figure 2 (inner radius R_1 = 30 mm, outer radius R_2 = 32 mm, axial length L = 30 mm). The material properties for oil shale particles, shale ash particles, and the retorting wall, along with the inter-particle and particle-wall contact parameters (restitution, static, and rolling friction coefficients), were set according to the values established in our previous work (see tables 3 and 4 in [27] for details).

It should be noted that this study primarily aims to reveal fundamental mechanisms. Future work will focus on dimensional analysis and scaling laws (such as the Froude number and filling degree similarity) to facilitate the translation of these findings to industrial-scale applications.

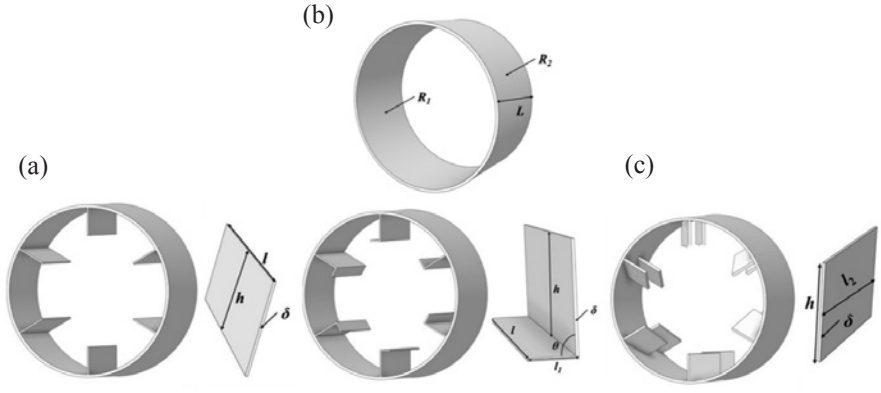

R_1 = 30 mm, R_2 = 32 mm, L = 30 mm, l = 30 mm, h = 10 mm, δ = 0.5 mm, l_1 = 4 mm, l_2 = 4 mm

Fig. 2. Structure of the baffle in the rotary furnace: straight baffle (a), right-angle baffle (b), and inclined baffle (c).

Simulations varied three key parameters – particle filling degree (20%, 30%, 50%), rotational speed (3, 4, 5 rpm), and baffle shape (straight, right-angle, inclined) – to generate the dataset for subsequent neural network training and optimization. This parametric analysis aims to systematically elucidate the influence mechanisms of these parameters on particle mixing and heat transfer characteristics. All simulated conditions maintained an initial mass ratio of 3:1 between oil shale and shale ash, with the initial temperature of shale ash (740 °C) set significantly higher than that of oil shale (110 °C) to accurately simulate the solid heat carrier process used in industrial applications.

4. Analysis of DEM simulation results

4.1. Evaluation metrics for particle mixing and heat transfer

To analyze the mixing and heat transfer between oil shale and shale ash particles, the mixing index (M), the average temperature of oil shale particles ($\overline{T}$), and the particle temperature standard deviation (S_T) were employed as evaluation metrics [26]. A higher M value indicates better mixing, while a lower S_T signifies a more uniform temperature distribution and superior heat transfer performance.

4.2. Influence of operational and structural parameters

As shown in Figure 3, a lower filling degree (20%) significantly enhanced particle mixing, achieving a higher maximum mixing index (0.217) more rapidly (112 s) compared to higher ratios (30% and 50%). This is attributed to increased particle mobility and enhanced convective mixing under reduced gravitational compaction. This observation aligns with the findings of Herz et al. [13] and Nafsun et al. [30], who also reported improved heat transfer performance at lower filling levels in rotary kilns. Although the final average temperature was similar across all cases (approximately 520 °C), the temperature distribution was markedly more uniform at the lower filling degree, as evidenced by a smaller temperature standard deviation. This indicates that reducing the filling degree improves heat transfer efficiency primarily by enhancing temperature uniformity rather than by altering the overall heating rate.

Increasing the rotational speed from 3 to 5 rpm, as illustrated in Figure 4, accelerated both the mixing rate and the heating rate of the oil shale particles. The system reached a stable mixing state more quickly at higher speeds. More importantly, the temperature standard deviation decreased significantly with increasing rotational speed, demonstrating that a higher speed effectively promotes a more homogeneous temperature field. This result is consistent with the conclusions of Xie et al. [22], who demonstrated that the specific heat transfer coefficient increases with rotational speed. At 5 rpm, the competing

effects of enhanced collision-induced mixing and incipient radial segregation led to fluctuations in the mixing index after 150 s; nevertheless, the overall heat transfer performance was superior.

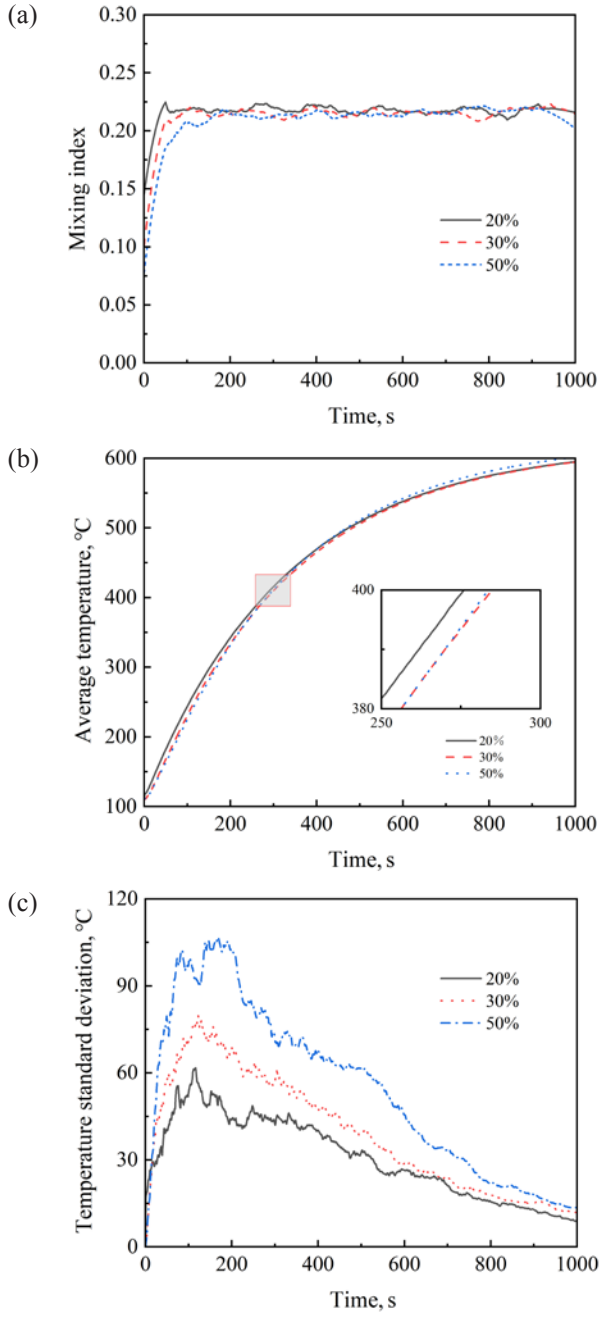

Fig. 3. Variation of evaluation indices under different filling degrees: mixing index (a), average temperature (b), and temperature standard deviation (c).

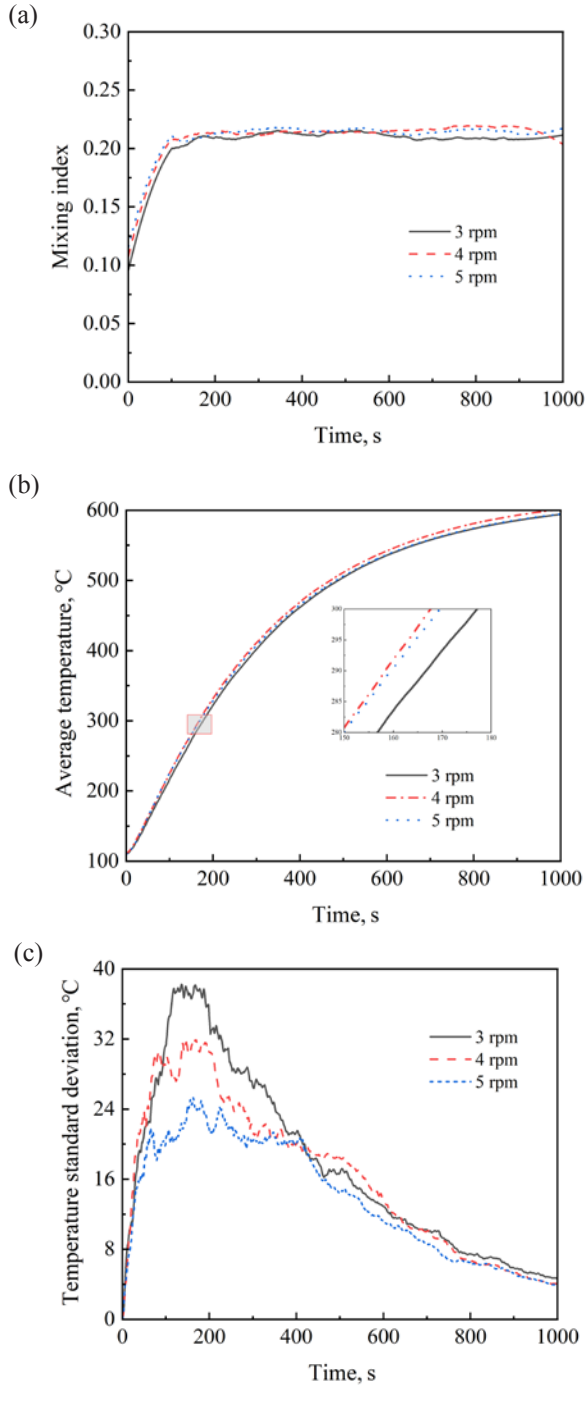

Fig. 4. Variation of evaluation indices under different rotational speeds: mixing index (a), average temperature (b), and temperature standard deviation (c).

As shown in Figure 5, the installation of baffles markedly improved mixing compared to the baffle-free structure. Among the three baffle types studied, the right-angle baffle yielded the best mixing performance ($M \approx 0.22$) and, crucially, the most uniform temperature distribution (lowest S_T). Although the straight baffle achieved a mixing index similar to that of the inclined baffle (approximately 0.21), it resulted in the largest temperature deviation. The superior performance of the right-angle baffle in achieving homogeneous mixing corroborates the experimental findings of Zhang et al. [12], who identified the right-angle baffle as optimal under specific conditions. The superior performance of the right-angle baffle stems from its ability to generate secondary vortices during particle lifting and cascading, thereby promoting radial mixing and increasing the contact frequency between hot and cold particles.

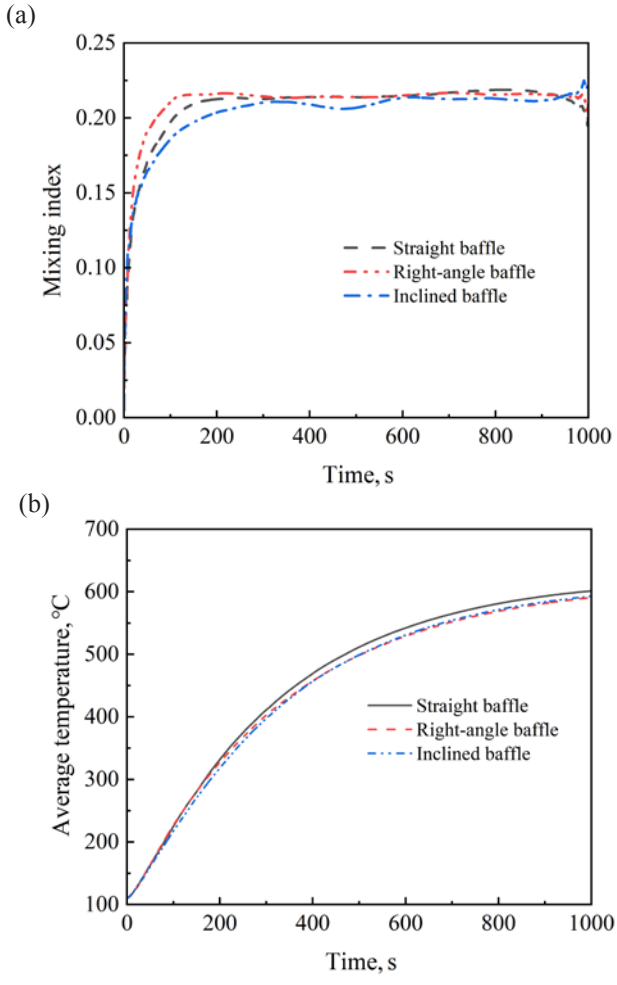

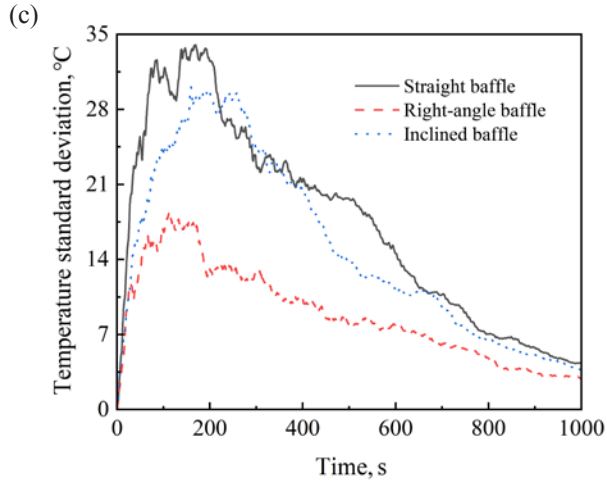

Fig. 5. Variation of evaluation indices under different baffle structures: mixing index (a), average temperature (b), and temperature standard deviation (c).

These trends are concisely summarized in Table 1, which provides a systematic comparison of how each parameter influences mixing and heat transfer performance. The synthesized results demonstrate that operational parameters (filling degree and rotational speed) predominantly affect the rate of mixing and heat transfer, as well as the uniformity of the temperature field, while structural parameters (baffle shape) play a decisive role in mixing effectiveness and thermal homogeneity. Among all configurations, the right-angle baffle combined with a lower filling degree and moderate rotational speed delivered the most favorable performance under the investigated conditions.

The results demonstrate that operational parameters (filling degree, rotational speed) primarily influence the rate of mixing and heat transfer, as well as the uniformity of the temperature field. Under the investigated conditions, the right-angle baffle was identified as the optimal design.

Table 1. Summary of the effects of key parameters on mixing and heat transfer

Parameter	Variation trend	Effect on mixing	Effect on heat transfer uniformity (S_T)
Filling degree	Decrease (50% → 20%)	Significant improvement	Significant improvement (reduces S_T)
Rotational speed	Increase (3 → 5 rpm)	Improvement (may fluctuate at high speed)	Significant improvement (reduces S_T)
Baffle type	Right-angle > inclined > straight	Right-angle is optimal	Right-angle is optimal (lowest S_T)

5. Intelligent optimization

The above analysis shows that the particle filling degree, furnace rotational speed, and baffle structure are critical parameters affecting oil shale retorting. Through genetic algorithm optimization of operating parameters, this study identifies the optimal parameter combination to achieve the best heat transfer and mixing effects for a specific baffle structure, thereby enhancing the stability and controllability of the reaction process. Optimizing operating parameters to reach the target temperature in the shortest time can significantly reduce the production cycle, improve equipment operational efficiency, and lower energy consumption and production costs.

To this end, based on DEM simulation results, this study employs backpropagation neural networks (BP-NN) and genetic algorithms to comprehensively optimize the above operating parameters and baffle structural parameters. The research is divided into two parts:

(1) BP-NN modeling: Mathematical models were established using the BP-NN neural network method to characterize the operational time of the furnace with different baffle structures in relation to filling degree, rotational speed, mixing index, and particle average temperature.

(2) Genetic algorithm optimization: With the objective of minimizing the operational time required for the furnace to reach the set target temperature (i.e., particle average temperature), operating parameters for different baffle structures – including filling degree, rotational speed, and mixing index – were optimized to facilitate better control of the reaction process.

5.1. Establishment of a training library

Using DEM simulation results under different cases, this study selected filling degree, rotational speed, mixing index, average temperature of oil shale particles, and furnace operation time data for different baffle structures. Learning samples were constructed for straight, right-angle, and inclined baffles, with sample sizes of 24901, 33173, and 41300 data points, respectively. For each baffle type, learning samples were randomly divided into test and training sets in a 1:9 ratio. Predicted operation times for test samples were obtained via neural network training and compared with their corresponding actual values.

5.2. Neural network prediction model

5.2.1. Model building

BP-NN is a multi-layer feed-forward neural network trained by the error back-propagation algorithm. It is widely used in large-scale model prediction due to its high modeling accuracy and short training time. The network consists of

an input layer, hidden layers, and an output layer, with the input signal passing through the hidden layers to the output layer.

This study employs a three-layer BP-NN, with the input layer consisting of four key parameters: filling degree, rotational speed, mixing index, and average temperature of oil shale particles. The output layer predicts the corresponding operation time. The network includes two hidden layers, each with 20 neurons. The training function is *trainbr* based on the Bayesian regularization algorithm, which reduces the overfitting risk and improves model generalization. The mean square error is used as the performance evaluation function, with a network convergence error set to 1e-6. The *tansig* activation function handles nonlinear features, while the output layer uses the *purelin* linear function to directly predict the shortest operation time.

5.2.2. Predicted results

Figure 6 shows the comparison results between predicted and actual operation times of test samples for the inclined baffle structure, along with the relative error distribution of predictions obtained via neural network training. The predicted operation times exhibit a high degree of consistency and overlap with actual values, indicating excellent prediction performance and confirming that the neural network algorithm meets the model prediction requirements of this study. Due to the large dataset, only partial comparison results are presented in Figure 6.

As shown in Figure 7, the relative error distribution of operation time predictions for the inclined baffle indicates that the relative errors of more than 90% of training samples are controlled within ±0.1%, with the maximum relative error not exceeding 0.25%. Calculations show that the average

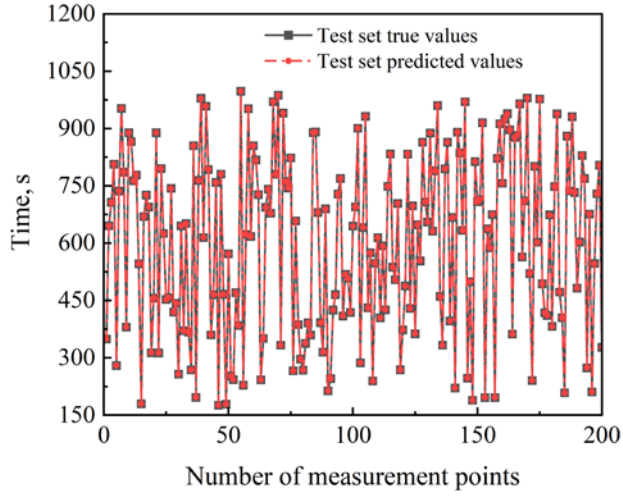

Fig. 6. Comparison between predicted and actual operation times and relative error distribution for the inclined baffle structure.

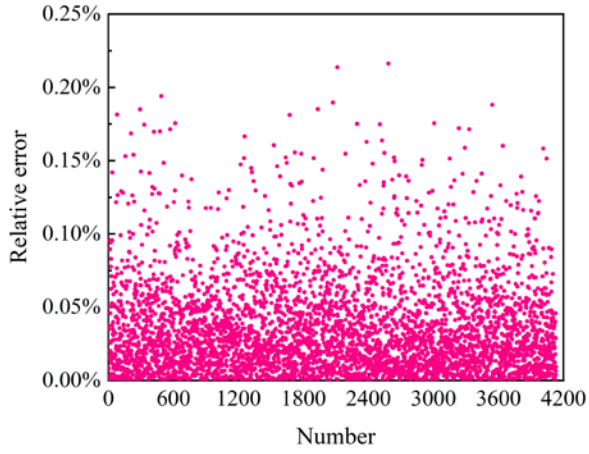

Fig. 7. Relative error of predicted operation time for inclined baffle test set.

relative errors of operation time predictions for the straight baffle, right-angle baffle, and inclined baffle are 0.03%, 0.03%, and 0.03%, respectively; all of which are less than 1%. This demonstrates that the BP-NN model accurately predicts the equipment's operation time under different operating conditions, with relative errors within the acceptable range for engineering applications.

Notably, the straight and right-angle baffle prediction samples exhibit similar operation time prediction results to the inclined baffle, and thus are not repeated here.

5.3. Genetic algorithm optimization

Genetic algorithm (GA) is a widely used global search method. The selection of an appropriate optimization algorithm is crucial for the efficiency and effectiveness of the intelligent optimization framework. Several AI-based optimization methods are available, each with distinct characteristics. For instance, PSO is renowned for its simple implementation and rapid convergence in the early stages, but it may struggle with complex multi-modal problems and is prone to premature convergence [31]. Reinforcement learning (RL) excels in sequential decision-making processes and can handle dynamic environments, yet it typically demands substantial computational resources and interaction data, which is prohibitive for computationally expensive simulations like DEM [32].

In contrast, GA was chosen for this study due to its well-established capability in handling non-linear, multi-parameter optimization problems with discontinuous and complex search spaces, which aligns well with the characteristics of our parameter-response model. Its global search ability, derived from operations such as selection, crossover, and mutation, reduces the risk of being trapped in local optima. Furthermore, the coupling of GA

with the BP-NN creates a powerful surrogate-based optimization strategy [33]. The BP-NN provides a rapid and accurate prediction of the objective function (operation time), effectively replacing the computationally intensive DEM simulations during the iterative optimization process. This GA-BP synergy offers a balanced approach between global exploration and computational efficiency for our specific problem.

In this study, the shortest running time when the equipment reaches the set temperature is taken as the optimization objective, and the filling degree, rotational speed, and mixing index of the furnace are optimized under different baffle structures. The optimization results indicate that the operation time required to reach the target temperature can be reduced by approximately 20–30% compared to the baseline conditions, which is expected to significantly lower energy consumption and production costs. In addition, increasing the heating rate can accelerate the breaking of valence bonds of organic matter, thus increasing the generation of reaction products. At the same time, rapid heating will increase the temperature gradient inside and outside the particles, which is conducive to the escape of the reaction products and shortens their residence time. This not only helps reduce secondary reactions and cracking of volatile products, ultimately improving the shale oil yield, but also contributes to enhancing the product quality of shale oil.

The parameter settings of GA are shown in Table 2.

Table 2. Optimization parameter settings in genetic algorithms

Optimization parameter	Description	Range
Objective functions	Operation time	min
Optimization variables	Particle filling degree	0.30.5
	Furnace rotational speed	3–5 rpm
	Mixing index	0.18–0.25
Constraints	Average temperature of oil shale particles	500–550 °C
Initial parameters	Generation number	100
	Population size	200
	Selection rate	Tournament
	Crossover probability	0.8
	Mutation rate	Adaptive feasible

Figure 8 illustrates the iterative evolution of fitness values during genetic algorithm optimization for minimizing operation time when the average temperature of oil shale particles reaches 520 °C under three baffle configurations: straight, right-angle, and inclined. The figure clearly reflects the convergence characteristics of the optimization process and its effect.

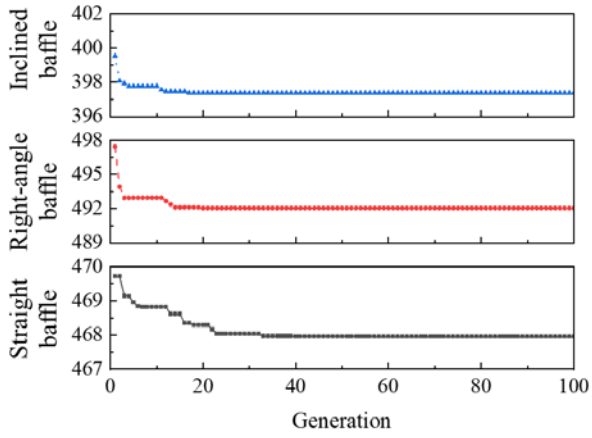

Fig. 8. Iterative optimization of fitness values for straight, right-angle, and inclined baffles at 520 °C.

From the curve trends, the algorithm rapidly improves fitness values within the first 20 generations, then enters a smooth convergence stage, and stabilizes at around 50 generations. The maximum fitness value converges to approximately 0.82.

Table 3 presents the shortest operation times and optimized parameter combinations for straight, right-angle, and inclined baffles to reach the 520 °C operating temperature. As depicted in Table 3, the inclined baffle demonstrates the highest thermal efficiency, reaching the target temperature in only 397 s, followed by the straight baffle (468 s) and the right-angle baffle (492 s). It is noteworthy that while the right-angle baffle exhibited the best mixing and temperature uniformity in the DEM analysis (Section 4.2), the inclined baffle achieved the shortest operation time in the global optimization. This highlights the distinction between optimizing for a single physical objective (e.g., mixing uniformity) and a comprehensive process objective (e.g., minimum time to reach a target temperature), and underscores the value of the integrated DEM-NN-GA framework in identifying such nuanced optimal solutions. Under optimal conditions, the mixing index of all three structural designs stabilizes at 0.18, whereas the filling degree parameters exhibit significant differences.

While traditional DEM simulations accurately analyze particle motion [17–22], they consume substantial computational resources to determine optimal conditions. In contrast, the genetic algorithm-based optimization method overcomes this limitation by establishing nonlinear mapping relationships between parameters and operation time, enabling rapid prediction of reasonable process parameter combinations and significantly improving optimization efficiency. This data-driven approach, integrating simulation with intelligent algorithms, addresses the challenge of multi-parameter coupling optimization

that is difficult to resolve through traditional numerical or experimental methods alone [15, 23]. This approach provides a new research idea and technical pathway for optimizing complex multi-parameter coupled systems.

Figure 9 illustrates the minimum operation time required for the furnace to achieve operation temperatures of 500 °C, 510 °C, 520 °C, 530 °C, 540 °C, and 550 °C for straight, right-angle, and inclined baffles. Results show that for all baffle structures, the minimum operation time increases with increasing operation temperature.

Comparing optimization results across baffle structures for the same operating temperature, the inclined baffle requires the shortest operation time, followed by the straight baffle and then the right-angle baffle. This indicates that under multi-parameter coupling, the inclined baffle exhibits the fastest

Table 3. Optimization results for straight, right-angle, and inclined baffles at 520 °C

Baffle shape	Optimization goal	Optimization variable		
	Time	Filling degree	Rotational speed, rpm	Mixing index
Straight baffle	467	0.36	5.00	0.18
Right-angle baffle	492	0.30	3.00	0.18
Inclined baffle	397	0.32	3.00	0.18

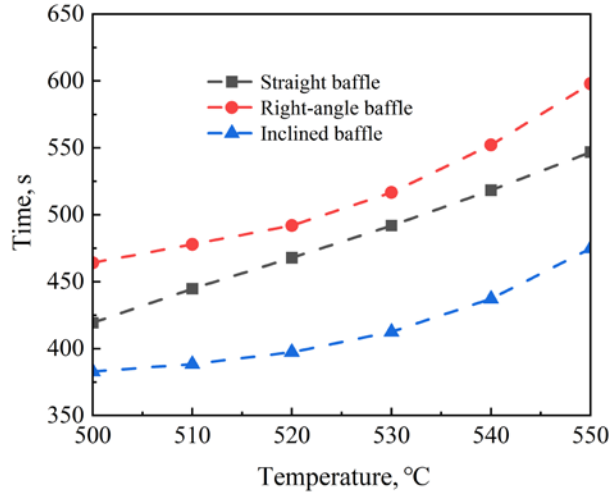

Fig. 9. Minimum operation time for straight, right-angle, and inclined baffles under different operating temperatures.

heating rate, followed by the straight baffle, with the right-angle baffle having the slowest heating rate. This finding provides a complementary perspective to the structural optimization studies exemplified by Liang et al. [14], demonstrating that the "optimal" structure can vary depending on the specific performance metric chosen for optimization.

Figure 10 shows the distribution of decision variables (filling degree, rotational speed, and mixing index) for optimizing the shortest operation time of different baffle structures under varying operating temperatures.

Figure 10(a) indicates that the filling degree for the straight baffle ranges from 0.35–0.40, decreasing with increasing operating temperature. For both the right-angle and inclined baffles, the filling degree distribution interval is 0.30–0.35. Notably, the filling degree of the right-angle baffle decreases with temperature, while that of the inclined baffle increases.

Figure 10(b) reveals that the rotational speed for the right-angle baffle ranges from 4.4–5.0 rpm. At 500 °C, the optimal condition uses 4.85 rpm, whereas other optimal conditions adopt 3.0 rpm. In contrast, the inclined baffle maintains a constant rotational speed of 3.0 rpm across all temperatures. The straight baffle's rotational speed increases with temperature, reaching 5.0 rpm at 520–550 °C. Evidently, rotational speed has a minimal impact on the minimum operation time across different baffles and temperatures.

Figure 10(c) shows that the mixing indices of the straight and right-angle baffles follow a similar trend: 0.25 at 500 °C and 0.18 at 510–550 °C. For the inclined baffle, the mixing index remains 0.18 at 500–530 °C and increases with further temperature rises. These distributions of filling degree, rotational speed, and mixing index provide a basis for equipment operation control.

(a)

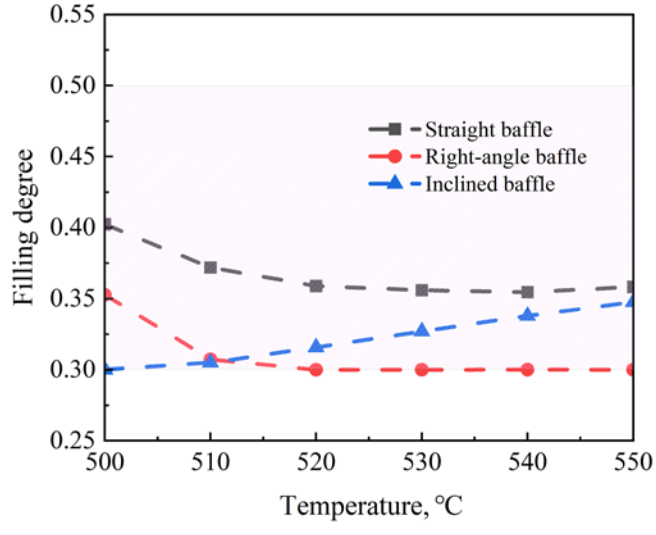

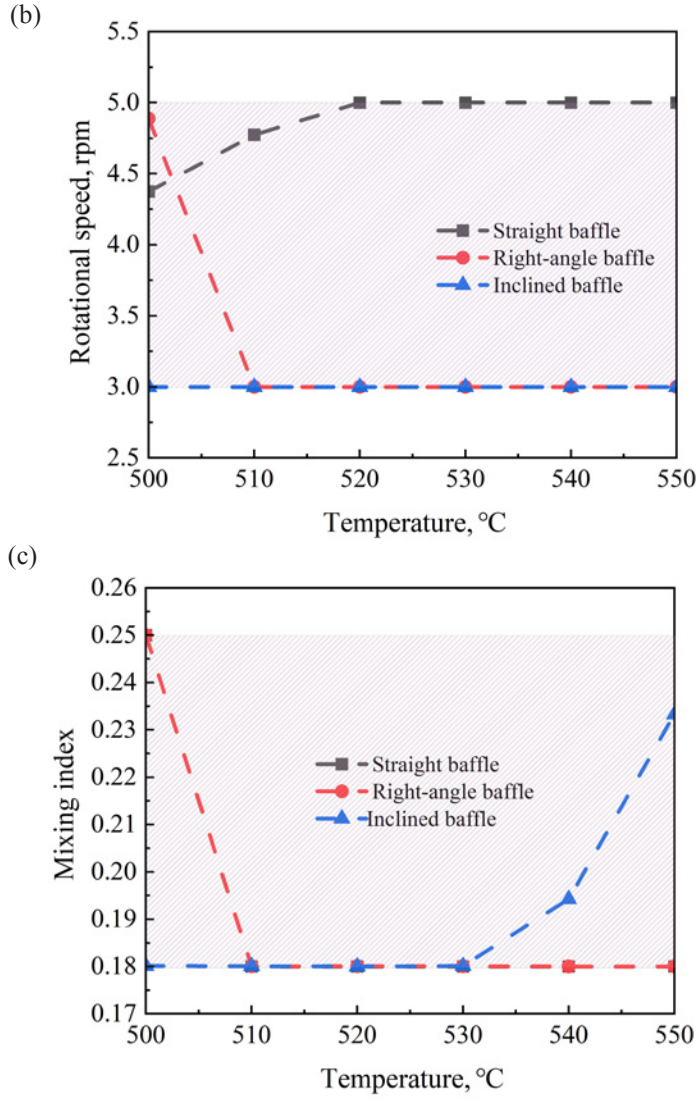

Fig. 10. Distribution of decision variables for different baffle structures under different operating temperatures: filling degree (a), rotational speed (b), and mixing index (c).

6. Conclusions

This study establishes an intelligent optimization framework for particle mixing and heat transfer in rotary retorting furnaces by integrating the discrete element method (DEM), backpropagation neural network (BP-NN), and genetic algorithm (GA). DEM simulations were first conducted to generate foundational data, based on which a BP-NN model was developed to predict

operation time. Subsequently, GA was employed for global optimization of key operational parameters to minimize the time required to reach the target temperature. The main findings are summarized as follows:

1. The established BP-NN prediction model demonstrates excellent accuracy, with a maximum relative error between predicted and actual operation times not exceeding 0.25%. This model effectively overcomes the limitations of traditional DEM simulations, such as high computational cost and long calculation time, providing an efficient tool for operational optimization.
2. The optimization framework integrating BP-NN and GA proves highly effective for multi-parameter coupling optimization in rotary retorting furnaces. By establishing a nonlinear mapping among key parameters, it enables the rapid identification of optimal settings for different baffle shapes. The results reveal a nuanced finding: while the right-angle baffle excelled in mixing and temperature uniformity in isolated analysis, the inclined baffle achieved the shortest operation time under global optimization, underscoring the importance of a system-level approach. Consequently, the optimal parameter combinations derived by GA provide clear guidance for industrial operation, promising to shorten production cycles by approximately 20–30%, reduce energy consumption, and enhance shale oil yield and quality by minimizing secondary reactions.
3. While the GA-BP framework demonstrated superior performance here, it is instructive to acknowledge its position relative to other AI paradigms. Future work could involve a comparative analysis with other meta-heuristics (e.g., particle swarm optimization) within the same surrogate-assisted framework. For scenarios requiring real-time adaptive control, exploring hybrid strategies – such as leveraging the trained network within a model-based reinforcement learning framework – presents a promising direction, despite the associated computational challenges.

Data availability statement

All data, models, and code generated or used during this study are included in the article.

Acknowledgments

This work was financially supported by the Liaoning Provincial Department of Education through a local project (No. JYTMS20231421). The publication costs of this article were partially covered by the Estonian Academy of Sciences.

References

1. Chen, B., Wu, J., Zhang, Y. Data-driven analysis and insights into sorption-induced kerogen deformation in shale. *Gas Science and Engineering*, 2025, **136**, 205579. https://doi.org/10.1016/j.jgsce.2025.205579
2. Yin, X., Cao, Z., Cao, C., Lü, N. Simulation and optimization in shale oil condensation recovery system. *Journal of Petrochemical Universities*, 2019, **32**(3), 20–27. https://doi.org/10.3969/j.issn.1006-396X.2019.03.004
3. Jia, B., Su, J. Advancements and environmental implications in oil shale exploration and processing. *Applied Sciences*, 2023, **13**(13), 7657. https://doi.org/10.3390/app13137657
4. Guo, C., Zou, T., Pan, H., Lu, H., Hu, H. Effect of transition metal salt catalysts on pyrolysis of Fushun oil shale. *Journal of Liaoning Petrochemical University*, 2021, **41**(3), 15–22. https://doi.org/10.3969/j.issn.1672-6952.2021.03.003
5. Ma, Y., Xiang, Q., Ding, K. Development of oil shale at home and abroad. *World Petroleum Industry* (China), 2024, **31**(1), 16–25. https://doi.org/10.20114/j.issn.1006-0030.20231108001
6. Li, J. *Simulation Research on Particle Heat Transfer Process in a Solid Heat Carrier Rotary Retorting for Oil Shale*. Master's thesis. Northeast Electric Power University, China, 2018.
7. Zhang, L., Wei, Q., Wang, Q. Influence of flights' shape on motion and mixing of binary particles in rotary retort. *Journal of Zhejiang University (Engineering Science)*, 2018, **52**(8), 1542–1550. https://doi.org/10.3785/j.issn.1008-973X.2018.08.014
8. Li, S., Zhang, L., Zhang, X., Yu, K., Wang, Q., Hao, W. Numerical analysis of particle mixing and movement in rotary retorting. *Proceedings of the CSEE*, 2011, **31**(2), 32–38.
9. Bisulandu, B.-J. R. M., Huchet, F. Rotary kiln process: an overview of physical mechanisms, models and applications. *Applied Thermal Engineering*, 2023, **221**, 119637. https://doi.org/10.1016/j.applthermaleng.2022.119637
10. Seidenbecher, J., Herz, F., Meitzner, C., Specht, E., Wirtz, S., Scherer, V. et al. Experimental analysis of the flight design effect on the temperature distribution in rotary kilns. *Chemical Engineering Science*, 2021, **240**, 116652.
11. He, Y., E, D., Lai, N. C., Jiang, Z. Influence of flight structures and baffle dam on particle behaviors and gas-solid heat exchange enhancement in a rotary drum. *Particuology*, 2025, **102**, 104–117. https://doi.org/10.1016/j.partic.2025.04.010
12. Zhang, L., Li, S., Yu, K., Zhang, X., Wang, Q. Cold experiments on mixing performance of oil shale particle and solid heat carrier in rotary retorting. *Chemical Industry and Engineering Progress*, 2011, **30**(3), 492–497.
13. Herz, F., Mitov, I., Specht, E., Stanev, R. Influence of operational parameters and material properties on the contact heat transfer in rotary kilns. *International Journal of Heat and Mass Transfer*, 2012, **55**(25–26), 7941–7948. https://doi.org/10.1016/j.ijheatmasstransfer.2012.08.022

14. Liang, R., Zhang, Z., Jin, Z., Yu, X., Zhang, S. Engineering application of indirect heating rotary kiln in oil shale pyrolysis treatment. *Chinese Journal of Environmental Engineering*, 2021, **15**(9), 3029–3034.
15. Nabilah, A. J., Satritama, B., Hidayat, T., Taskinen, P., Santoso, I., Kurniadani, H. et al. Reduction of saprolite nickel ore using methane-argon gas mixture with laboratory-scale simulated rotary kiln-electric furnace (RKEF) technology. *Minerals Engineering*, 2025, **234**, 109776. https://doi.org/10.1016/j.mineng.2025.109776
16. Li, J., Sun, T., Wen, L. Multi-objective evaluation of optimization of direct evaporative cooling air supply mode in rotary kiln process section. *Refrigeration and Air Conditioning*, 2025, **39**(1), 56–65.
17. Hu, J., Zhang, L., Wang, B., Kisuka, F., He, Y., Wang, Z. et al. A robust DEM framework for efficient simulation of heat generation in long-duration recurrent granular flows. *Powder Technology*, 2025, **465**, 121308. https://doi.org/10.1016/j.powtec.2025.121308
18. Wu, H., Li, W., Wang, J., Zhan, M., Gu, H., Xu, P. et al. Drying characteristics of soil in large-scale rotary kilns: an experimental and CFD-DEM study. *Drying Technology*, 2025, **43**(3), 527–540. https://doi.org/10.1080/07373937.2024.2436505
19. Arntz, M. M. H. D., den Otter, W. K., Briels, W. J., Bussmann, P. J. T., Beeftink, H. H., Boom, R. M. Granular mixing and segregation in a horizontal rotating drum: a simulation study on the impact of rotational speed and fill level. *AIChE Journal*, 2010, **54**(12), 3133–3146. https://doi.org/10.1002/aic.11622
20. Wang, Q., Li, J., Wang, Z., Zhang, L. Numerical simulation on characteristics of heat transfer between particles in rotary retorting. *CIESC Journal*, 2017, **68**(11), 4137–4146. https://doi.org/10.11949/j.issn.0438-1157.20170147
21. Wang, Q., Liu, B. W., Wang, Z. C. Investigation of heat transfer mechanisms among particles in horizontal rotary retorts. *Powder Technology*, 2020, **367**, 82–96. https://doi.org/10.1016/j.powtec.2020.03.042
22. Xie, Q., Chen, Z. B., Hou, Q. F., Yu, A. B., Yang, R. DEM investigation of heat transfer in a drum mixer with lifters. *Powder Technology*, 2017, **314**, 175–181. https://doi.org/10.1016/j.powtec.2016.09.022
23. Wang, M., Chen, E., Liu, P., Guo, W. Multivariable nonlinear predictive control of a clinker sintering system at different working states by combining artificial neural network and autoregressive exogenous. *Advances in Mechanical Engineering*, 2020, **12**(1), 1687814019896509. https://doi.org/10.1177/1687814019896509
24. Li, T., Zhang, Z., Chen, H. Predicting the combustion state of rotary kilns using a convolutional recurrent neural network. *Journal of Process Control*, 2019, **84**, 207–214. https://doi.org/10.1016/j.jprocont.2019.10.009
25. Ko, M. S., Chang, T. B., Lee, C. Y., Huang, J. W., Lim, C. F. Optimization of cyclone-type rotary kiln reactor for carbonation of BOF slag. *Sustainability*, 2021, **13**(20), 11556. https://doi.org/10.3390/su132011556

26. Zhang, R. F. *Research on State Recognition and Intelligent Optimization Method of Cement Clinker Calcination Process*. PhD thesis. University of Jinan, China, 2023.
27. Wang, C., Sun, Y., Wang, N., Sun, J., Yue, Y. Study on the influence of baffles on heat transfer characteristics of particles in an oil shale rotary kiln. *Applied Thermal Engineering*, 2025, **268**, 125924. https://doi.org/10.1016/j.applthermaleng.2025.125924
28. Zhou, Z. Y., Yu, A. B., Zulli, P. Particle scale study of heat transfer in packed and bubbling fluidized beds. *AIChE Journal*, 2009, **55**(4), 868–884. https://doi.org/10.1002/aic.11823
29. Chaudhuri, B., Muzzio, F. J., Tomassone, M. S. Modeling of heat transfer in granular flow in rotating vessels. *Chemical Engineering Science*, 2006, **61**(19), 6348–6360. https://doi.org/10.1016/j.ces.2006.05.034
30. Nafsun, A. I., Herz, F., Liu, X. Influence of material thermal properties and dispersity on thermal bed mixing in rotary drums. *Powder Technology*, 2018, **331**, 121–128. https://doi.org/10.1016/j.powtec.2018.01.072
31. Kant, R., Maurya, S. P., Singh, K. H. Qualitative and quantitative reservoir characterization using seismic inversion based on particle swarm optimization and genetic algorithm: a comparative case study. *Scientific Reports*, 2024, **14**(1), 22581. https://doi.org/10.21203/rs.3.rs-3141822/v1
32. Michailidis, P., Michailidis, I., Kosmatopoulos, E. Reinforcement learning for optimizing renewable energy utilization in buildings: a review on applications and innovations. *Energies*, 2025, **18**(7), 1724. https://doi.org/10.3390/en18071724
33. Jin, L., Duan, J., Fan, T., Jiao, P., Dong, T., Wu, Q. Using GA-BP coupling algorithm to predict the high-performance concrete mechanical property. *KSCE Journal of Civil Engineering*, 2023, **27**(2), 684–697. https://doi.org/10.1007/s12205-022-0912-9

Oil Shale, 2026, 43, 2, 165–196 https://doi.org/10.3176/oil.2026.2.03

Optimization of oil shale retorting process based on heat transfer model

Chunhua Wang[(a)]*, Yufeng Wu[(a)], Chunhui Wang[(b)], Ningning Li[(a)]*, Lina Liu[(a)], Chengdong He[(a)], Jiang Liu[(a)], Yue Yue[(a)], Haodan Pan[(a)], Zhiyong Hu[(c)], Yulin Yan[(d)]

[(a)] College of Mechanical Engineering, Liaoning Petrochemical University, Fushun 113001, China
[(b)] China National Energy Group Ledong Power Generation Co. Ltd., Ledong 572539, China
[(c)] College of Petroleum Engineering, Liaoning Petrochemical University, Fushun 113001, China
[(d)] Fushun Mining Group Co. Ltd., Fushun 113009, China

Received 8 February 2025, accepted 8 April 2026, available online 16 April 2026

Abstract. *To optimize the oil shale retorting process and improve the thermal efficiency of the retort, a heat transfer model of the oil shale retorting in the Fushun-type retort was established based on the gas-solid heat transfer equation. The orthogonal experimental method was used, with hot air volume (A), hot recycle gas temperature (B), and oil shale interparticle porosity (C) taken as the investigation factors, and the retort height required for the retorting of the same quality oil shale as the metric of the thermal efficiency of the retort. The smaller the retort height, the higher the thermal efficiency of the retort. Range and variance analyses revealed that the effects of the three factors on retort height are, from large to small: A > B >C; this shows that hot air volume (A) exerts the most significant influence. Based on this, computational fluid dynamics simulation was conducted on the hot air volume parameter. The study shows that increasing the hot air volume can effectively increase the heat supply proportion of the generated gas in the retorting process to 59.288%. To maintain the height of the high-temperature zone in the reaction section, it is proposed to increase the oxygen content in the hot air volume, which proves the feasibility of oxygen-enriched retorting.*

Keywords: *oil shale retorting, heat transfer model, orthogonal experimental, hot air volume.*

* Corresponding authors, wangchunhua@lnpu.edu.cn, lining773239@163.com

1. Introduction

Oil shale is a kerogen-rich sedimentary rock that can be broken down when heated to produce shale oil and pyrolysis gas. Its global reserves far exceed those of traditional oil, making it a valuable energy resource for countries such as the United States, Russia, and China. Oil shale under air-isolated conditions can be subjected to low-temperature retorting to obtain shale oil, shale semi-coke, and pyrolysis gas. Among the existing ground-based retorting processes for industrial production, the gas heat-carrier retorting process is the most widely used, such as Brazil's Petrosix process, Estonia's Kiviter process, the U.S. SGR process, Japan's Joseco process, and China's Fushun retorting process. The Fushun-type retort is equipment for oil shale retorting that uses hot recycle gas as a heat carrier, and it has achieved the largest commercial production in China [1].

Many operating parameters affect the thermal efficiency of oil shale retorting. Many scholars have analyzed the effects of typical parameters on the retorting process of oil shale, including heating rates, grain size of oil shale, pyrolysis process temperature, and residence time of oil shale. Wang et al. [2, 3] investigated the effects of different heating rates on the density, viscosity, boiling point, cloud point, and calorific value of shale oil during pyrolysis of oil shale. Nazzal [4] showed that shale oil coking at higher heating rates leads to lower yields. This may be because the temperature difference between the core and oil shale surface increases significantly as the heating rate rises during the pyrolysis process. Geng et al. [5] found that the shale oil yield increases significantly during oil shale pyrolysis at temperatures ranging from 300 to 500 °C and decreases above 500 °C due to the enlargement of oil shale pores and secondary decomposition of pyrolysis products. Pan et al. [6] conducted a similar study. The results demonstrate that oil shale yield is positively correlated with temperatures from 350 to 520 °C and negatively correlated at temperatures ranging from 520 to 600 °C. Experiments by Xu et al. [7] showed that increasing the residence time can improve the physical properties of oil shale, but a residence time that is too long can lead to secondary decomposition of oil and gas. Han et al. [8] used gas chromatography–mass spectrometry to extract and characterize the organic compounds in shale coke under different pyrolysis conditions. A prolonged residence time leads to the enrichment of aromatic hydrocarbons and nitrogenous organic compounds in oil shale coke, resulting in lower shale oil grades. Khalil [9] indicated that the particle size of oil shale affects mass transfer, heat transfer, and secondary reactions during pyrolysis, and that an increase in particle size leads to a decrease in total weight loss and gas weight loss, as well as a decrease in the amount of oil produced. Tang [10] conducted a study on samples with different grain sizes and performed thermogravimetric analysis. These results are consistent with those of previous assessments. However, in the oil shale retorting process, the influence of relevant operating parameters on the retort's thermal efficiency remains poorly understood.

Moreover, it is unclear which of these parameters have the most significant impact and which can be neglected.

Therefore, a numerical heat transfer model was established for oil shale retorting in the Fushun-type retort based on the gas-solid heat transfer equation in this work. The specific effects of the three typical parameters – hot air volume, hot recycle gas temperature, and oil shale interparticle porosity – on the heat utilization efficiency of the retort were discussed, the key factors affecting the thermal efficiency of the retort were determined, and effective improvement measures to improve the thermal efficiency of the retort were proposed.

2. Research object and methods

2.1. Research object

The Fushun-type retort can be divided into three sections from top to bottom [11]: drying, retorting, and gasification sections, as shown in Figure 1. The process flow for each section is as follows:

(1) Drying section

Oil shale with a particle size between 12 and 75 mm is fed into the retort from the top via the feeding device and then enters the drying section, flowing in a top-down direction. In the drying section, the oil shale comes into counter-current contact with the upward-flowing shale oil and gas mixture. It is heated to a temperature of 100–150 °C, causing the moisture within it to be released. The released moisture rapidly evaporates into steam and mixes with the oil and gas mixture, thus completing the drying process. Subsequently, the shale oil and gas mixture carrying the steam is led out of the retort through the gas collection umbrella.

(2) Retorting section

The dried oil shale exchanges heat with the hot recycle gas that passes through the section, as well as with the hot gas mixture flowing from the lower gasification section. Specifically, when the oil shale is heated to 330 °C, low-boiling-point volatile fractions start to form. In the temperature range of 350–550 °C, the oil shale releases a large amount of tar. The generated tar gases volatilize upward and are then led out through the gas collection umbrella.

(3) Gasification section

The gasification section is primarily located in the lower part of the retort, where reduction reactions and oxidation reactions mainly occur. In the reduction reaction, after semi-coke from the retorting section absorbs physical heat from hot gases generated in the oxidation reaction, some fixed carbon in the semi-coke reacts with water vapor to generate CO and H_2. The resulting water gas combines with gases from the gasification section to form a gas mixture that rises into the upper retorting section, while the semi-coke moves downward to undergo oxidation reactions.

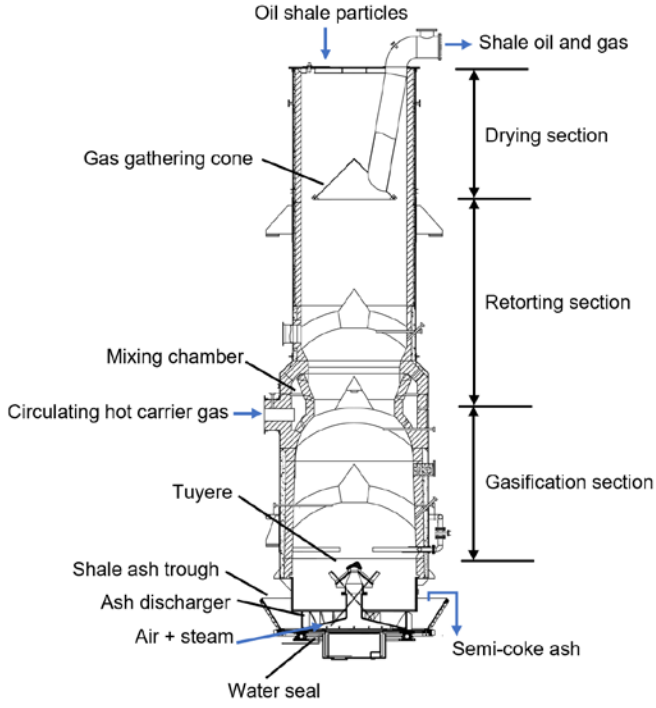

Fig. 1. Schematic structure of each section of the oil shale retort.

In the oxidation reaction, the fixed carbon in the shale semi-coke undergoes a vigorous oxidation reaction with the saturated air at 75–85 °C that is fed in, generating high-temperature products with a temperature greater than 700 °C, such as CO_2, CO, and shale ash. The newly formed gases mix with N_2 in the air to form a gas mixture. The gas mixture offers essential heat for the semi-coke reduction gasification reaction. At the same time, the shale ash produced by the reaction enters the cooling section.

2.2. Establishment of mathematical models

2.2.1. Modeling method

By discretizing the heat exchange field inside the retort, the energy balance equations for each section of the retort were established. These equations form a system of equations that can be solved discretely to effectively describe the characteristics of the high-temperature heat exchange field [12, 13].

Figure 2 shows the input and output parameters of the mathematical model. The accuracy and comprehensiveness of these parameters are crucial for the validity of the model. By properly selecting and adjusting these parameters, the complexity and dynamic changes within the heat exchange field in the retort can be captured more accurately [14]. The model's input parameters cover all aspects of the heat exchange field, whereas the output parameters provide key information about the simulation results.

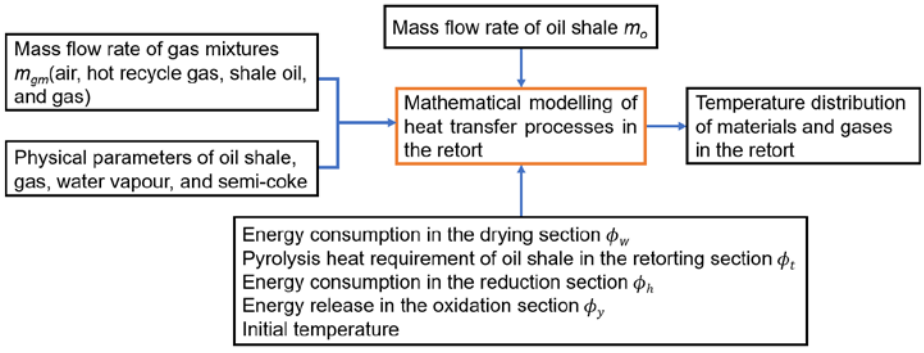

Fig. 2. Input and output parameters of mathematical models of heat transfer processes.

Table 1. Parameters specified in the modeling

Parameter	Value
Oil shale initial temperature	23 °C
Oil shale particle size	12~75 mm
Thermal conductivity of oil shale	1 W/(m·K) [15]
Apparent density of oil shale	1900 kg/m^3
Oil shale specific heat capacity	967 J kg^{-1} °C^{-1}
Oil shale moisture content	7.5%
Hot recycle gas density	1.22 kg/m^3
Shale ash specific heat	1088 J kg^{-1} °C^{-1}
Density of mixed gas	1.08 kg/m^3 [16]
Hot air density	1.293 kg/m^3
Loss factor of oil shale	0.069 [17]
Mean retort diameter	2750 mm
Mass flow rate of oil shale at inlet	1.375 kg/s
Mass flow rate of air at inlet	0.479 kg/s
Mass flow rate of hot recycle gas at inlet	0.289 kg/s

2.2.2. Assumptions

In view of the complex heat transfer process in the oil shale retorting, the following assumptions were made:

(1) It was assumed that the heat dissipation loss of the retort wall was negligible.

(2) It was assumed that the influence of radiation heat transfer in the retort was negligible.

(3) It was assumed that the material layer and gas properties were uniform within each section.

(4) The average particle size of oil shale particles in the actual retorting process was used instead of the actual particle size.

(5) The impact of heat transfer caused by the generation of oil and gas from the pyrolysis of organic matter during the oil shale retorting process was not considered.

2.3. Mathematical model

2.3.1. Theoretical basis of gas-solid convection heat transfer in oil shale retorts

During oil shale retorting, the solid material descends slowly and passes through the drying section. The hot recycle gas passes vertically through the material layer, exchanging heat with oil shale particles. This not only cools the semi-coke but also promotes the pyrolysis of the oil shale. The complex gas flow and heat transfer within the pores, owing to the small pore diameters and irregular shapes between the oil shale blocks, pose challenges for accurate mathematical simulation. Thus, the material layer was treated as a porous medium to account for heat transfer between the gas and solid phases.

The local non-thermal equilibrium double energy equation for convective heat transfer in porous media has been used to analyze the heat transfer process between gas and solid phases. Oil shale particles and gases were treated as distinct continuous media. Within the volume unit defined by the zones, the average temperatures of the gas and solid regions were determined and considered as the average temperatures of the gas phase and solid phase objects, respectively. These temperatures represent the thermal state within the same characteristic volume, and the heat transfer process within the porous medium is treated as a heat exchange between these two phases. The corresponding generalized system of equations is as follows:

$$\varepsilon\left(\rho c_p\right)_f \frac{\partial t_f}{\partial \tau} + \left(\rho c_p\right)_f v \cdot \nabla t_f = \nabla \cdot \left(\lambda_{feff} \nabla t_f\right) - h_{v,s-f}\left(t_f - t_s\right), \tag{1}$$

$$(1-\varepsilon)(\rho c_s)\frac{\partial t_s}{\partial \tau} = (1-\varepsilon)\nabla \cdot \left(\lambda_{seff} \nabla t_s\right) + h_{v,s-f}\left(t_f - t_s\right).^{1} \tag{2}$$

[1] For symbols used in the equations, please refer to the Nomenclature at the end of this article.

Equations (1) and (2) are the differential equations for gas-solid heat transfer. The heat transfer process within the retort can be simplified to a gas-solid heat transfer process within a porous medium, thereby avoiding the consideration of other complex heat transfer phenomena, such as solid-solid and gas-gas heat exchanges, during the analysis of discrete equations.

Given that adjacent oil shale blocks are in point contact and have a small thermal conductive area, and considering the small thermal conductivity of oil and gas in the gas stream, the thermal conductive fluxes between the material layers and between the gas stream and the material layers can be neglected in comparison to convective heat transfer. Therefore, the heat transfer between the gas and the material layer can be simplified to the expression shown below [16–20]:

$$\phi_{s-f} = h_{v,s-f}\left(t_s - t_f\right), \tag{3}$$

where the convective heat transfer coefficient $h_{v,s-f}$ per unit area between the material layer and gas can be determined by Achenbach's criterion relation [21, 22], as shown below:

$$h_{v,s-f} = \frac{6h_{sf}\left(1-\varepsilon\right)}{d_p}, \tag{4}$$

where h_{sf} is determined as follows:

$$Nu = \frac{h_{sf}d_p}{\lambda_f} = 2.0 + 0.6Pr^{1/3}Re^{1/2}. \tag{5}$$

In Equation (5), the values of *Pr* and *Re* can be obtained by solving the following equations:

$$Pr = \frac{\left(\mu c_p\right)_f}{\lambda_f}, \tag{6}$$

$$Re = \frac{\varepsilon\rho_r d_{\mathrm{p}} u}{\mu_{\mathrm{f}}}. \tag{7}$$

2.3.2. Mathematical modeling of oil shale retort

A discretization method was applied to solve the heat transfer process within the retort by dividing the entire heat transfer region into small sections. The temperature and physical parameters were assumed to be uniform within each section. By discretizing the heat-transfer region, an energy-balance equation can be established for each section. This series of equations forms a system, and by solving this system, it is possible to characterize the heat transfer between the gas and solid in a discrete manner. Figure 3 shows the heat-transfer process diagrams for these three sections.

The heat transfer equations for each section of the retort can be established based on the energy conservation equation and the heat transfer equation

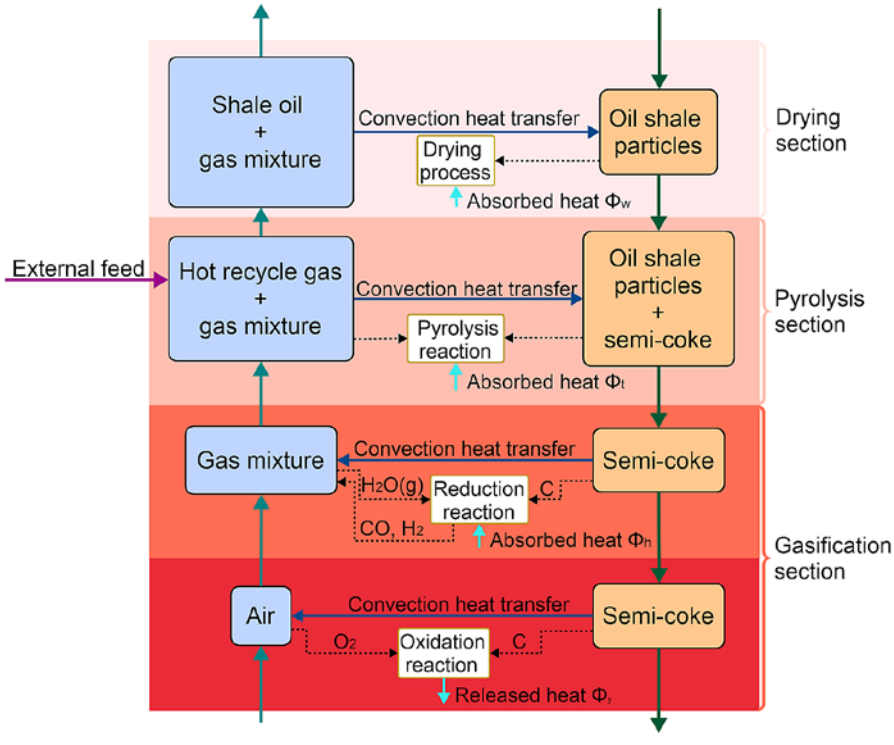

Fig. 3. Heat transfer process diagram for oil shale retort.

between gas and solid phases. It should be particularly noted that there is a unique source term in the energy conservation equation for each section. In the gasification section, the source term includes the chemical heat released by the combustion of semi-coke and the heat absorbed during the gasification of semi-coke; in the retorting section, the source term is the heat absorbed during the pyrolysis of oil shale; and in the drying section, the source term is the latent heat consumed by the evaporation of water. By accurately considering these source terms, the heat transfer process in each section of the retort can be more accurately described. The equations for each section are shown as Equations (8)–(11).

Gasification section:

(1) Oxidation reaction:

$$\begin{cases} \phi_{go-in} + \phi_{so-in} = \phi_{go-out} + \phi_{so-out} - \phi_y \\ \phi_{go-in} - \phi_{go-out} = m_{go,i-1} c_{go,i-1} t_{go,i-1} - m_{go,i} c_{go,i} t_{go,i} = -h_{o,i} V (t_{so,i} - t_{go,i}) - \phi_y \\ \phi_{so-in} - \phi_{so-out} = m_{so,i+1} c_{so,i+1} t_{so,i+1} - m_{so,i} c_{so,i} t_{so,i} = h_{o,i} V (t_{so,i} - t_{go,i}) \end{cases}, \quad (8)$$

(2) Reduction reaction:

$$\begin{cases} \phi_{gr-in} + \phi_{sr-in} = \phi_{gr-out} + \phi_{sr-out} + \phi_h \\ \phi_{gr-in} - \phi_{gr-out} = m_{gr,j-1} c_{gr,j-1} t_{gr,j-1} - m_{gr,j} c_{gr,j} t_{gr,j} = -h_{r,j} V (t_{sr,j} - t_{gr,j}) \\ \phi_{sr-in} - \phi_{sr-out} = m_{sr,j+1} c_{sr,j+1} t_{sr,j+1} - m_{sr,j} c_{sr,j} t_{sr,j} = h_{r,j} V (t_{sr,j} - t_{gr,j}) + \phi_h \end{cases} . \quad (9)$$

Retorting section:

$$\begin{cases} \phi_{gt-in} + \phi_{rws-in} + \phi_{st-in} = \phi_{gt-out} + \phi_{st-out} + \phi_t + \phi_{g-t} \\ \phi_{gt-in} + \phi_{rsw-in} - \phi_{gt-out} = m_{gt,k-1} c_{gt,k-1} t_{gt,k-1} - m_{gt,k} c_{gt,k} t_{gt,k} \\ = -h_{t,k} V (t_{st,k} - t_{gt,k}) + \phi_t + m_{t,k} c_{gt,k} (t_{gt,k} - t_{st,k}) \\ \phi_{st-in} - \phi_{st-out} = m_{st,k+1} c_{st,k+1} t_{st,k+1} - m_{st,k} c_{st,k} t_{st,k} = h_{t,k} V (t_{st,k} - t_{gt,k}) \end{cases} . \quad (10)$$

Drying section:

$$\begin{cases} \phi_{gd-in} + \phi_{sd-in} = \phi_{gd-out} + \phi_{sd-out} + \phi_w + \phi_{g-w} \\ \phi_{gd-in} - \phi_{gd-out} = m_{gd,m-1} c_{gd,m-1} t_{gd,m-1} - m_{gd,m} c_{gd,m} t_{gd,m} = -h_{d,m} A (t_{sd,m} - t_{gd,m}) \\ + m_w c_{w,m} (t_{gd,m} - t_{am}) \\ \phi_{sd-in} - \phi_{sd-out} = m_{sd,m+1} c_{sd,m+1} t_{sd,m+1} - m_{sd,m} c_{sd,m} t_{sd,m} = h_{d,m} V (t_{sd,m} - t_{gd,m}) + \phi_w \end{cases} . \quad (11)$$

2.3.3. Solution and validation of the model

(1) Solution of the model

Separately, the equations for the above four sections were linked to form a set of energy-balance equations for each model section. The solution model for the temperature field in each of these processes can be expressed in the form of a matrix equation:

$$[A]\vec{t} + \vec{C} = 0 . \quad (12)$$

To facilitate the model, the height of each model section was divided into 0.01 m. Assuming that there are N model sections in the retort, N_1 model sections are required for the gasification process of semi-coke, N_2 model sections for the retorting process of shale semi-coke; and N_3 model sections for the drying process of shale semi-coke, that is, $N = N_1 + N_2 + N_3$. The following gasification section was used as an example to establish a system of matrix equations to solve the problem, and the remaining three sections were listed in the same way.

(a) Matrix solver:

$$\vec{t}_1 = \left(t_{s,1}, t_{g,1}, \cdots, t_{s,i}, t_{g,i}, \cdots, t_{s,N_1}, t_{g,N_1} \right)^T . \quad (13)$$

Vector $\vec{t}_1$ has $2N_1$ elements.

Matrix $[A]_1$ is as follows:

$$[A]_1=\begin{pmatrix} h_{s-g}V & \psi_1 & 0 & 0 & 0 & \cdots & 0 & \cdots & 0 & 0 \\ \xi_1 & h_{s-g}V & m_{so,1}c_{so,1} & 0 & 0 & 0 & \ddots & 0 & 0 & 0 \\ 0 & m_{go,2}c_{go,2} & h_{s-g}V & \psi_2 & 0 & 0 & 0 & \ddots & 0 & 0 \\ 0 & 0 & \xi_2 & h_{s-g}V & m_{so,2}c_{so,2} & 0 & 0 & 0 & \ddots & 0 \\ 0 & 0 & 0 & \ddots & \ddots & \ddots & 0 & 0 & 0 & \vdots \\ 0 & 0 & 0 & 0 & m_{go,i}c_{go,i} & h_{s-g}V & \psi_i & 0 & 0 & 0 \\ \vdots & \ddots & 0 & 0 & 0 & \xi_i & h_{s-g}V & m_{so,i}c_{so,i} & 0 & 0 \\ 0 & 0 & \ddots & 0 & 0 & 0 & \ddots & \ddots & \ddots & 0 \\ 0 & 0 & 0 & \ddots & 0 & 0 & 0 & m_{go,N_1}c_{go,N_1} & h_{s-g}V & \psi_{N_1} \\ 0 & 0 & \cdots & 0 & \cdots & 0 & 0 & 0 & \xi_{N_1} & h_{s-g}V \end{pmatrix}. \quad (14)$$

Included among these:

$$\xi_i=-(m_{so,i}c_{so,i}+h_{o,i}V), \quad (15)$$

$$\psi_i=-(m_{go,i}c_{go,i}+h_{o,i}V). \quad (16)$$

Vector $\vec{C}$ is as follows:

$$\vec{C}=\begin{pmatrix} m_{go,0}c_{go,0}t_{go,0}+\phi_y \\ 0 \\ \vdots \\ \phi_y \\ 0 \\ \vdots \\ \phi_y \\ m_{so,N_1}c_{so,N_1}t_{so,N_1} \end{pmatrix}. \quad (17)$$

(b) Physicochemical reaction parameters in the model:

The temperature at which the pyrolysis of oil shale is initiated increases with the extent of retorting. The onset of pyrolysis for oil shale particles occurs at 180 °C. Consequently, it is assumed that the water within the oil shale particles evaporates linearly between 25 and 180 °C, and the volatile fraction precipitates linearly between 180 and 550 °C [23, 24]. The special heat release of each section in the oil shale retort is shown in Table 2.

Table 2. Heat composition of each section in the retort

Pyrolytic heat release characteristics of materials in the retort	Symbol	Calorific value
Heat released by unit mass of solid combustion in the oxidation reaction	q_o	32791670 J/kg
Heat absorbed by unit mass of solid in the redox reaction (water-gas reaction)	q_r	7508300 J/kg
Heat required for releasing volatiles via pyrolysis of unit mass of solid in the retorting section	q_t	235559 J/kg [25]
Latent heat of water evaporation and gasification in the drying section	q_d	2442000 J/kg [26]

Gasification section

Oxidation reaction:

$$\begin{cases} m_y = \dfrac{m_{y,all}}{N_1} \\ \phi_y = q_o \times m_y \\ m_{go,i} = m_{go,0} + (i-1) \times m_y \\ m_{so,i} = m_{so,0} + i \times m_y \end{cases}. \tag{18}$$

Reduction reaction:

$$\begin{cases} m_h = \dfrac{m_{h,all}}{N_2} \\ \phi_h = q_r \times m_h \\ m_{\mathrm{gr},j} = m_{go,N_1} + (j-1) \times m_h \\ m_{sr,j} = m_{so,N_1} + j \times m_h \end{cases}. \tag{19}$$

Retorting section:

$$\begin{cases} m_t = \dfrac{m_{t,all}}{N_3} \\ \phi_t = q_t \times m_t \\ m_{gt,k} = m_{gr,N_2} + (k-1) \times m_t \\ m_{st,k} = m_{sr,N_2} + k \times m_t + m_{chc} \end{cases}. \tag{20}$$

Drying section:

$$\begin{cases} m_w = \dfrac{m_{w,all}}{N_4} \\ \phi_w = q_d \times m_w \\ m_{gd,m} = m_{gt,N_3} + (m-1) \times m_w \\ m_{sd,m} = m_{st,N_3} + m \times m_w \end{cases} . \quad (21)$$

(2) Validation of the model

To validate the accuracy of the mathematical simulation method, this study compared and analyzed the numerical simulation results of the gas-phase temperature distribution within the retort against real-time monitoring data of gas phase temperature distribution obtained during actual industrial production processes. The specific measurement locations and comparative results are shown in Figures 8 and 4, respectively. The comparative analysis results indicate that the maximum relative deviation between the measured gas-phase temperature data and the simulation results is within 8%. Although a certain margin of error exists, considering the simplified assumptions of the model and the requirements of practical engineering applications, this level of deviation is deemed reasonably acceptable. These findings validate the reliability of the computational model in reflecting the actual thermodynamic characteristics under operating conditions.

3. Results and discussion

3.1. Gas-solid temperature distributions

Figure 5 depicts the temperature distributions of the oil shale particles and mixed gas, as well as the temperature differences between them, within the chamber of a gas retort. The retorting process was conducted at 520 °C, with oil shale particles having a porosity of 0.5.

Within the retort, the gas-solid phase exhibits typical counter-current heat transfer characteristics along the retort height direction.

At ambient temperature, the oil shale is fed from the retort top and gradually descends under gravity. Oil shale is progressively heated via thermal exchange through intensive contact with the upward-flowing hot gas carrier. Oil shale undergoes sequential drying and retorting processes, yielding oil vapors and semi-coke. During this process, the gas phase is cooled and the oil vapors become gaseous components. Concurrently, the hot recycle gas is introduced into the retorting section, transferring its thermal energy to the oil shale. This causes a certain degree of temperature elevation in the gas phase. Finally, the gas phase exits the retort at approximately 120 °C.

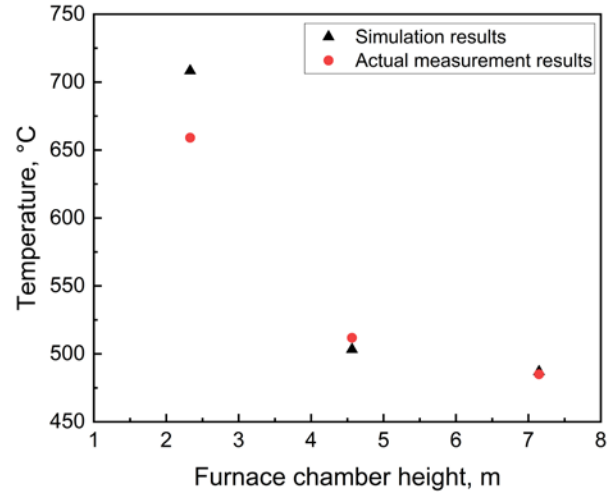

Fig. 4. Comparison of simulation and experiment.

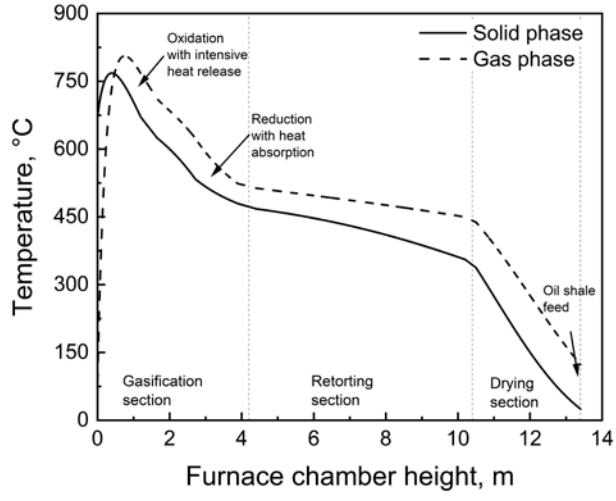

Fig. 5. Gas-solid temperature distribution.

The semi-coke moves downward into the gasification section, where it fully contacts and absorbs heat from the gas phase, undergoing the water-gas shift reaction. This effectively prevents excessive temperature elevation of the semi-coke, maintaining it stably between 500–550 °C. During this process, the gas phase is cooled, and the gaseous products generated from the water-gas shift reaction also join the gas phase.

The semi-coke unreacted in the reduction reaction continues to move downward, mixes with air supplied from the bottom, and undergoes oxidative

combustion. During this process, the semi-coke reacts completely with oxygen, releasing substantial heat that causes its temperature to rise rapidly to approximately 750 °C. Simultaneously, the high-temperature combustion products enter the gas phase, elevating the gas temperature significantly to around 850 °C. During combustion, the semi-coke is converted into high-temperature semi-coke ash, which exchanges heat with the cold air introduced from the bottom of the retort. The heat from the semi-coke ash is transferred to the cold air, causing a decrease in its temperature, while the temperature of the gas phase is further increased. Ultimately, the semi-coke ash is cooled to around 65 °C, and then discharged from the retort.

Changes in parameters such as hot air volume, hot recycle gas temperature, and porosity affect the heat transfer process and heat transfer intensity inside the retort. Specifically, the variation in porosity (as shown in Eq. (5)) influences the gas-solid heat transfer coefficient. Meanwhile, the hot air volume and hot recycle gas temperature alter the thermophysical properties of the mixed gas in the retort and the gas mass involved in reactions at different stages. These changes further affect the heating degree of oil shale particles, leading to variations in both the location where oil shale undergoes retorting and the time required for complete retorting. Under different parameter conditions, the reasonable retort height is defined as the height at which oil shale just finishes pyrolysis inside the retort. This height ensures no redundant space while avoiding impacts on product yield and quality.

The curve distribution of the retort temperature varying with height in Figure 5 indicates that, to achieve the retorting of oil shale, the actual length of each section of the retort body derived from production data is as follows: the gasification section is 4.2 m high, the retorting section is 6.2 m high, and the drying section is 3.0 m high, with the total height of the retort being 13.4 m. For the current Fushun-type retort in the plant, the internal reaction height (excluding the ashtray and air distributor head) measures 12.6 m. The relative error between this measured height and the mathematically simulated height is 6.3%. Although this error exists, it falls within an acceptable range, which also verifies the feasibility of the mathematical simulation.

3.2. Analysis of the effect of thermodynamic parameters on the retorting process

3.2.1. Orthogonal experimental design data and orthogonal table

In this study, an orthogonal experiment was carried out. Its purpose was to analyze how hot air volume, hot recycle gas temperature, and oil shale interparticle porosity affect the thermal efficiency of the retort. The retort height needed to distill the same quality of oil shale served as an indicator of the retort's thermal efficiency. Specifically, a lower required retort height indicated a higher thermal efficiency of the retort. An orthogonal experiment

is a multifactorial experimental research method in which a few representative experimental points can be selected from a large number of experimental combinations. This experimental design enables a substantial reduction in the number of experiments while ensuring the validity of scientific analysis. Range and variance analyses are commonly used to analyze the results of orthogonal experiments. The polar deviation method is simple, fast, and requires minimal calculation, but it also has shortcomings, mainly because it does not separately analyze random or conditional errors; however, the variance method can address this deficiency [27]. In this study, we employed the variance method for data processing and analysis. The detailed calculation method of variance analysis is referenced in [28, 29].

The orthogonal factor-level table used is presented in Table 3. Since the interaction of the factors was not considered, the $L_9(3^4)$ table was selected as the orthogonal table. Nine sets of simulations were required, according to the orthogonal experimental schedule, and each set of simulations was completed sequentially. Table 4 presents the orthogonal table used to study the multifactor effect levels. During the parameter selection process, the experimental parameters were determined based on the actual plant process and theoretical calculations. This was done to ensure several conditions. First, the hot air volume did not exceed 1.24 kg/s. Second, the hot recycle gas temperature was

Table 3. Orthogonal experimental factor level table

Level	Factors		
	Hot air volume, kg/s	Hot recycle gas temperature, °C	Porosity
	A	B	C
1	0.3996	516.07	0.4
2	0.4627	536.07	0.5
3	0.5258	556.07	0.6

Table 4. Orthogonal experimental design and results

Case	Factors				Retort height, m
	A	B	C	Error	
1	1	1	1	1	16.21
2	1	2	2	2	15.15
3	1	3	3	3	14.58
4	2	1	2	3	14.22

Continued on the next page

Table 4. *Continued*

Case	Factors				Retort height, m
	A	B	C	Error	
5	2	2	3	1	13.81
6	2	3	1	2	12.50
7	3	1	3	2	13.24
8	3	2	1	3	12.07
9	3	3	2	1	11.75

close to 550 °C. Additionally, the porosity was optimized using the nonlinear value-taking method in order to identify the optimal parameter combination.

3.2.3. Analysis of orthogonal experiment results

Nine cases were designed in the orthogonal experiment, and the variation diagrams of gas-solid temperature with retort height distribution for each case were analyzed. The distribution law of the maximum retort height is consistent with that in the orthogonal experiment table. The specific variation law of gas-solid temperature distribution with height under each working condition is shown in Figure 6.

It can be observed that regarding the variation of temperature distribution with retort height from Case 1 to Case 9, the overall variation law shows consistency. Among these cases, Case 1 exhibits the highest retort height, which is 16.21 m, while Case 9 is the working condition with the lowest retort height, at 11.75 m. Based on the analysis of retort heights at different levels, the retort height varies with the change of working conditions.

In the lower region of the retort, the gas and solid phase temperatures of all cases rise rapidly to relatively high levels, with peak values approaching or exceeding 750 °C; this is due to the large amount of heat released by the intense combustion reactions occurring in this region. In contrast, in the drying section of the upper retort, the gas and solid phase temperatures decrease continuously and eventually reach relatively low levels. This is because the newly added oil shale particles need to absorb heat from the mixed gas in the retort, resulting in a rapid temperature drop of both phases in this region.

As the retort height increases, the temperatures of the two phases show an overall decreasing trend, but there are significant differences among different cases: the temperature drop in Cases 1–3 is relatively gentle, and the gas phase temperature is consistently higher than the solid phase temperature, with a stable temperature difference between them. This is because the high-temperature gas generated by combustion is used to heat the solid phase,

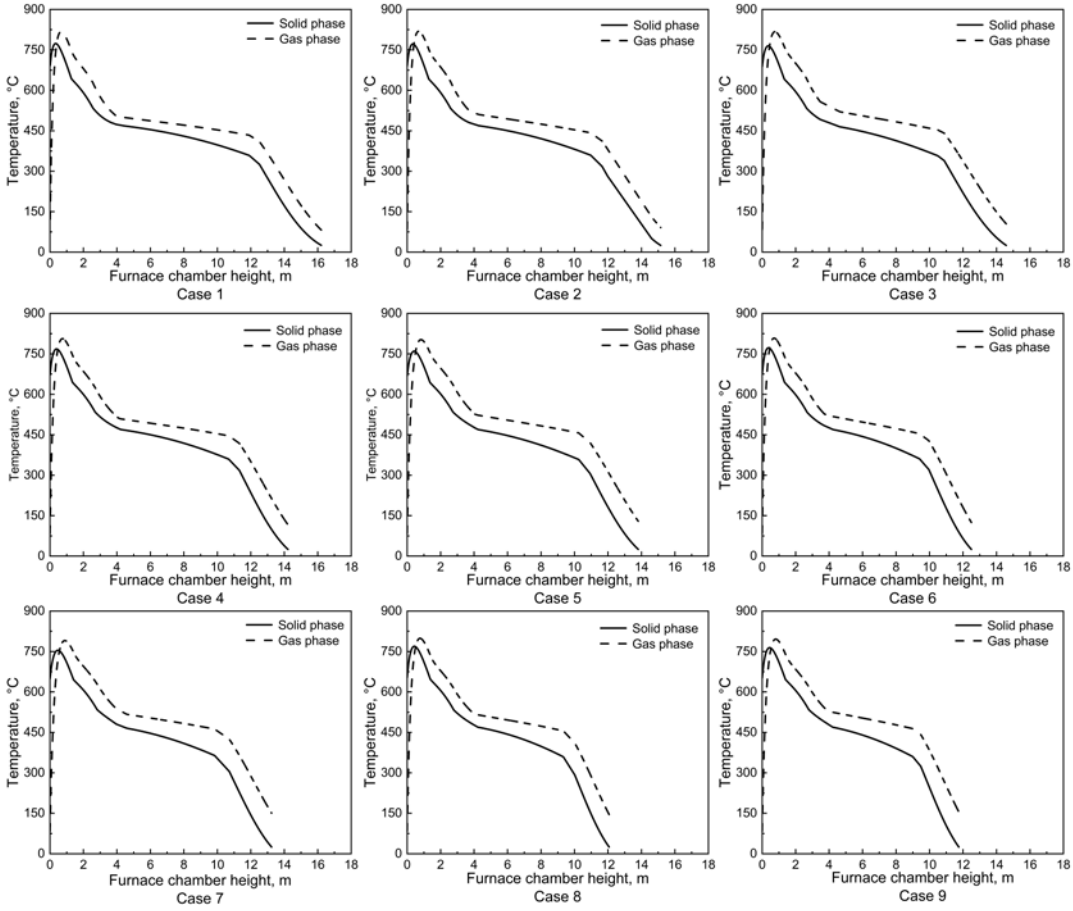

Fig. 6. Gas-solid temperature distribution diagrams for Cases 1–9.

leading to the gas phase temperature remaining continuously higher than the solid phase temperature. The magnitude of the solid phase temperature drop in Cases 4–6 is significantly greater than that in Cases 1–3. The main reason is that the increased hot air volume enhances the heat transfer process with the solid phase, resulting in a larger decrease in the solid phase temperature. The temperature decreasing trend in Cases 7–9 is consistent with the previous cases, but there are differences in specific values and decreasing rates. Along the retort height direction, the temperatures of the gas and solid phases drop more rapidly – especially at the position corresponding to the retorting section, where the length of this section is significantly shortened. This is because, as the hot air volume further increases, the heat supply from the generated gas in the gasification section is enhanced, which facilitates the progress of the retorting reaction.

In general, all cases follow the overall trend of rapid temperature rise to a peak in the lower part of the retort, gradual temperature drop in the middle part, and continuous temperature drop to a relatively low value in the upper part. However, differences exist among cases in terms of temperature change rate, temperature difference between solid and gas phases, and other parameters. These differences are related to factors such as the amount of hot air fed into the retort, the temperature of hot recycle gas, and porosity, which reflect the distribution characteristics of the temperature field in the retort under different working conditions. The height of the retort is affected by changes in different parameters. For example, in Cases 1–9: when the hot recycle gas temperature was consistently 516.07 °C (Cases 1, 4, 7), the retort height decreased from 16.21 m to 13.24 m as the hot air volume increased from 0.3996 kg/s to 0.5258 kg/s; when the hot recycle gas temperature was consistently 536.07 °C (Cases 2, 5, 8), the retort height decreased from 15.15 m to 12.07 m with the increase in the hot air volume; and when the hot recycle gas temperature was consistently 556.07 °C (Cases 3, 6, 9), the retort height decreased from 14.58 m to 11.75 m, following the same trend of hot air flow rate increase. This phenomenon can be attributed to the enhanced heat transfer efficiency inside the retort caused by the increased hot air volume, which promotes the heating of oil shale particles and accelerates the retorting process, thereby leading to a reduction in retort height.

Simulation studies were conducted to analyze how three factors (hot air volume, hot recycle gas temperature, and oil shale interparticle porosity) influence the chamber height of the retort. This analysis aims to rank the factors according to their influence magnitude and uncover the intrinsic relationship between each factor and the key performance indicators of the retorting process. This study employed two statistical methods, range analysis and variance analysis, to investigate the effects of different experimental factors on retort height. Range analysis offers a straightforward way to understand the influence range of each factor, while variance analysis provides a more comprehensive evaluation by considering the variability within the data.

In this study, the orthogonal experimental method was employed to systematically investigate the effects of factors A, B, and C on the retort height standard. The results of range analysis showed that the primary and secondary order of the effects of the three factors on the index was A > B > C, with their range (R) values being 2.96, 1.61, and 0.28, respectively. Analysis of variance further confirmed that both factor A ($F = 75.822$, $P = 0.013$) and factor B ($F = 22.233$, $P = 0.043$) had significant effects on the retort height standard, while the effect of factor C ($F = 0.693$, $P = 0.591$) did not reach the statistical significance level.

The results indicated that factor A was the most critical parameter for controlling the retort height standard, factor B played an auxiliary regulatory role, and factor C had no significant effect on the results within the level range set in the experiment. Taking the reduction of retort height as the optimization

Table 5. Influence of each factor on the mean retort height

Analytical method	Item	Factor			Error
		A	B	C	
Range analysis	K_1	15.31	14.56	13.59	13.92
	K_2	13.51	13.68	13.71	13.63
	K_3	12.35	12.94	13.88	13.62
	R	2.96	1.61	0.28	0.30
Variance analysis	Sum of squares of deviations	13.351	3.915	0.122	0.176
	Freedom	2	2	2	2
	F ratio	75.822	22.233	0.693	
	P	0.013*	0.043*	0.591	
	Significance	*	*	-	

objective, the recommended optimal combination of process parameters was A3 and B3, and the level of factor C could be selected according to actual production conditions. Combining the findings from analytical methods, hot air volume was identified as the key factor affecting the effectiveness of oil shale retorting production [30]. Meanwhile, the effects of hot recycle gas temperature and porosity should not be overlooked.

The mean values of each factor in the orthogonal experiment were plotted for comparative analysis. Figure 7 presents the mean value comparison diagram of the orthogonal experiment, from which it can be observed that factor A (hot air volume), factor B (hot recycle gas), and factor C (porosity) all exert influences on the experimental index. With the increase of factor A (hot air volume), the variation trends of the index under different hot recycle gas temperatures exhibit significant differences: under condition B1, the retort height decreases continuously, from 16.21 to 13.24 m; under condition B2, it remains relatively stable, fluctuating between 15.15 and 12.07 m; under condition B3, it shows fluctuation, yet the overall height also decreases, dropping to a minimum of 11.75 m.

Comprehensive analysis indicates that, to improve the thermal efficiency of the retorting retort, a higher hot air volume should be combined with the hot recycle gas temperature at level B3. This combination can reduce the retort height to 11.75 m, which is the lowest value among all combinations. Meanwhile, the distribution of the three level points of porosity shows that its influence is relatively weak. The results of the orthogonal experiment reveal that hot air volume is the key factor affecting the retort height. Furthermore, range analysis and analysis of variance confirm that the regulation of hot

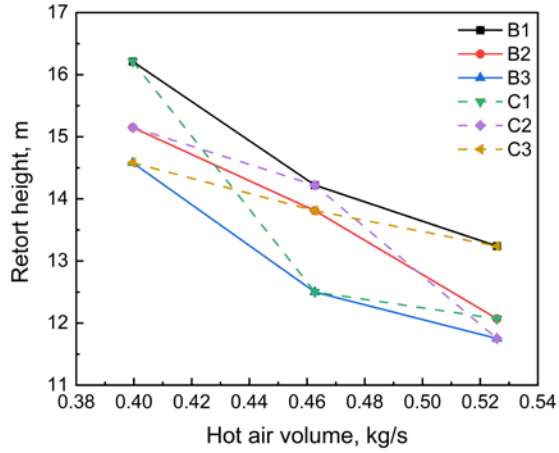

Fig. 7. Mean value comparison diagram of factor A with factors B and C.

air volume is significantly positively correlated with the retorting thermal efficiency – specifically, an increase in the hot air volume can significantly enhance the retorting thermal efficiency.

4. Study on simulation and optimization of hot air parameters for the Fushun-type retort

Based on the above orthogonal experiment results, it is known that the factor with the greatest influence on the height of the retorting retort is the hot air volume. This is a key parameter for regulating the heat supply. An increase in the hot air volume can enhance the kinetic process of the fixed carbon combustion reaction in the gasification section, promote its full combustion, and release more heat, thereby providing sufficient heat support for retorting. Meanwhile, the increase in fixed carbon combustion heat can optimize the distribution of the temperature field in the retort and affect the height of the material layer, the range of the pyrolysis zone, and other factors. To improve the accuracy of simulation results and conduct diversified research, computational fluid dynamics (CFD) software was used to perform simulations on the optimal working condition of the orthogonal experiment.

The water and oxygen in the hot air undergo redox reactions with the fixed carbon (C) in the semi-coke. These reactions mainly occur in the gasification section. The hot air volume has the strongest influence on the gasification section of the retorting retort; therefore, modeling was conducted for the gasification section. All structures used in the simulation adopt the actual parameters of the factory. Model establishment and mesh division were carried out for the gasification section of the retorting retort. The specific modeling area can be seen in Figure 8.

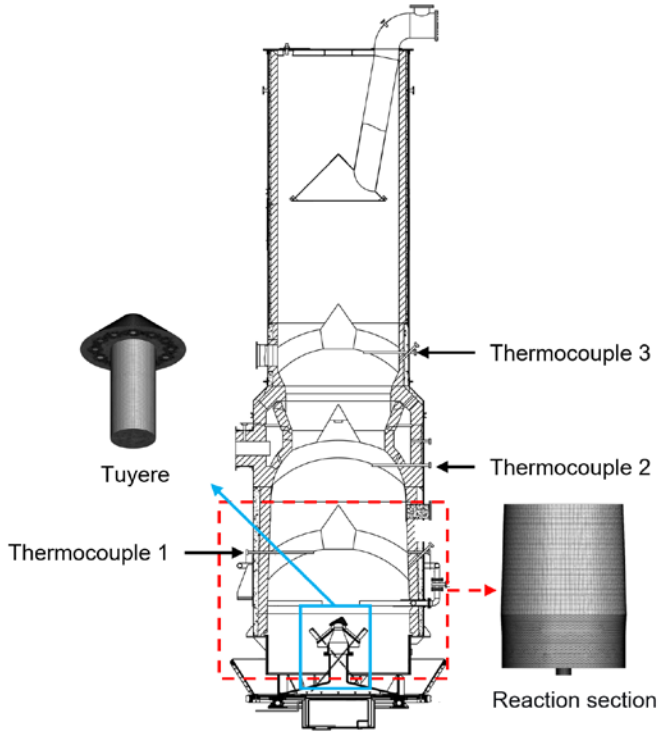

Fig. 8. Schematic diagram of model establishment and mesh division.

Based on the thermocouple position specified in Figure 8, a comparison was conducted between the simulation results and the temperature measurements obtained from the corresponding thermocouples in factory tests. It was found that the error between the CFD simulation data and the measured data is within 5%, which is within a reasonable and acceptable range. This effectively confirms the accuracy of the simulation results.

Figure 9 shows the temperature distribution contour maps of the reaction section under different working conditions. In the gasification section of the retorting retort, heat is mainly derived from the intense oxidation reaction of fixed carbon in semi-coke. In Figure 9(a), the high-temperature zone is mainly distributed in the lower part of the gasification section. Driven by gravity, the fixed carbon (C) in semi-coke falls to the lower part of the gasification section and undergoes an oxidative combustion reaction with oxygen in the introduced hot air, releasing heat. In contrast, in Figure 9(b), the red high-temperature zone is concentrated in the lower-middle part, with the high-temperature zone located relatively higher. This is because the velocity at the hot air inlet is relatively high, resulting in a slow falling speed of semi-coke, and the oxidative combustion reaction occurs in the relatively higher region.

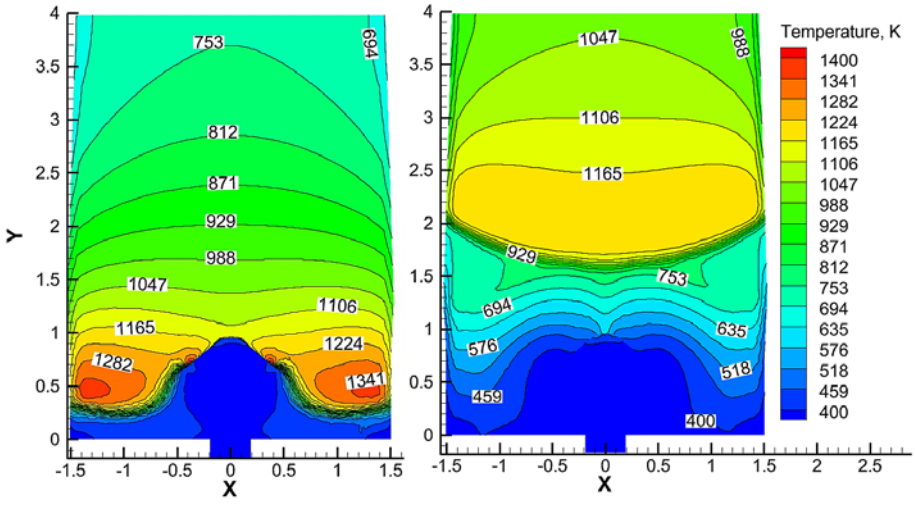

(a) 0.4667 kg/s (b) 0.5258 kg/s

Fig. 9. Temperature distribution contour maps in the gasification section: current factory data with a hot air volume of 0.4667 kg/s (a); the optimal hot air volume of 0.5258 kg/s selected by the orthogonal experiment (b).

The heat released by combustion in the gasification section moves upward along with the high-temperature flue gas, forming an obvious temperature gradient, which presents a gradual temperature decrease from bottom to top. The lower part of the gasification section is a low-temperature zone, mainly because this region is the location of the hot air inlet, where the air velocity is relatively high, driving the airflow upward and preventing the occurrence of combustion reactions in the lower part.

It can be seen in Figure 9 that there are significant differences in the distribution of high-temperature zones under different hot air volumes. This is mainly because increasing the hot air volume leads to an increase in the inlet velocity, which affects the heat transfer behavior and the movement behavior of semi-coke particles in the retort, resulting in the upward shift of the high-temperature zone.

According to the literature, the heat sources required for oil shale retorting are divided into three parts: (1) 47% of the heat is provided by the self-generated gas in the gasification section; (2) 30% of the heat is provided by the hot recycle gas; and (3) 23% of the heat is provided by the heat exchange between the primary air and steam [31]. These three gas streams jointly form a heat carrier, which directly conducts heat exchange with oil shale. By analyzing the above two working conditions, the heat condition at the gas outlet of the gasification section was investigated to explore the contribution degree of the change in the hot air volume in the gasification section to the heat required for the pyrolysis of the oil shale gasification section.

According to the literature, the heat required for retorting 1 kg of oil shale is 989.951 kJ/kg [31]. Based on the CFD simulation results, the contribution of the two working conditions to oil shale retorting was analyzed. The results show that the self-generated gas heating proportion of the orthogonal working condition (59.288%) is higher than that of the current factory working condition (46.554%), as shown in Table 6. These data verify the feasibility of the orthogonal working condition and prove that it has more advantages in improving thermal energy utilization efficiency.

However, analysis based on the position of the temperature distribution contour maps shows that the high-temperature zone under the orthogonal experiment working condition is relatively higher, while under the current factory working condition, the high-temperature zone is mainly distributed in the lower part of the gasification section. A higher-positioned high-temperature zone may lead to a relatively high temperature in the retorting section, potentially causing over-retorting. To stabilize the high-temperature zone at a relatively lower position in the gasification section, reducing the air velocity at the hot air inlet is conducive to maintaining a stable high-temperature zone.

Table 6. Comparison of heat supply quantities

Parameter	Factory working condition	Orthogonal working condition
Mass flow rate at the inlet of the gasification section	0.272 kg/s	0.526 kg/s
Heat flux carried by generated gas per second	460.861 kJ	586.923 kJ
Heat supply proportion of generated gas	46.554%	59.288%
Heat required for retorting 1 kg of oil shale	989.95 1kJ	

Based on an in-depth investigation of thermal parameters, this study establishes that increasing the hot air volume is the most critical pathway for optimizing the retorting process, with its core mechanism being the intensification of the oxidation and exothermic process of fixed carbon in semi-coke. This finding illuminates the path for process innovation: the implementation of oxygen-enriched retorting technology by actively regulating the chemical composition of the inlet gas. By elevating the oxygen concentration in the inlet stream while maintaining an appropriate gas volume, the combustion reaction can be intensified more directly and efficiently, thereby significantly enhancing the self-sustaining heating capacity of the retort. Simulation results indicate that this technology has the potential to increase the heat supply proportion of the process-generated gas beyond 59.288%,

substantially reducing dependence on external heat sources such as circulating carrier gas, and thereby opening a highly promising technological route for energy conservation, consumption reduction, and efficiency enhancement in oil shale retorting processes.

To advance oxygen-enriched retorting technology from concept to industrial practice, future research should concentrate on several key directions. The foremost priority is to systematically explore the effects of different oxygen concentrations (e.g., 25–35%) on retorting thermal equilibrium, product yield, and overall energy consumption, to identify the optimal operational window for oxygen enrichment. Concurrently, it is essential to elucidate the oxidation reaction kinetics of semi-coke under oxygen-enriched conditions and its impact on heat transfer and product formation mechanisms in the upper retorting zones, thereby providing a theoretical foundation for process control. Finally, concerted efforts must be directed toward the system integration and engineering development of this technology, including the creation of coupling schemes with low-energy oxygen production processes, investigation of precise temperature field control strategies in the reaction zone under oxygen-enriched conditions, and comprehensive techno-economic and environmental benefit assessments, ultimately ensuring the safe, stable, and economical operation of this innovative process.

5. Conclusions

Mathematical models for the drying, retorting, reduction, and oxidation sections of the oil shale retort have been developed, yielding a set of energy balance equations for each section. Three typical parameters – hot air volume, circulating hot recycle gas temperature, and oil shale interparticle porosity – were analyzed through single-factor and multi-factor analyses. The aim was to determine the factors most influencing the height of the oil shale retort and to identify the optimal working conditions. Meanwhile, to improve accuracy, CFD simulation technology was used to conduct simulation and comparison between the factory working condition and the optimal working condition selected by the orthogonal experiment.

1. A numerical heat transfer model for each section of the Fushun-type retort has been established and its reliability verified. Subsequently, each section of the retort was optimized using this model. When the retort temperature is 520 °C, the recommended retort height is 13.4 m, with the gasification, retorting, and drying sections being 4.2 m, 6.2 m, and 3.0 m in height, respectively.
2. Orthogonal experimental analysis reveals that the factors influencing retort height, in descending order of significance, are hot air volume, hot recycle gas temperature, and porosity. Hot air volume plays a crucial role in the retorting process.

3. Based on the key finding that increasing the hot air volume optimizes the retorting process by intensifying the oxidation of fixed carbon, this study proposes an innovative strategy of oxygen-enriched retorting. By elevating the oxygen concentration in the inlet gas, this approach is expected to significantly enhance the system's self-sustaining heating capacity, thereby reducing reliance on external heat sources. Subsequent research should focus on determining the optimal oxygen concentration range, elucidating the associated reaction kinetics, and developing the necessary integrated engineering systems to promote the safe and efficient industrial application of this advanced retorting technology.

Data availability statement

All data, models, and code generated or used during this study are included in the article.

Acknowledgments

This study was financially supported by the Scientific Research Project of the Education Department of Liaoning Province (project No. L2020028) and Liaoning Provincial Department of Education unveils local projects (No. JYTMS20231421). We thank the reviewers for their careful reading of the manuscript and for providing valuable guidance and suggestions. The publication costs of this article were partially covered by the Estonian Academy of Sciences.

References

1. Yin, X. H., Cao, Z. B., Cao, C. Y., Lü, N. Simulation and optimization in shale oil condensation recovery system. *Journal of Petrochemical Universities*, 2019, **32**(3), 20–27. https://doi.org/10.3969/j.issn.1006-396X.2019.03.004
2. Wang, Q., Liu, J., Bai, J. R., Kong, L. W. Analysis on properties of shale oil pyrolyzed from oil shale at different heating rates. *Journal of Northeast Electric Power University*, 2011, **31**(1), 24–28.
3. Wang, Q., Xu, C. X., Chi, M. S., Zhang, H. X., Cui, D., Bai, J. R. FT-IR study on composition of oil shale kerogen and its pyrolysis oil generation characteristics. *Journal of Fuel Chemistry and Technology*, 2015, **43**(10), 1158–1166.
4. Nazzal, M. J. Influence of heating rate on the pyrolysis of Jordan oil shale. *Journal of Analytical and Applied Pyrolysis*, 2002, **62**(2), 225–238. https://doi.org/10.1016/S0165-2370(01)00119-X
5. Geng, Y. D., Liang, W. G., Liu, J., Cao, M. T., Kang, Z. Q. Evolution of pore

and fracture structure of oil shale under high temperature and high pressure. *Energy & Fuels*, 2017, **31**(10), 10404–10413. https://doi.org/10.1021/acs.energyfuels.7b01071

6. Pan, C. C., Liang, Q. F., Guo, X. L., Dai, Z. H., Liu, H. F., Gong, X. Characteristics of different sized slag particles from entrained-flow coal gasification. *Energy & Fuels*, 2016, **30**(2), 1487–1495.
7. Xu, L. F., Ma, Z. L., Zheng, L. J., Bao, F. Change of physical properties at different heating rates, time and water content for oil shale. *Petroleum Geology & Experiment*, 2018, **40**(4), 545–550. https://doi.org/10.11781/sysydz201804545
8. Han, X. X., Jiang, X. M., Cui, Z. G. Study of the combustion mechanism of oil shale semicoke in a thermogravimetric analyzer. *Journal of Thermal Analysis and Calorimetry*, 2018, **92**(2), 595–600. https://doi.org/10.1007/s10973-007-8659-6
9. Khalil, A. Oil shale pyrolysis and effect of particle size on the composition of shale oil. *Oil Shale*, 2013, **30**(2), 136–146. https://doi.org/10.3176/oil.2013.2.04
10. Tang, Y. B. A laboratorial study of spontaneous combustion characteristics of the oil shale in Fushun, China. *Combustion Science and Technology*, 2016, **188**(6), 997–1010. https://doi.org/10.1080/00102202.2015.1136301
11. Lu, H., Pan, H. D., Guo, C., Liu, X. Y., Wang, C. H., Yue, Y. Comparative study on pyrolysis kinetic model of Fushun oil shale. *Journal of Liaoning Petrochemical University*, 2020, **40**(1), 20–25. https://doi.org/10.3969/j.issn.1672-6952.2020.01.004
12. Luo, W. X., Yu, C. J., Wang, Q., Zhao, A., Ke, Y. L. Spatially discretised compensation method for coordinate transformation in large-scale metrology under nonuniform temperature field. *Measurement Science and Technology*, 2023, **34**(3), 035003. https://doi.org/10.1088/1361-6501/ACA2D0
13. Baruah, B., Tiwari, P. Effect of high pressure on nonisothermal pyrolysis kinetics of oil shale and product yield. *Energy & Fuels*, 2020, **34**(12), 15855–15869. https://doi.org/10.1021/ACS.ENERGYFUELS.0C02538
14. Rossiello, G., Uzair, M. A., Ahmadpanah, S. B., Rogora, M., Saponaro, A., Torresi, M. Integrated use of CFD and field data for accurate thermal analyses of oil/gas boilers. *Fuel*, 2023, **335**, 126931. https://doi.org/10.1016/j.fuel.2022.126931
15. Zhu, J., Yi, L., Yang, Z., Li, X. Numerical simulation on the in situ upgrading of oil shale reservoir under microwave heating. *Fuel*, 2021, **287**, 119553. https://doi.org/10.1016/j.fuel.2020.119553
16. Brokaw, R. S. Predicting transport properties of dilute gases. *Industrial & Engineering Chemistry Process Design and Development*, 1969, **8**(2), 240–253. https://doi.org/10.1021/i260030a015
17. Al-Harahsheh, M., Kingman, S., Saeid, A., Robinson, J., Dimitrakis, G., Alnawafleh, H. Dielectric properties of Jordanian oil shales. *Fuel Processing Technology*, 2009, **90**(10), 1259–1264. https://doi.org/10.1016/j.fuproc.2009.06.012

18. Jia, C., Li, J., Chen, J., Cui, S., Liu, H., Wang, Q. Simulation and prediction of co-combustion of oil shale retorting solid waste and cornstalk in circulating fluidized bed using CPFD method. *Applied Thermal Engineering*, 2020, **165**, 113574. https://doi.org/10.1016/j.applthermaleng.2019.03.145
19. Xiao, K. M., Wang, Y. M., Hu, H. B., Wen, Z., Lou, G. F., Su, F. Y. et al. Numerical analysis on heat transfer process in the coke oven with the multi-chamber coupling mathematical model. *Case Studies in Thermal Engineering*, 2023, **44**, 102858. https://doi.org/10.1016/J.CSITE.2023.102858
20. Huang, F. F., Liu, W. J., Chen, S. A., Tian, Z. X., Wei, J. T. Thermal desorption characteristics of the adsorbate in activated carbon based on a two-dimensional heat and mass transfer model. *Applied Thermal Engineering*, 2022, **214**, 118775. https://doi.org/10.1016/J.APPLTHERMALENG.2022.118775
21. Achenbach, E. Heat and flow characteristics of packed beds. *Experimental Thermal and Fluid Science*, 1995, **10**(1), 17–27. https://doi.org/10.1016/0894-1777(94)00077-L
22. Wakao, N., Kaguei, S. *Heat and Mass Transfer in Packed Beds*. Gordon and Breach Science Publishers, 1983.
23. Zhao, J. F., Sun, M. G., Zhang, L. X., Hu, C. Z., Tang, D. W., Yang, L. et al. Forced convection heat transfer in porous structure: effect of morphology on pressure drop and heat transfer coefficient. *Journal of Thermal Science*, 2021, **30**, 363–393. https://doi.org/10.1007/s11630-021-1403-x
24. Guo, W., Pan, J., Zhang, X., Deng, S., Zhu, C. Experimental and mechanistic study on isothermal oxidative pyrolysis of oil shale. *Journal of Analytical and Applied Pyrolysis*, 2023, **175,** 106215. https://doi.org/10.1016/J.JAAP.2023.106215
25. Baraj, E., Ciahotný, K., Hlinčík, T. The water gas shift reaction: catalysts and reaction mechanism. *Fuel*, 2021, **288**, 119817. https://doi.org/10.1016/j.fuel.2020.119817
26. Wei, J., Guo, Q., Song, X., Ding, L., Mosqueda, A., Liu, Y. et al. Effect of hydrothermal carbonization temperature on reactivity and synergy of co-gasification of biomass hydrochar and coal. *Applied Thermal Engineering*, 2021, **183**(P2), 116232. https://doi.org/10.1016/j.applthermaleng.2020.116232
27. Seberry, J. *Orthogonal Designs: Hadamard Matrices, Quadratic Forms and Algebras*. Cham, Springer, 2017.
28. Wang, C., Wang, C., Pan, H., Yue, Y. Effect of structure parameters on low nitrogen performance of burner based on orthogonal experiment method. *Case Studies in Thermal Engineering*, 2022, **39**, 102404. https://doi.org/10.1016/j.csite.2022.102404
29. Liu, W. Q. *Design of Experiments*. Tsinghua University Press, Beijing, 2020.
30. Ding, H., Liu, P., Chang, X., Zhang, B. A novel power quality comprehensive estimation model based on multi-factor variance analysis for distribution network with DG. *Processes*, 2023, **11**(8), 2385. https://doi.org/10.3390/pr11082385
31. Wu, Q. C. *Oil Shale Retorting Technology*. Liaoning Science and Technology Press, Shenyang, 2012.

Nomenclature

Symbol	Connotation	Unit
ε	Specific heat capacity of the solid	J kg^{-1} °C^{-1}
ρ	Density	kg/m^3
c_p	Specific heat capacity of the gas at constant pressure	J kg^{-1} °C^{-1}
t_f	Average temperature of the gas	°C
τ	Time	s
v	Velocity	m/s
λ_{feff}	Effective thermal conductivity of the gas	W m^{-1} °C^{-1}
λ_{seff}	Effective thermal conductivity of the solid	W m^{-1} °C^{-1}
$h_{v,s-f}$	Convective heat transfer coefficient per unit area between the gas and the solid phases	W m^{-2} °C^{-1}
t_s	Average temperature of the solids	°C
d_p	Particle diameter	mm
$_f$	Thermal conductivity of the gas	W m^{-1} °C^{-1}
u	Gas flow velocity	m s^{-1}
μ_f	Dynamic viscosity of the gas	Pa·s
$\phi_{go\text{-}in}$	Heat carried into the oxidation section by the gas mixture	W
$\phi_{go\text{-}out}$	Heat carried away from the oxidation section by the gas mixture	W
$\phi_{so\text{-}in}$	Heat carried into the oxidation section by the solids	W
$\phi_{so\text{-}out}$	Heat carried away from the oxidation section by the solids	W
ϕ_y	Heat released by the oxidation reaction in the oxidation sections	W
$m_{go,i-1}$	Mass flow rate of the gas mixture in model section i–1 of the oxidation section	kg s^{-1}
$m_{go,i}$	Mass flow rate of the gas mixture in model section i of the oxidation section	kg s^{-1}
$c_{go,i-1}$	Constant-pressure specific heat capacity of the gas mixture in model section i–1of the oxidation section	J kg^{-1} °C^{-1}
$c_{go,i}$	Constant-pressure specific heat capacity of the gas mixture in model section i of the oxidation section	J kg^{-1} °C^{-1}

Continued on the next page

Continued

Symbol	Connotation	Unit
$c_{so,i+1}$	Constant-pressure specific heat capacity of the solids in model section i+1 of the oxidation section	J kg^{-1} °C^{-1}
$c_{so,i}$	Constant-pressure specific heat capacity of the solids in model section i of the oxidation section	J kg^{-1} °C^{-1}
$t_{go,i-1}$	Average temperature of the gas mixture in model section i–1 of the oxidation section	°C
$t_{go,i}$	Average temperature of the gas mixture in model section i of the oxidation section	°C
$t_{so,i}$	Average temperature of the solids in model section i of the reduction section	°C
$t_{so,i+1}$	Average temperature of the solids in model section i+1 of the reduction section	°C
$h_{o,i}$	Heat transfer coefficient per unit area between the solids and the gas mixture in model section i of the oxidation section	W m^{-2} °C^{-1}
V	Heat transfer volume of the material layer in each model section	m^3
$m_{so,i+1}$	Mass flow rate of the solids in model section i+1 of the oxidation section	kg s^{-1}
$m_{so,i}$	Mass flow rate of the solids in model section i of the oxidation section	kg s^{-1}
$\phi_{gr\text{-}in}$	Heat carried into the reduction section by the gas mixture	W
$\phi_{gr\text{-}out}$	Heat carried away from the reduction section by the gas mixture	W
$\phi_{sr\text{-}in}$	Heat carried into the reduction section by the solids	W
$\phi_{sr\text{-}out}$	Heat carried away from the reduction section by the solids	W
ϕ_h	Heat absorbed by the reduction reaction in the reduction section	W
$m_{gr,j-1}$	Mass flow rate of the gas mixture in model section j–1 of the reduction section	kg s^{-1}
$m_{gr,j}$	Mass flow rate of the gas mixture in model section j of the reduction section	kg s^{-1}
$c_{gr,j-1}$	Constant-pressure specific heat capacity of the gas mixture in model section j–1of the reduction section	J kg^{-1} °C^{-1}
$c_{gr,j}$	Constant-pressure specific heat capacity of the gas mixture in model section j of the reduction section	J kg^{-1} °C^{-1}
$c_{sr,j+1}$	Constant-pressure specific heat capacity of the solids in model section j+1 of the reduction section	J kg^{-1} °C^{-1}

Continued on the next page

Continued

Symbol	Connotation	Unit
$c_{sr,j}$	Constant-pressure specific heat capacity of the solids in model section *j* of the reduction section	J kg^{-1} °C^{-1}
$t_{gr,j-1}$	Average temperature of the gas mixture in model section *j*–1 of the reduction section	°C
$t_{gr,j}$	Average temperature of the gas mixture in model section *j* of the reduction section	°C
$t_{sr,j}$	Average temperature of the solids in model section *j* of the reduction section	°C
$t_{sr,j+1}$	Average temperature of the solids in model section *j*+1 of the reduction section	°C
$h_{r,j}$	Heat transfer coefficient per unit area between the solids and the gas mixture in model section *j* of the reduction section	W m^{-2} °C^{-1}
$m_{sr,j+1}$	Mass flow rate of the solids in model section *j*+1 of the reduction section	kg s^{-1}
$m_{sr,j}$	Mass flow rate of the solids in model section *j* of the reduction section	kg s^{-1}
$\phi_{chc\text{-}in}$	Heat carried into the retorting section by the circulating heat-carrying gas	W
$\phi_{\text{gt-in}}$	Heat carried into the retorting section by the gas mixture	W
$\phi_{\text{gt-out}}$	Heat carried away from the retorting section by the gas mixture	W
$\phi_{\text{st-in}}$	Heat carried into the retorting section by the solids	W
$\phi_{st\text{-}out}$	Heat carried away from the retorting section by the solids	W
ϕ_t	Pyrolysis reaction heat in the retorting section	W
$\phi_{\text{g–t}}$	Heat consumed for retort gas to reach the gas mixture temperature in the retorting section	W
$m_{gt,k-1}$	Mass flow rate of the gas mixture in model section *k*–1 of the retorting section	kg s^{-1}
$m_{gt,k}$	Mass flow rate of the gas mixture in model section *k* of the retorting section	kg s^{-1}
$c_{gt,k-1}$	Constant-pressure specific heat capacity of the gas mixture in model section *k*–1of the retorting section	J kg^{-1} °C^{-1}
$c_{gt,k}$	Constant-pressure specific heat capacity of the gas mixture in model section *k* of the retorting section	J kg^{-1} °C^{-1}
$c_{st,k+1}$	Constant-pressure specific heat capacity of the solids in model section *k*+1 of the retorting section	J kg^{-1} °C^{-1}

Continued on the next page

Continued

Symbol	Connotation	Unit
$c_{st,k}$	Constant-pressure specific heat capacity of the solids in model section *k* of the retorting section	J kg^{-1} °C^{-1}
$t_{gt,k-1}$	Average temperature of the gas mixture in model section *k*–1 of the retorting section	°C
$t_{gt,k}$	Average temperature of the gas mixture in model section *k* of the retorting section	°C
$t_{st,k}$	Average temperature of the solids in model section *k* of the retorting section	°C
$t_{st,k+1}$	Average temperature of the solids in model section *k*+1 of the retorting section	°C
$h_{t,k}$	Heat transfer coefficient per unit area between the solids and the gas mixture in model section *k* of the retorting section	W m^{-2} °C^{-1}
$m_{st,k+1}$	Mass flow rate of the solids in model section *k*+1 of the retorting section	kg s^{-1}
$m_{st,k}$	Mass flow rate of the solids in model section *k* of the retorting section	kg s^{-1}
ϕ_{w}	Latent heat of moisture evaporation in the drying section	W
$\phi_{gd\text{-}in}$	Heat carried into the drying section by the gas mixture	W
$\phi_{gd\text{-}out}$	Heat carried away from the drying section by the gas mixture	W
$\phi_{sd\text{-}in}$	Heat carried into the drying section by the solids	W
$\phi_{sd\text{-}out}$	Heat carried away from the drying section by the solids	W
ϕ_{g-w}	Heat consumption for water vapor to reach the temperature of the mixed gas in the drying section	W
$m_{gd,m-1}$	Mass flow rate of the gas mixture in model section *m*–1 of the drying section	kg s^{-1}
$m_{gd,m}$	Mass flow rate of the gas mixture in model section *m* of the drying section	kg s^{-1}
$c_{gd,m-1}$	Constant-pressure specific heat capacity of the gas mixture in model section *m*–1 of the drying section	J kg^{-1} °C^{-1}
$c_{gd,m}$	Constant-pressure specific heat capacity of the gas mixture in model section *m* of the drying section	J kg^{-1} °C^{-1}
$c_{sd,m+1}$	Constant-pressure specific heat capacity of the solids in model section *m*+1 of the drying section	J kg^{-1} °C^{-1}
$c_{sd,m}$	Constant-pressure specific heat capacity of the solids in model section *m* of the drying section	J kg^{-1} °C^{-1}

Continued on the next page

Continued

Symbol	Connotation	Unit
$t_{gd,m-1}$	Average temperature of the gas mixture in model section m–1 of the drying section	°C
$t_{gd,m}$	Average temperature of the gas mixture in model section m of the drying section	°C
$t_{sd,m}$	Average temperature of the solids in model section m of the drying section	°C
$t_{sd,m+1}$	Average temperature of the solids in model section m+1 of the drying section	°C
$h_{d,m}$	Heat transfer coefficient per unit area between the solids and the gas mixture in model section m of the drying section	W m^{-2} °C^{-1}
$m_{sd,m+1}$	Mass flow rate of the solids in model section m+1 of the retorting section	kg s^{-1}
$m_{sd,m}$	Mass flow rate of the solids in model section m of the retorting section	kg s^{-1}
m_{w}	Mass flow rate of water vapor evaporated from the solids in the drying section	kg s^{-1}
$c_{w,m}$	Constant-pressure specific heat capacity of the water vapor in model section m of the drying section	J kg^{-1} °C^{-1}
$t_{a,m}$	Initial average temperature of the water vapor in model section m of the drying section	°C
$\overline{C}$	Vector comprising heat of the pyrolysis reaction and latent heat of evaporation of water (does not include temperature variables)	
$\vec{t}_1$	Vector comprising average temperatures of oil shale and gas in each modeled section	
$m_{y,all}$	Mass flow rate of gases generated by oxidative combustion in the oxidation section	kg s^{-1}
$m_{h,all}$	Mass flow rate of gases generated by the water-gas reaction in the reduction section	kg s^{-1}
m_{rws}	Mass flow rate of hot recycle gas introduced into the retorting section	kg s^{-1}
$m_{t,all}$	Mass flow rate of retort gas generated in the retorting section	kg s^{-1}
$m_{w,all}$	Mass flow rate of water vapor generated in the drying section	kg s^{-1}

Oil Shale, 2026, 43, 2, 197–227 https://doi.org/10.3176/oil.2026.2.04

Numerical investigation of superheated steam injection for in situ oil shale exploitation: fracture network optimization and energy efficiency analysis

Jianzheng Su[a,b], Dong Yang[c,d], Xudong Huang[c,d]*

[a] State Center for Research and Development of Oil Shale Exploitation, 31 Xueyuan Road, Haidian District, Beijing 100083, China
[b] Sinopec Petroleum Exploration and Production Research Institute, 31 Xueyuan Road, Haidian District, Beijing 100083, China
[c] Key Lab of In situ Property-improving Mining of Ministry of Education, Taiyuan University of Technology, 79 West Yingze Street, Wanbailin District, Taiyuan, Shanxi Province 030024, China
[d] In situ Steam Injection Branch of State Center for Research and Development of Oil Shale Exploitation, Taiyuan University of Technology, 79 West Yingze Street, Wanbailin District, Taiyuan, Shanxi Province 030024, China

Received 18 July 2025, accepted 8 April 2026, available online 16 April 2026

Abstract. *This study numerically investigates in situ oil shale exploitation by superheated steam injection, emphasizing coupled thermo-hydraulic-mechanical processes. An anisotropic multi-field model was developed to evaluate how hydraulic fracture distribution and thermally activated weak planes affect oil/gas recovery and energy return. Using conditions from the Balikun deposit (Xinjiang), four cases were simulated (1–2 hydraulic fractures, with/without weak-plane evolution). Weak-plane activation markedly improves heating via alternating convection and conduction, expanding high-temperature zones and achieving 90.5% oil recovery after 1000 days. Without it, heating is limited (< 60% recovery) and production declines rapidly. Energy return rates peak early (5.79–8.44) but decay without fracture evolution, whereas activated weak planes sustain values > 5 for over a year. Doubling initial fractures boosts recovery by 46% but only slightly improves energy efficiency due to higher steam consumption.*

Keywords: *oil shale, numerical simulation, superheated steam, energy return rate, fracture network.*

* Corresponding author, huangxudong@tyut.edu.cn

1. Introduction

Oil shale, a sedimentary rock rich in immature organic matter, serves as a critical supplementary energy resource to conventional fossil fuels due to its vast global reserves [1, 2]. Under high-temperature conditions, the organic kerogen within oil shale undergoes pyrolysis to produce shale oil and gas. However, conventional mining methods (e.g., underground or open-pit mining) are economically unfeasible for deeply buried oil shale deposits due to low energy density and high extraction costs [3]. Consequently, in situ exploitation has emerged as a promising strategy for mid-to-deep oil shale development. Among existing techniques, the MTI (Mining Technology Institute) method, pioneered by Zhao et al. [4], employs superheated steam as a heat carrier to thermally decompose kerogen while simultaneously transporting pyrolyzed products to the ground. This method involves three key steps: (1) drilling wells in target areas, (2) hydraulic fracturing to establish interconnected fracture networks as initial steam channels, and (3) injecting superheated steam to initiate and sustain pyrolysis.

The in situ steam injection process involves complex thermo-hydro-mechanical-chemical (THMC) coupling effects. Steam injection alters the permeability and mechanical properties of oil shale through thermal expansion, pore pressure changes, and anisotropic deformation [5]. These dynamic interactions, in turn, influence steam flow, heat transfer efficiency, and hydrocarbon recovery rates, ultimately determining the economic viability of the process. While laboratory experiments have provided valuable insights into temperature-dependent properties such as density [6 , 7], permeability [8, 9], and thermal conductivity [9–11], replicating in situ multi-field coupling conditions remains challenging. Field trials, though critical, are cost-prohibitive and lack repeatability, underscoring the need for cost-effective numerical simulations to bridge this gap [13, 14].

Prior studies have focused predominantly on temporal-spatial variations in temperature, seepage, and stress fields during in situ heating. For instance, Kang et al. [14] developed a coupled thermo-hydraulic-mechanical (THM) model to analyze anisotropic heat transfer and deformation in oil shale. Wang et al. [15] further incorporated temperature-dependent anisotropy in thermal conductivity and permeability, revealing how directional heterogeneity affects heating efficiency. Recent advancements include comparative analyses of heating methods (e.g., electromagnetic, microwave, and steam injection) [16–18] and sustainable energy integration [19]. However, existing research largely neglects critical economic metrics such as energy return rate (ERR) and hydrocarbon recovery efficiency, limiting their practical relevance [20–22].

To address this gap, this study integrates temperature-dependent porosity, fracture connectivity, and anisotropic permeability into a THM-coupled numerical model. Using the geological conditions of Xinjiang's Balikun oil shale deposit as a reference, we investigate how hydraulic fracture

configurations and thermally activated weak planes influence hydrocarbon recovery, ERR, and operational longevity. By coupling experimental data with multi-physics simulations, this work provides actionable strategies for optimizing in situ oil shale exploitation, balancing technical performance with economic feasibility.

2. Establishment of THM coupling mathematical model and determination of initial/boundary conditions

2.1. Fundamental assumptions

In situ steam injection for oil shale extraction involves complex physico-chemical processes. To balance computational tractability while preserving the essential physics of in situ thermal recovery, the following simplifying assumptions are adopted:

(1) Continuum medium approximation: The oil shale formation and its overburden/underburden strata are treated as statistically homogeneous continua at the engineering scale. Macroscopic physical-mechanical parameters (e.g., permeability, elastic modulus) are employed directly, with microscale discontinuities (induced by temperature, external loads, or pore pressure) represented implicitly through the statistical evolution of these parameters.

(2) Darcy's law for fluid flow: Fluid motion under local pressure gradients obeys Darcy's law:

$$q = -\frac{k}{\mu}\nabla p, \tag{1}$$

where q is volumetric flux (m/s), k is permeability (m²), μ is dynamic viscosity (Pa·s), and ∇p denotes the hydraulic gradient.

(3) Negligible interfacial tension: Multiphase interfacial tension effects among water, steam, and kerogen pyrolysis products within fractures/pores are disregarded.

(4) Coupled hydrocarbon transport: Pyrolysis-derived hydrocarbons are assumed to migrate advectively with steam/condensate, with their independent transport behavior neglected due to trace concentrations.

(5) Instantaneous kerogen pyrolysis: Organic matter pyrolysis is considered complete upon reaching the threshold temperature, ignoring reaction kinetics and activation energy. This simplification is justified as the measured specific heat capacity of oil shale (which inherently includes kerogen) already incorporates the energy required for pyrolysis across temperature variations.

(6) Transversely isotropic porous media: The oil shale and its mudstone cap/base layers exhibit transverse isotropy in their poroelastic properties.

(7) Local thermal equilibrium: The timescale of heat exchange between pore fluids and the solid matrix is assumed negligible, permitting the use of a local thermal equilibrium equation for conductive–convective heat transfer.

2.2. THM coupling mathematical model

(1) Solid deformation equation

According to Salimzadeh et al. [23], the deformation field of saturated porous media satisfies the following differential equation:

$$\mathrm{div}(\mathbf{D}(\varepsilon-\varepsilon_{\mathrm{c}})-\alpha p\mathbf{I}-\beta_s\boldsymbol{K}(T-T_0)\mathbf{I})+\mathbf{F}=0, \tag{2}$$

where **D** is the stiffness matrix (see Table 1 for the meanings of all symbols used in Equations (2)–(10)). For anisotropic conditions, **D** is expressed as:

$$\mathrm{D}=\begin{bmatrix} C_{11} & C_{12} & C_{13} & 0 & 0 & 0 \\ C_{12} & C_{11} & C_{13} & 0 & 0 & 0 \\ C_{13} & C_{13} & C_{33} & 0 & 0 & 0 \\ 0 & 0 & 0 & C_{44} & 0 & 0 \\ 0 & 0 & 0 & 0 & C_{44} & 0 \\ 0 & 0 & 0 & 0 & 0 & \frac{C_{11}-C_{12}}{2} \end{bmatrix}, \tag{3}$$

where:

$$\begin{cases} C_{11}=E_{par}\left(E_{per}-E\nu_{per}^2\right)\Gamma \\ C_{33}=E_{per}\left(1-\nu_{par}^2\right)\Gamma \\ C_{12}=E_{par}(E_{per}\nu_{par}^2+E_{par}\nu_{per}^2)\Gamma \\ C_{13}=E_{par}E_{per}\nu_{par}\left(1+\nu_{par}\right)\Gamma \\ C_{44}=\mathrm{G}_{per} \\ C_{66}=\mathrm{G}_{par} \\ \Gamma=\frac{1}{(1+\nu_{par})\{(1-\nu_{par})E_{par}-2\nu_{per}^2E_{par}\}} \end{cases} \tag{4}$$

(2) Energy conservation equation

Based on Wang et al. [24], the heat transfer process during in situ thermal recovery of oil shale can be described by the following equations:

$$(\rho c_e)_{\mathrm{eff}}\frac{\partial T}{\partial t}+\rho_l c_{pl}\mathbf{q}\cdot\nabla T-\mathrm{div}(\boldsymbol{\lambda}_{\mathrm{eff}}\nabla T)=0, \tag{5}$$

$$(\rho c_e)=\phi\rho_l c_{pl}+(1-\phi)\rho_s c_{ps}, \tag{6}$$

$$\lambda_{\mathrm{eff}}=(1-\phi)\lambda_{\mathrm{s}}+\phi\lambda_{\mathrm{l}}. \tag{7}$$

The thermal conductivity tensor is given by:

$$\lambda_{\mathrm{s}}=\begin{bmatrix} \lambda_{\mathrm{s-par}} & 0 & 0 \\ 0 & \lambda_{\mathrm{s-par}} & 0 \\ 0 & 0 & \lambda_{\mathrm{s-per}} \end{bmatrix}. \tag{8}$$

(3) Mass conservation equation

According to Salimzadeh et al. [23], fluid flow in porous media satisfies the following mass conservation equation:

$$\mathrm{div}\left(\frac{\mathbf{k}}{\mu_l}(\nabla p + \rho_l g)\right) = \alpha\frac{\partial(\mathrm{div}\mathbf{u})}{\partial t} + C_p\frac{\partial p}{\partial t} - \phi\beta_T\frac{\partial T}{\partial t}. \tag{9}$$

The permeability tensor of oil shale is expressed as follows:

$$\mathbf{k} = \begin{bmatrix} k_{par} & 0 & 0 \\ 0 & k_{par} & 0 \\ 0 & 0 & k_{per} \end{bmatrix}. \tag{10}$$

Table 1. Meanings of symbols

Symbol	Meaning	Symbol	Meaning
D	Stiffness matrix	**I**	Second-order identity tensor
α	Biot coefficient	p	Fluid pressure
β_s	Thermal expansion coefficient of oil shale	T_0	Initial temperature of the domain
$\boldsymbol{K}$	Bulk modulus of oil shale matrix	$\boldsymbol{F}$	Body force component matrix
$\boldsymbol{E}_{par}$	Elastic modulus parallel to bedding plane	$\boldsymbol{E}_{per}$	Elastic modulus perpendicular to bedding plane
$\boldsymbol{v}_{par}$	Poisson's ratio parallel to bedding plane	$\boldsymbol{v}_{per}$	Poisson's ratio perpendicular to bedding plane
$\boldsymbol{\rho}_l$	Density of heated fluid	C_{pl}	Specific heat capacity of heated fluid
q	Velocity of heated fluid	$\boldsymbol{T}$	Temperature
$\boldsymbol{\rho}_s$	Density of oil shale	C_{ps}	Specific heat capacity of heated oil shale
$\boldsymbol{\lambda}_s$	Thermal conductivity tensor of oil shale	$\boldsymbol{\lambda}_l$	Thermal conductivity tensor of heated fluid
$\boldsymbol{\lambda}_{s-par}$	Thermal conductivity of oil shale parallel to bedding plane	$\boldsymbol{\lambda}_{s-per}$	Thermal conductivity of oil shale perpendicular to bedding plane
k	Permeability tensor of oil shale	μ_l	Dynamic viscosity of heated fluid
u	Deformation of oil shale	g	Gravitational acceleration
ϕ	Porosity of oil shale	$\boldsymbol{C}_p$	Compressibility coefficient of heated fluid

Continued on the next page

Table 1. *Continued*

Symbol	Meaning	Symbol	Meaning
β_T	Volumetric expansion coefficient of heated fluid	$\boldsymbol{k}_{par}$	Permeability of oil shale parallel to sedimentary bedding plane
$\boldsymbol{k}_{per}$	Permeability of oil shale perpendicular to sedimentary bedding plane	C_e	Equivalent specific heat capacity

As demonstrated by Wang et al. [25], oil shale exhibits significant permeability anisotropy. The permeability of oil shale in different directions under varying temperature conditions can be obtained through the following fitting equations:

$$k_{\mathrm{per}} = \begin{cases} 0 & (20 < T < 450\ ℃) \\ 2.46 \times 10^{-20}T + 1.081 \times 10^{-17} & (450 \le T < 550\ ℃) \\ -2.457 \times 10^{-21}T^2 + 2.805 \times 10^{-18}T + 7.868 \times 10^{-16} & (550 \le T \le 600\ ℃) \end{cases}, \quad (11)$$

$$k_{\mathrm{par}} = \begin{cases} -4.539 \times 10^{-22}T^2 + 2.036 \times 10^{-19}T - 5.419 \times 10^{-18} & (20 \le T < 350\ ℃) \\ 1.759 \times 10^{-20}T^2 - 1.212 \times 10^{-17}T + 2 \times 10^{-15} & (350 \le T \le 600\ ℃) \end{cases}. \quad (12)$$

The coupled THM mechanism of in situ thermal recovery of oil shale involves significant interactions among physical parameters. Based on extensive previous research, this study summarizes the theoretical and empirical formulas for key physical parameters in in situ thermal recovery of oil shale as functions of temperature, pore pressure, and time, as presented below:

$$\begin{cases} \rho_{\mathrm{g}} = 2272.7\frac{p \times 10^{-6}}{T+273} \\ \rho_{\mathrm{w}} = (0.9967 - 4.615 \times 10^{-5}T - 3.063 \times 10^{-6}T^2) \times 10^3 \\ \mu_{\mathrm{g}} = (0.36T + 88.37) \times 10^{-7} \\ \mu_{\mathrm{w}} = \left(\frac{1743-1.8T}{47.7T+759}\right) \times 10^{-3} \\ C_{\mathrm{g}} = -0.0001T^3 + 0.0948T^2 - 27.103T + 9246.8 \\ C_{\mathrm{w}} = 0.0165T^2 - 1.4878T + 4207.4 \\ \lambda_{\mathrm{g}} = 1.0 \times 10^{-8}T^3 - 4.0 \times 10^{-6}T^2 + 0.0006T + 0.0078 \\ \lambda_{\mathrm{w}} = -1.26 \times 10^{-5}T^2 + 2.56 \times 10^{-3}T + 0.5513 \\ \rho_{\mathrm{s}} = -8.0 \times 10^{-9}T^3 - 9.0 \times 10^{-6}T^2 + 0.0018T + 2.0919 \\ \phi = -5.0 \times 10^{-7}T^3 + 0.0005T^2 - 0.1028T + 7.2611 \\ \lambda_{s-per} = 1.176 \times 10^{-6}T^2 - 0.00285T + 1.9381 \\ \lambda_{s-par} = 4.563 \times 10^{-6}T^2 - 0.00119T + 0.7581 \end{cases}. \quad (13)$$

The aforementioned permeability fitting equations were derived from intact oil shale specimens and do not account for the enhanced heating effect caused by thermally induced fractures along bedding planes during steam injection. However, thermal fracturing in oil shale under steam stimulation primarily occurs along bedding planes, thereby improving permeability only in the parallel direction. Therefore, in this numerical simulation, the permeability perpendicular to bedding planes adopts the results from Wang et al. [25], while the permeability parallel to bedding planes is modified based on previous studies [26], as detailed below.

The permeability of oil shale parallel to bedding planes is primarily influenced by the density and aperture of interconnected fractures. At room temperature, oil shale is highly compact and intact, exhibiting extremely low permeability. However, at the meter scale, pre-existing fractures may exist due to diagenetic and geological processes, providing initial pathways for high-temperature steam during the early heating stage. Thus, it is assumed that the initial hydraulic fractures, propped by supporting agents, maintain high permeability (on the order of 10^{-12} to 10^{-1} m^2). The solid matrix is assumed to remain fracture-free below 350 °C, with its permeability determined by Wang et al. [25]. For newly formed interconnected fractures above 350 °C, permeability data from reference [27] are adopted. All permeability data are imported into the COMSOL Multiphysics software in the form of interpolation functions, as illustrated in Figure 1.

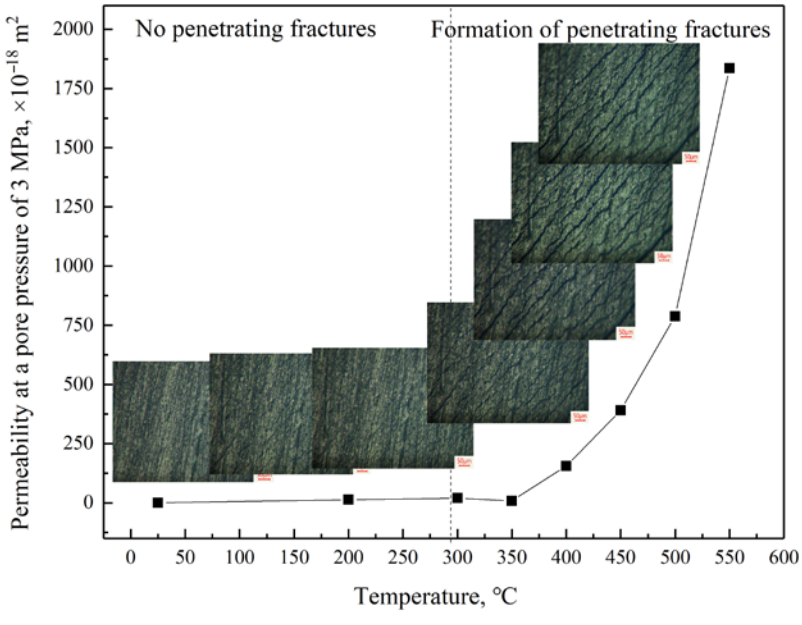

Fig. 1. Variation curve of oil shale permeability with temperature considering fracture evolution [27].

2.3. Establishment of the physical-geometric model

This study is primarily based on the occurrence conditions of oil shale in Barkol, Xinjiang, as the engineering background. Therefore, the physical-geometric model for numerical simulation is established according to the burial conditions of oil shale in Barkol. The average total thickness of the oil shale in Barkol is approximately 42.58 m, comprising about 22 oil shale layers with an average oil yield of 6.52%, while locally, the oil yield can exceed 10%. The burial depth of oil shale in this mining area ranges from the surface to 500 m underground, and the shallowly buried oil shale resources are currently being exploited via open-pit mining. The oil shale layers in this region exhibit a gentle occurrence, with a dip angle generally around 3°, though locally reaching up to 60°. The roof and floor strata of the oil shale layers are predominantly silty mudstone or mudstone, which are weakly aquiferous and act as aquicludes. The arid climate, absence of perennial surface water, and simple hydrogeological conditions in the mining area are favorable for the industrial practice of in situ steam injection for oil shale exploitation.

Based on the above considerations, the physical-geometric model for numerical simulation is simplified as follows:

(1) The dip angle of the oil shale layer is assumed to be 0°, i.e., a horizontal stratum.

(2) The depth from the surface to the top of the oil shale layer is 200 m, with a layer thickness of 40 m.

(3) The roof and floor strata are weakly aquiferous aquicludes with extremely low permeability, and no aquifers are present above or below the oil shale layer.

(4) A nine-well arrangement is adopted for the exploitation zone, consisting of one central steam injection well surrounded by eight production wells, as illustrated in Figure 2. The spacing between adjacent wells is 60 m. For numerical simulation, only a quarter of the model is considered, containing one injection well and three production wells located at the vertices of the model.

Research by Wang et al. [15] indicates that during in situ steam injection for oil shale exploitation, a fracture spacing of 20 m in the oil shale reservoir yields optimal heating efficiency and economic benefits. Given the assumed oil shale layer thickness of 40 m in this study, only cases with one and two hydraulic fractures are considered. For a single fracture, it is located at the mid-height of the oil shale layer. For two fractures, the upper fracture is 10 m below the roof, and the lower fracture is 10 m above the floor, with a vertical spacing of 20 m between them, both aligned along the bedding plane.

Furthermore, according to the findings in [27], when high-temperature steam is injected to heat oil shale, under a steam injection-to-production well spacing of 25 cm, the spacing of thermally induced fractures connecting the injection and production wells along the bedding plane is approximately 1 cm. Thus, it is assumed that the ratio of fracture spacing to well spacing under steam heating conditions is 1:25. Consequently, for a well spacing of 60 m,

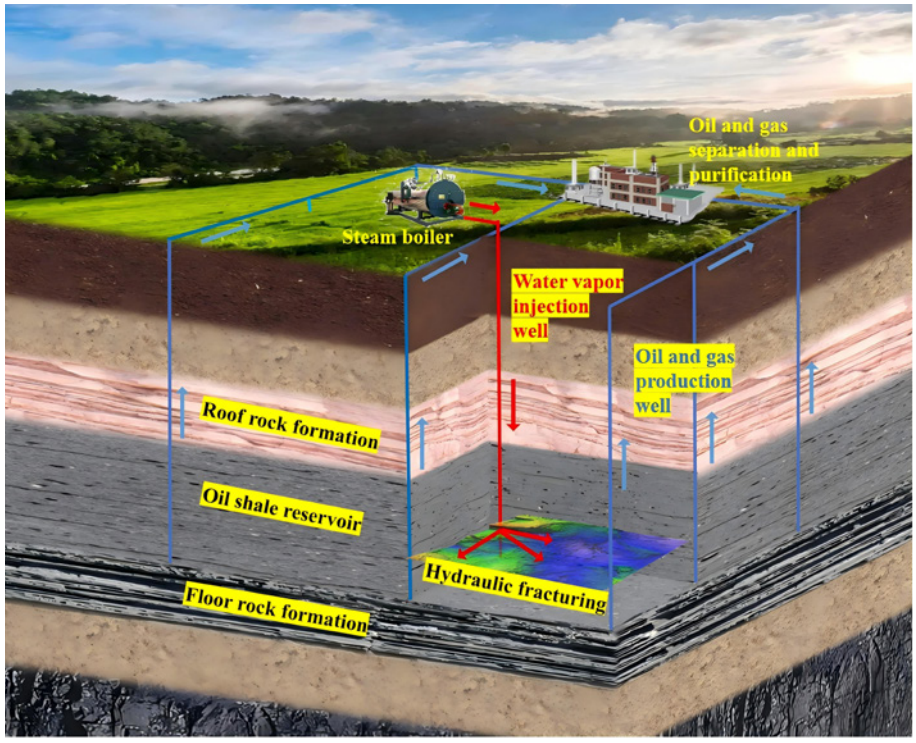

Fig. 2. Nine-well arrangement system for the in situ pyrolysis process of oil shale [27].

the spacing of thermally induced fractures should be 2.4 m. Therefore, this study assumes that weak planes are distributed every 2.5 m along the bedding plane in the oil shale layer. These weak planes remain closed at low temperatures (below 350 °C), exhibiting the same permeability as the solid matrix. When the temperature exceeds 350 °C, these weak planes evolve into interconnected fractures along the bedding plane. Once fractures form, they create new steam channels, allowing high-temperature steam to penetrate and further expand the heated zone. For comparison, cases without weak planes in the oil shale layer are also investigated. Table 2 summarizes the fracture and weak plane distributions for the four models studied.

The assumptions regarding weak plane spacing and extension distance in this study are extrapolated linearly from the results of [28]. The rationale for these assumptions is briefly explained as follows. Figure 3 shows oil shale core samples obtained via drilling in the Barkol oil shale mining area. Core analysis reveals abundant fractures and weak planes within the oil shale layers, with some intervals even containing large fracture zones. These fractures or weak planes are often associated with iron oxides, resulting in lower cementation strength. The cores obtained from drilling tend to break along these fractures or weak planes, which exhibit a wide range of scales, from micrometers to

meters. Figure 4 schematically illustrates the relationship between temperature field distribution and fracture development under steam heating. Initially, steam flows only along the initial fractures, heating the surrounding rock. Thermal fracturing of the heated rock generates new steam channels, further expanding the heating range. Thus, the assumptions regarding weak plane and fracture evolution in this study are reasonable.

It is important to note that the 2.5 m spacing is a conceptual model parameter derived from a linear extrapolation of laboratory-scale findings (1 cm fracture spacing under 25 cm well spacing [28]) to the field-scale well spacing of 60 m. While this provides a computationally tractable and mechanistically plausible representation of fracture network evolution, we acknowledge its inherent limitations. The actual spacing of natural weak planes and thermally induced fractures in a real reservoir is likely heterogeneous and influenced by in situ stress fields and geological discontinuities that are not fully captured in this model. Consequently, the absolute values of recovery and energy efficiency may be sensitive to variations in this assumed spacing. However, the primary conclusion of this study – that the activation of weak planes significantly enhances heating efficiency and recovery compared to models without them – is expected to hold qualitatively. Future work should include a systematic sensitivity analysis on this parameter once more field data becomes available to better constrain its range.

Table 2. Fracture distribution and weak surface distribution of different models

Model No.	Number of hydraulic fractures	Consideration of weak planes in the oil shale layer	Remarks
Model 1	1	No	The hydraulic fracture is located at the mid-depth of the oil shale layer, aligned along the bedding plane and connecting the injection and production wells.
Model 2	1	Yes	The hydraulic fracture is positioned at the mid-depth of the oil shale layer, following the bedding plane orientation and linking the injection and production wells. Weak planes are distributed every 2.5 m along the sedimentary bedding plane; these planes evolve into interconnected fractures between wells when the formation temperature exceeds 300 °C.
Model 3	2	No	The upper hydraulic fracture is 10 m below the roof of the oil shale layer, while the lower fracture is 10 m above the floor. These two fractures are spaced 20 m apart and both follow the bedding plane to connect the injection and production wells.
Model 4	2	Yes	The upper hydraulic fracture is 10 m below the roof, and the lower fracture is 10 m above the floor, with 20 m vertical spacing. Both fractures are bedding-aligned and connect the wells. Weak planes (spaced 2.5 m along bedding) thermally evolve into conductive fractures at temperatures > 300 °C.

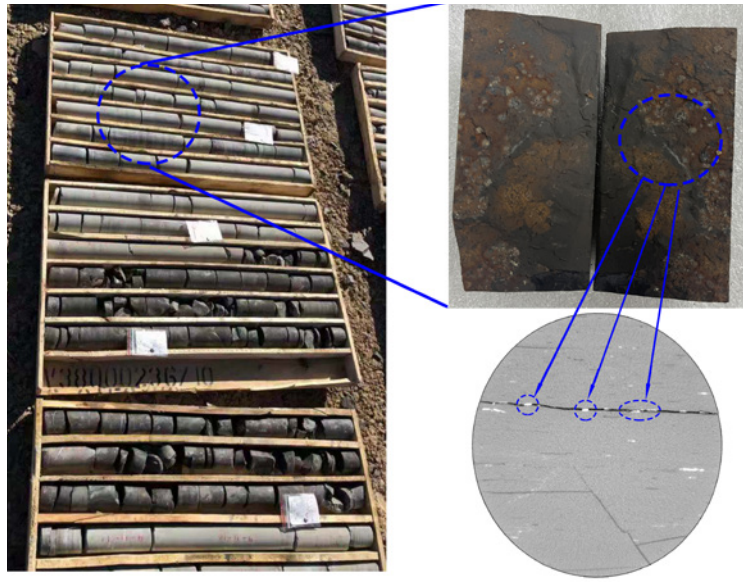

Fig. 3. Oil shale samples obtained by drilling.

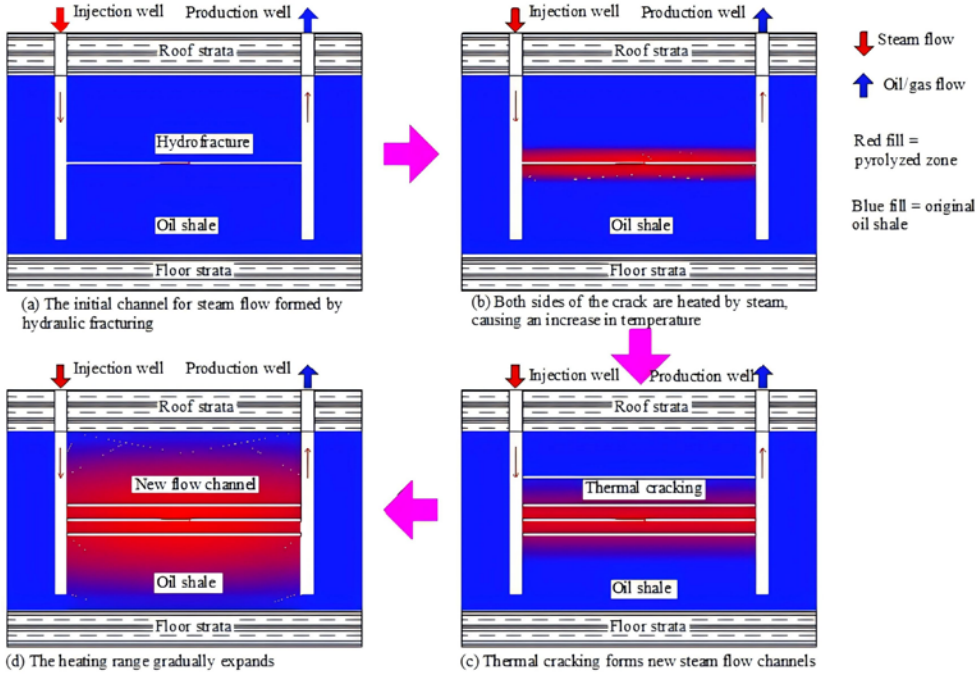

Fig. 4. Convection–conduction compound efficient heating mode for in situ exploitation of oil shale by superheated steam injection.

2.4. Determination of initial and boundary conditions for numerical simulation

Temperature field initial and boundary conditions: For numerical calculations in this study, the initial formation temperature is assumed to be 25 °C, while the temperature at the oil shale layer position in the injection well is set at 600 °C. The wellbore insulation is assumed to be effective, making all other boundaries free boundary conditions.

Solid deformation field initial and boundary conditions: The physical model's upper boundary is located 200 m below the surface. Therefore, a stress boundary condition of 5 MPa is applied to the top surface in the downward direction. The bottom (z = 0), left (y = 0), and back (x = 0) boundaries are fixed displacement boundaries with W = 0, V = 0, and U = 0, respectively, where U, V, and W represent displacements in the x, y, and z directions. Stress boundary conditions of 6 + γz MPa are applied to the surfaces where x and y equal 50 m, with directions as shown in Figure 5.

Seepage field initial and boundary conditions: The initial pore pressure in both the oil shale reservoir and cap rocks is assumed to be 0.1 MPa. The injection pressure at the oil shale layer section of the injection well is 3 MPa, while the production well pressure in the same section is 0.1 MPa.

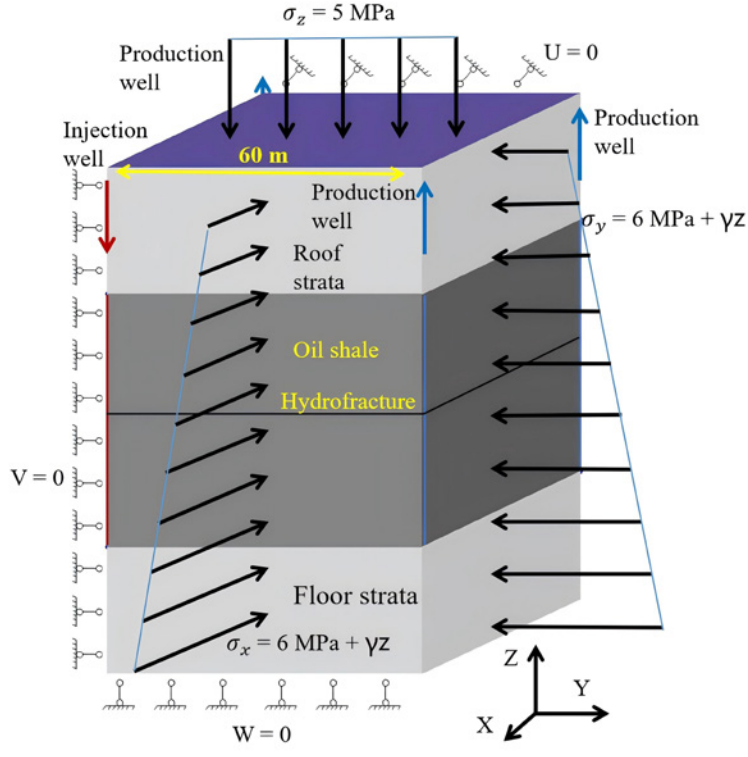

Fig. 5. Boundary conditions of numerical simulation (based on Model 1).

The wellbores are assumed to have excellent cementing conditions except in the oil shale layer section, meaning the internal fluid pressure has no effect on the surrounding rock's pore pressure.

Boundary conditions on symmetry planes: The numerical model utilizes a quarter-symmetry domain to simulate the full nine-well pattern, as shown in Figure 5. To accurately represent the symmetry of the full system, specific boundary conditions are applied to the symmetry planes (the planes at x = 0 and y = 0):

- Solid deformation field: These planes are defined as roller boundaries. This is implemented by constraining the normal displacement to zero; specifically, the displacement component U is set to zero on the symmetry plane at x = 0, and the displacement component V is set to zero on the symmetry plane at y = 0. This prevents motion across the symmetry planes while allowing for tangential deformation.
- Seepage field: The same symmetry planes are treated as impermeable (no-flux) boundaries. This condition ensures that no fluid flow occurs across these planes, which is physically consistent with the symmetry of the full well pattern, where these planes represent lines of symmetry in the flow field.

2.5. Calculation methods for recovery rate and energy return rate

According to the literature [29], the residual organic matter content in oil shale after heating by high-temperature steam at different temperatures shows good consistency with the thermogravimetric (TG) curve. Specifically, the residual organic matter content decreases with increasing temperature, and the temperature range of rapid organic matter reduction corresponds to the rapid mass loss range observed in TG experiments. CT observations reveal minimal residual organic matter above 550 °C, with no significant further reduction at higher temperatures. TG experiments also show markedly slower mass loss rates above 550 °C. Therefore, this study assumes that all mass loss in TG experiments represents conversion to oil/gas products, and temperatures above 550 °C indicate complete pyrolysis with 100% resource recovery. Based on these assumptions, the recovery rate (R_p) is calculated as follows:

$$R_P = \frac{\iiint_\Omega (1-\eta(T))\,\mathrm{d}\Omega}{\iiint_\Omega (1-\eta(550))\,\mathrm{d}\Omega}, \tag{14}$$

where $\eta(T)$ represents the oil shale TG curve. The mass loss is equated to oil/gas product mass, excluding effects from moisture evaporation. To minimize calculation errors, TG data from literature [29] are directly imported into COMSOL Multiphysics as interpolation functions (Fig. 6).

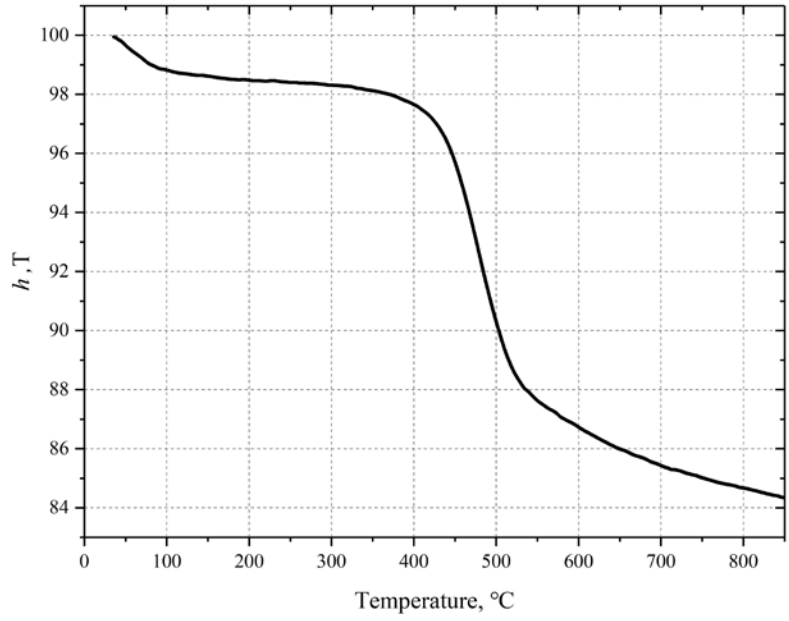

Fig. 6. Thermogravimetric curve of oil shale.

It is crucial to clarify the spatial context of the recovery calculation. The volume integrals in Equation (14) are computed over the entire quarter-symmetry numerical domain (Ω) established in Section 2.3 and illustrated in Figure 5. This domain contains one injection well and three production wells at its vertices, representing a symmetrical quarter of the full nine-well pattern. The recovery factor R_P thus calculated (e.g., the reported 90.5% for Model 4) represents the recovery efficiency achieved within this quarter-domain. The symmetric boundary conditions (zero normal displacement and zero fluid flux) applied at the symmetry planes (x = 0 and y = 0) ensure that the thermo-hydraulic-mechanical processes within this quarter-domain are representative of the processes occurring in the entire multi-well system. Therefore, the recovery factor from the quarter-domain is directly applicable to and representative of the performance of the full well pattern.

Previous numerical studies on in situ oil shale development primarily focused on the spatiotemporal evolution of temperature, seepage, and deformation fields, with some examining production characteristics. However, such limited focus provides inadequate guidance for industrial practice, which must consider economic viability. Without economic analysis, production-focused conclusions can be misleading. For energy development, the ERR serves as an effective economic indicator. This study therefore proposes key technical parameters based on R_E analysis.

The ERR is calculated as follows:

$$ERR = \frac{\text{Thermal energy of oil/gas products}}{\text{Injected thermal energy}}, \tag{15}$$

where the calorific value (E_p) of oil and gas products is calculated as 40 MJ/kg. This value is adopted as a representative weighted-average calorific value for the mixture of shale oil and pyrolysis gas generated from oil shale. The injected energy considers only the thermal energy carried by steam entering the oil shale layer through perforated pipes, excluding surface boiler and pipeline losses. The detailed formula is the following:

$$ERR = \frac{E_p \rho_s \iiint_{\Omega} (1-\eta(T))\mathrm{d}\Omega}{\int_0^t Q_g \rho_l(T) C_l(T)\mathrm{d}t}, \tag{16}$$

where Q_g is the steam injection rate (m^3/s), $\rho_l(T)$ is the high-temperature fluid density (kg/m^3) at temperature T, and $C_l(T)$ is the specific heat capacity ($J/(kg \cdot °C)$) of steam at temperature T.

3. Findings and discussion

3.1. Distribution and evolution of the reservoir temperature field during in situ steam injection for oil shale extraction

During in situ steam injection for oil shale extraction, the spatiotemporal distribution characteristics of temperature directly influence key parameters and technical indicators such as the permeability of the oil shale formation, oil recovery rate, and energy return rate. Table 3 presents the temperature field distribution of the oil shale formation for different models at various heating durations.

As shown in Table 3, during the initial heating stage, due to the extremely low permeability of the oil shale formation, a cylindrical high-temperature zone forms only near the steam injection well. Simultaneously, high-temperature steam flows through the initial fracture channels created by hydraulic fracturing, entering the interior of the oil shale formation and migrating toward the production well, forming a flattened high-temperature zone along the fracture paths. At one month of heating, the temperature field distributions of Models 1 and 2 are identical, while those of Models 3 and 4 are also nearly identical. This is because, in the early heating stage, high-temperature steam can only flow toward the production well through the initial hydraulic fractures. The surrounding rock adjacent to the fractures remains at a relatively low temperature, which is insufficient to induce the opening of weak planes in the oil shale formation to form interconnected steam channels between the injection and production wells.

As heating progresses, significant differences in temperature field distribution emerge among the models. Models 1 and 3 do not account for

the evolution of weak planes in the formation. Consequently, with prolonged heating, the high-temperature zone around the steam injection section expands annularly along the bedding planes of the oil shale, while the surrounding rock near the fractures continues to heat up via conduction. However, the expansion distance of the high-temperature zone remains limited due to the low thermal conductivity of oil shale, which hinders efficient large-scale heating through conduction alone. A comparison between Models 1 and 3 reveals that increasing the number of hydraulic fractures enhances heating efficiency, even without considering the influence of weak planes.

Table 3. Temperature distribution at different heating times

Time	Model 1	Model 2	Model 3	Model 4
30 d	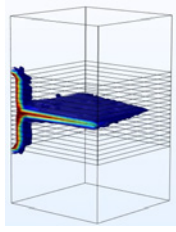	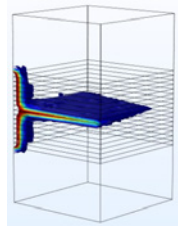	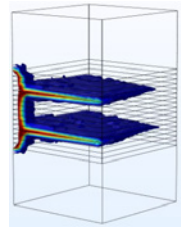	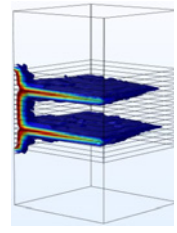
365 d	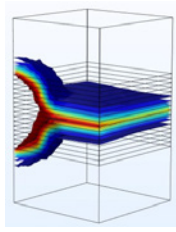	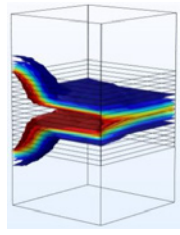	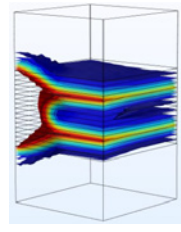	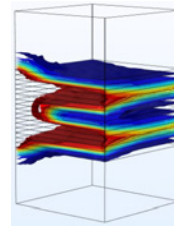
730 d	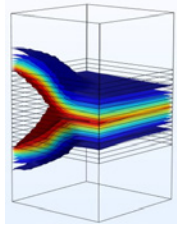	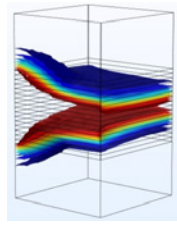	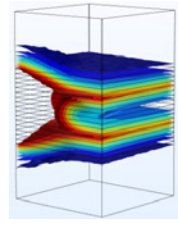	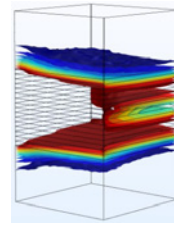
1000 d	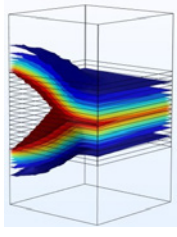	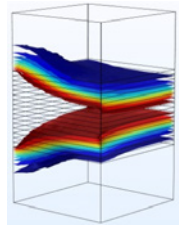	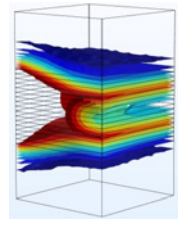	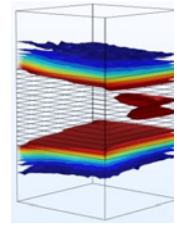

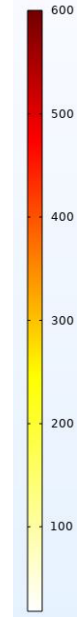

In contrast, Models 2 and 4 incorporate the influence of weak planes evolving into interconnected fractures on steam flow, resulting in fundamentally different temperature field distributions compared to Models 1 and 3. Under this condition, while high-temperature steam flows through the initial hydraulic fractures, the surrounding rock adjacent to the fractures is also heated. As the temperature of the surrounding rock rises and exceeds the thermal cracking threshold of oil shale (above 350 °C), fractures preferentially initiate along weak planes, forming bedding-parallel fractures. Once these newly formed fractures fully connect the injection and production wells, high-temperature steam enters the oil shale formation through these new pathways. At this stage, the heating mechanism transitions from conductive heating to convective steam heating along the newly formed fractures. Since convective heating is significantly faster than conduction, the temperature of the oil shale near the new fractures rises rapidly. Consequently, the flattened high-temperature zone expands perpendicular to the bedding planes. This alternating convection–conduction heating process facilitates rapid heating of the oil shale formation. A comparison between Models 2 and 4 demonstrates that increasing the number of hydraulic fractures accelerates heating.

Wang et al. [24] proposed constructing two 0.5 m-thick hydraulic fracture zones in the oil shale formation to serve as initial pathways for high-temperature steam. These zones exhibit high permeability, allowing steam to rapidly establish high-temperature regions and conductively heat the adjacent rock above and below. Simultaneously, as the temperature of the oil shale formation increases due to steam heating, the permeability of non-fractured regions improves, enabling steam to penetrate further and enhance heating. While this method achieves effective heating, creating thick fracture zones via hydraulic fracturing is challenging in practice. Unlike Wang's model, the proposed Models 3 and 4 feature two discrete fractures rather than thick zones, better reflecting real-world engineering conditions. Moreover, when accounting for weak plane evolution (Model 4), heating efficiency and oil recovery rates comparable to Wang's model can be achieved.

Figure 7 illustrates the temperature distribution in the oil shale formation at the production well (located 60 m from the injection well) under different heating durations. The results demonstrate significant variations in heating efficiency among the models despite identical well configurations, injection temperatures, and gas pressures.

Model 1 assumes only a single hydraulic fracture and no thermally activated weak planes that could evolve into interconnected fractures linking the injection and production wells. As shown in Figure 7(a), even after 2.5 years of heating, temperatures exceeding 600 °C were confined to the immediate vicinity of the hydraulic fracture. The surrounding rock exhibited a rapid thermal decline, dropping below 100 °C within 10 m of the fracture.

Model 2 incorporates the influence of weak planes evolving into permeable fracture networks. Figure 7(b) reveals that thermally activated weak planes significantly enhance heating efficiency, enabling a broad region of the oil

shale formation to reach pyrolysis temperatures. After 2.5 years, a 16-m-long high-temperature zone (> 500 °C) centered on the hydraulic fracture developed at the production well.

Model 3 disregards weak plane evolution but includes an additional hydraulic fracture. A comparison between Figure 7(a) and (c) indicates that dual fractures markedly expand the heated area. Initially, steam heats the rock adjacent to each fracture, with the inter-fracture zone gradually warming over time. By 2.5 years, the midpoint between the fractures reached 222 °C.

Model 4 combines dual fractures with weak plane activation. Figure 7(d) shows that early-stage heating was initially restricted to the fracture vicinity (258 °C at one month). However, after six months, the high-temperature zone expanded vertically, and by two years, the inter-fracture region homogenized at ~600 °C.

Notably, the transition from high-temperature (> 500 °C) to low-temperature (< 100 °C) zones remained within 20 m throughout the heating process. This phenomenon arises from the strong temperature dependence of oil shale permeability – high-temperature regions exhibit permeabilities 3–4 orders of magnitude greater than those of low-temperature zones. The resulting preferential steam flow into high-permeability areas further amplifies the thermal contrast. Low-permeability zones rely solely on conductive heating, which is inefficient due to oil shale's low thermal conductivity. This sharp thermal gradient forms a natural "thermal barrier" [30], minimizing heat loss and improving energy efficiency.

The "thermal barrier" is not a physical structure but a dynamic thermo-hydraulic phenomenon that arises from the coupling between localized convective heating within the fracture network and slow conductive heating of the intact oil shale matrix. Its formation can be attributed to three primary factors: (1) the inherently low thermal conductivity of oil shale, which restricts conductive heat spread; (2) the channelized flow of superheated steam, which creates a high-temperature zone bounded by the connected fracture pathways between injection and production wells; and (3) the sharp permeability contrast between this inner, fractured zone and the outer, intact rock mass, which prevents steam from penetrating beyond the active flow region. Consequently, the periphery of the heated zone relies solely on slow thermal conduction, resulting in a steep temperature decline that acts as an insulating layer. This mechanism is crucial for long-term energy efficiency, as it confines the injected thermal energy to the target production volume, thereby reducing parasitic heat loss to the surrounding formation and significantly enhancing the overall energy utilization ratio of the in situ conversion process.

However, once conductive heating raises low-temperature zones sufficiently to induce thermal fracturing, steam rapidly penetrates and heats these regions, converting them into high-permeability pathways. This dynamic process enables the progressive transformation of low-temperature zones into thermally productive areas.

(a) **Model 1**

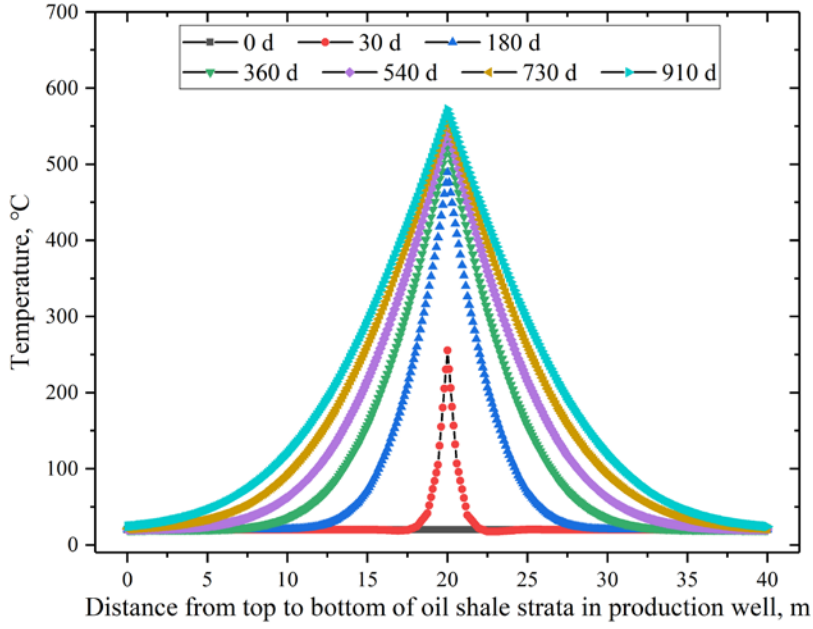

(b) **Model 2**

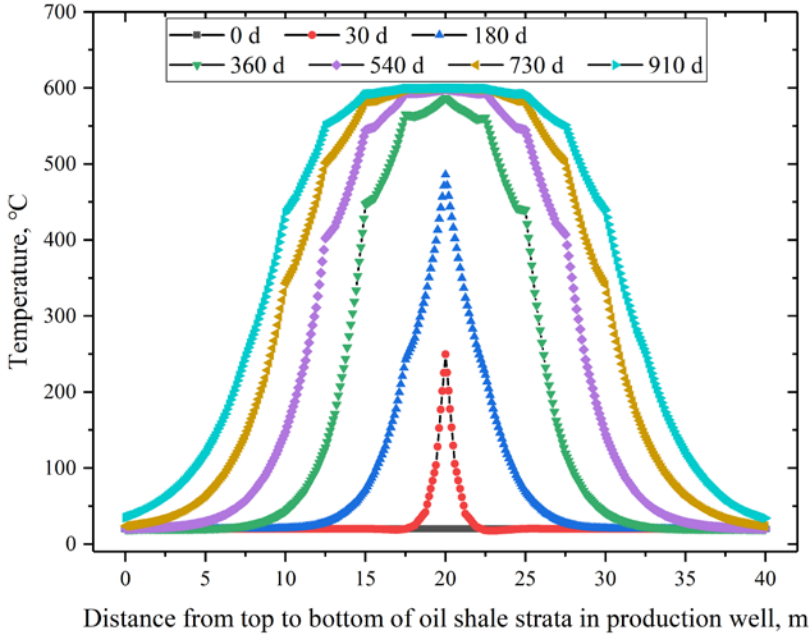

(c) **Model 3**

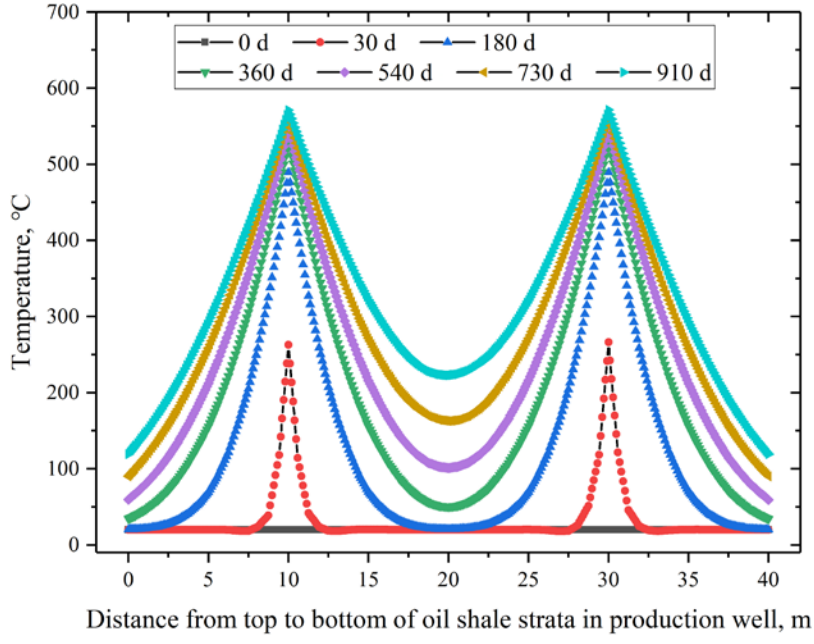

(d) **Model 4**

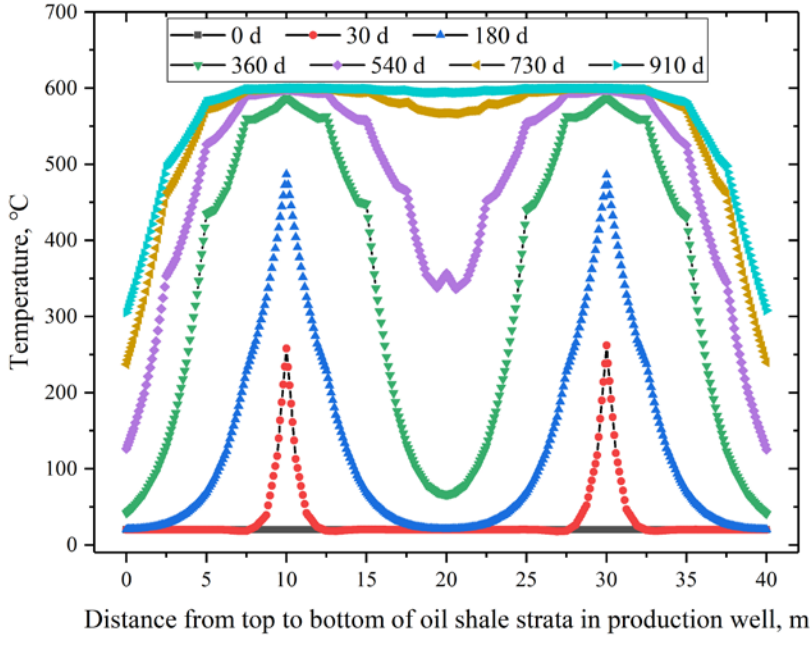

Fig. 7. Temperature distribution of the oil shale layer in the production well at different heating times.

3.2. Variation patterns of R_P and R_E with heating time

Hydrocarbon production and oil yield are critical process parameters for in situ thermal recovery of oil shale. Figure 8 illustrates the cumulative and daily hydrocarbon production curves of different models as a function of heating time. The results indicate that, under identical well patterns, well spacing, injection temperatures, and steam pressures, the hydrocarbon production trends of the models exhibit distinct characteristics.

Model 1 contains only a single hydraulic fracture and does not account for the influence of thermally induced weak-plane evolution into interconnected fractures on steam flow. As shown in Figure 8(a), during the initial heating stage, Model 1 achieves an average daily production of 36.92 t. This is attributed to the rapid heating of the oil shale adjacent to the fracture by high-temperature steam. However, as heating progresses, daily production declines sharply, dropping to 18.95 t by day 200 and further to below 14.6 t after 500 days. Cumulative production reaches 3053 t within the first 100 days, 10 054 t by day 500, and 16 231 t by day 1000, with a continuously decreasing growth rate. This phenomenon arises because the permeability of the rock surrounding the injection well increases due to thermal stimulation, creating a high-temperature zone. However, the absence of additional large-scale steam pathways restricts heat transfer primarily to conduction near the fracture, limiting the expansion of the heated region.

Model 3, which incorporates an additional hydraulic fracture, exhibits a similar trend but significantly higher production. The initial daily production reaches 59.3 t, declining to 28.57 t by day 200 and below 19.08 t after 500 days. By day 1000, cumulative production reaches 23 428 t, surpassing that of Model 1 in both daily and cumulative output.

Models 2 and 4 consider the evolution of weak planes into interconnected fractures under thermal stress, resulting in more complex production dynamics. Initially, the presence of hydraulic fractures leads to high daily production (33.10 t for Model 2 and 55.24 t for Model 4), which decreases by day 100 (19.47 t and 33.13 t, respectively) as pyrolysis near the initial fractures completes and new fracture networks develop. By day 200, thermally induced fractures form, allowing steam to penetrate deeper regions and temporarily boosting production. This cyclic process sustains relatively high production levels over extended periods, which is advantageous for industrial operations. However, after 600 days, production declines as a high-permeability thermal zone develops between wells, diverting steam flow and reducing the contribution of newly formed fractures.

(a) **Model 1**

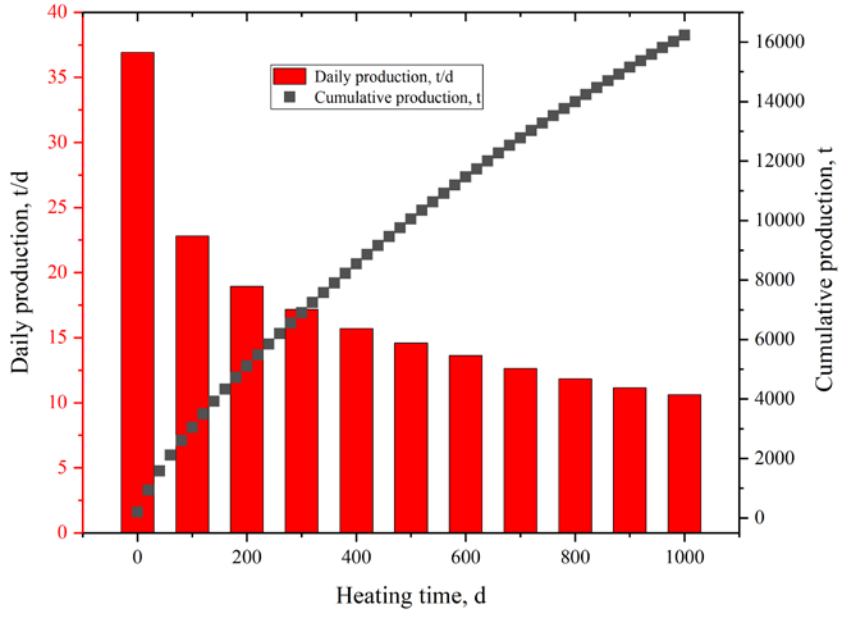

(b) **Model 2**

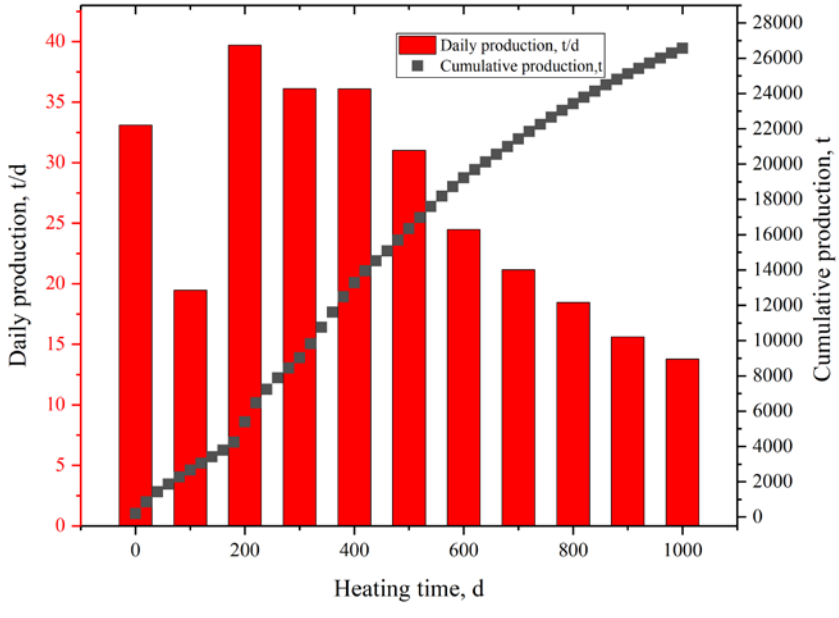

(c) **Model 3**

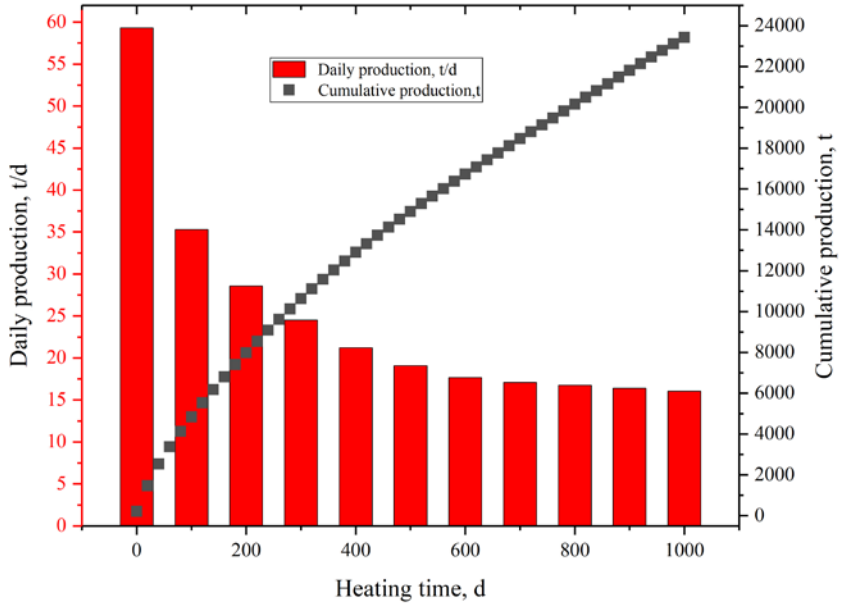

(d) **Model 4**

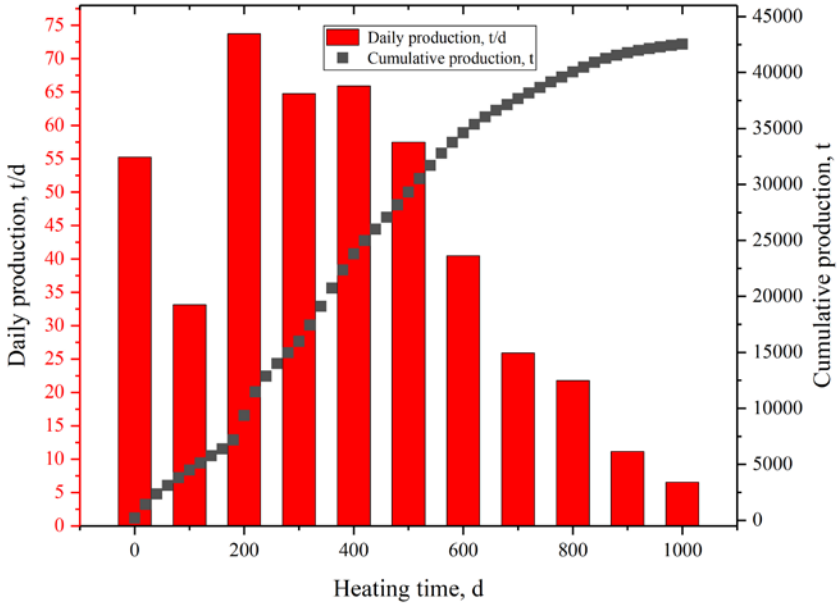

Fig. 8. Variation of oil shale oil and gas production with heating time.

Figure 9 presents the variation curves of oil yield with heating time for different models. As shown in Figure 9, when the heating duration is within 200 days, the differences in oil yield among the various models remain relatively small, all below 20%. However, when the heating time exceeds 200 days, significant discrepancies in oil yield begin to emerge.

For Model 1, the oil yield increases gradually with prolonged heating time, reaching only 34.5% after 100 days. The differences between Models 2 and 3 remain minimal throughout the heating process. Model 2 contains only one hydraulic fracture but accounts for the influence of thermally induced weak plane evolution into interconnected fractures on vapor flow, whereas Model 3 incorporates two hydraulic fractures without considering weak plane effects. The minor difference in oil yield between Models 2 and 3 indicates that both models achieve essentially identical volumes of pyrolyzed zones after heating.

In Model 2, the weak planes have not yet developed into interconnected fractures between the injection and production wells during the initial heating stage, while Model 3 benefits from two pre-existing hydraulic fractures serving as vapor flow channels. This configuration results in Model 3 exhibiting slightly higher oil yield than Model 2 during early heating stages. However, after 400 days of heating, Model 2 surpasses Model 1 in oil yield. Notably, none of Models 1, 2, or 3 achieve 60% oil yield even after 1000 days of heating, indicating suboptimal utilization of oil shale resources.

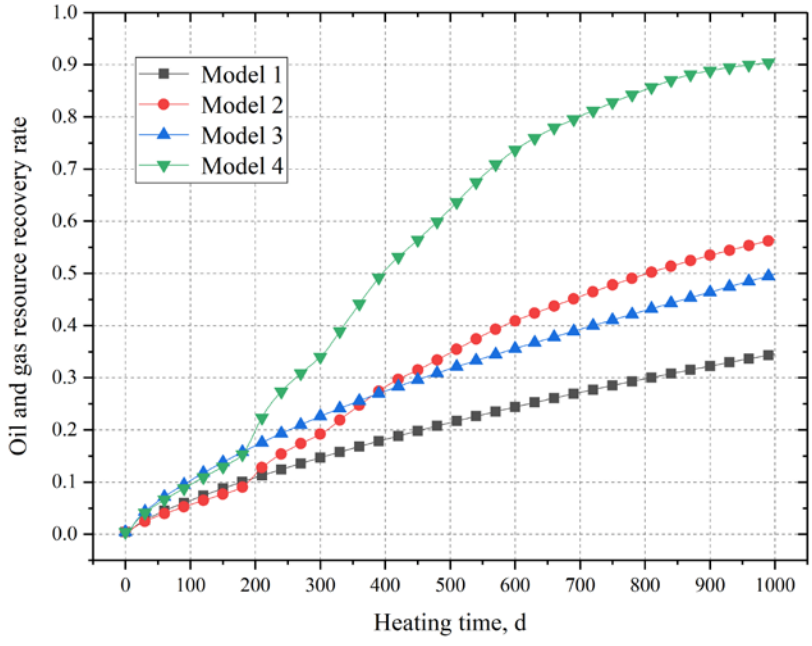

Fig. 9. Variation of oil yield by in situ steam injection with heating time.

In contrast, Model 4 maintains a high growth rate in oil yield during the first two years of heating, reaching 81.7% at the two-year mark and achieving 90.5% after 1000 days. The substantial improvement in oil yield achieved by Model 4 (which differs from Model 2 only by one additional hydraulic fracture) demonstrates that appropriately increasing the number of initial fracture channels through staged fracturing can significantly enhance both oil/gas production and recovery efficiency during in situ oil shale thermal recovery operations.

3.3. Temporal variation of energy return rate in in situ steam injection for oil shale recovery

For the industrial-scale exploitation of oil shale, if a particular in situ extraction method fails to achieve favorable economic benefits, large-scale industrial application becomes unfeasible. This study employs the ERR as an indicator to evaluate the economic viability of in situ steam injection for oil shale recovery. Figure 10 illustrates the variation of the ERR with heating time under four different models.

As shown in Figure 10, when steam is used as the heat-carrying medium, a high ERR can be achieved in the early stages of heating, whereas Shell's electrical heating technology requires a prolonged preheating period before oil production begins. This indicates that steam heating technology can deliver economic benefits at an earlier stage.

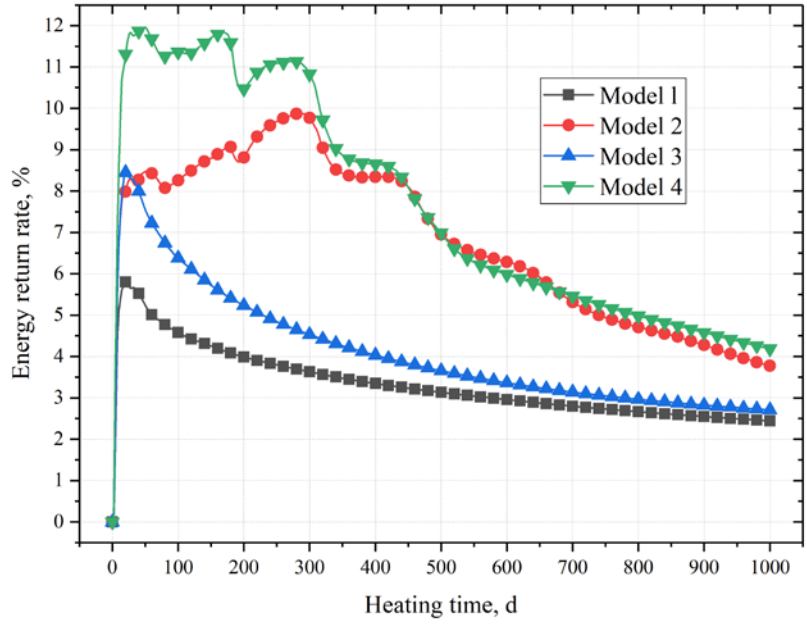

Fig. 10. Energy return rate of in situ steam injection for oil shale recovery as a function of heating time.

The ERR trends vary significantly among the different models. Models 1 and 3 do not account for the influence of thermally induced weak planes evolving into interconnected fractures on steam flow. In these models, the ERR peaks shortly after heating begins, reaching 5.79 and 8.44, respectively. However, as heating continues, the ERR gradually declines. This is because, in the initial phase, the pre-existing hydraulic fractures provide pathways for steam flow, allowing rapid heating and pyrolysis of oil shale near the fractures, thereby enhancing hydrocarbon production. Over time, the oil shale adjacent to the fractures is fully pyrolyzed, while regions farther away lack efficient steam channels, relying solely on slow thermal conduction. Consequently, hydrocarbon production decreases, leading to a continuous decline in the ERR.

Although Model 3 incorporates an additional hydraulic fracture compared to Model 1, its peak ERR is only 1.46 times that of Model 1. This is because, under identical well configurations, injection temperatures, and steam pressures, increasing the number of fractures also raises steam flow rates (as shown in Figure 11), thereby increasing energy input. As a result, the ERR does not improve proportionally with the number of fractures.

Models 2 and 4 consider the evolution of weak planes into interconnected fractures under thermal effects, with the only difference being that Model 2 has one hydraulic fracture while Model 4 has two. The ERR trends for these two models exhibit high similarity. Within the first year of heating,

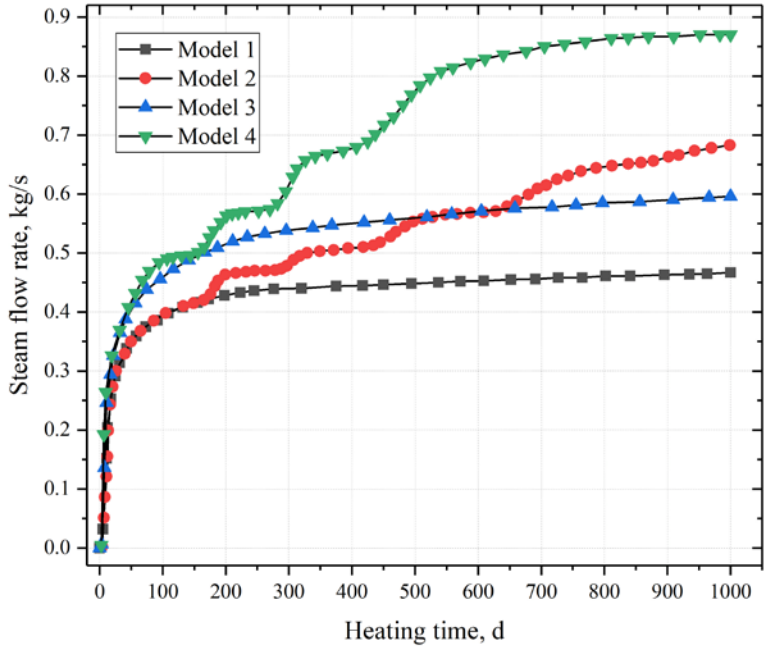

Fig. 11. Variation of steam flow rate as a function of heating time.

the ERR fluctuates significantly. These fluctuations occur because newly formed fractures connecting the injection and production wells allow high-temperature steam to rapidly penetrate and heat adjacent oil shale, leading to transient increases in the ERR as pyrolysis occurs. This cyclic process results in oscillatory behavior in the ERR. After one year, the ERR for both models begins to decline steadily without further fluctuations.

Considering the construction, operation, and maintenance costs of the entire extraction system, this study defines an ERR threshold of 5 for economically viable production. Models 1, 2, 3, and 4 fall below this threshold after 60, 740, 228, and 794 days of heating, respectively. The addition of a second fracture in Model 3 extends the viable production period by 168 days compared to Model 1, demonstrating that increasing fracture density can prolong production when thermal fracture evolution is negligible. However, Model 4 shows only marginal improvement over Model 2, indicating that when thermally activated fractures dominate flow pathways, the influence of additional hydraulic fractures on the ERR becomes negligible. Nevertheless, as seen in Figure 9, the number of fractures significantly impacts oil recovery efficiency.

4. Conclusions

This study investigates the spatiotemporal evolution of temperature fields during in situ steam injection for oil shale exploitation based on an anisotropic THM (thermo-hydro-mechanical) coupled mathematical model, while analyzing the variations in oil/gas production, oil recovery rate, and energy return rate with heating duration. The key findings are summarized as follows:

1. The evolution of thermally activated fractures from pre-existing weak planes plays a pivotal role in enhancing heating efficiency during in situ steam injection. These fractures facilitate alternating convection–conduction heating modes, enabling vertical expansion of high-temperature zones and achieving 90.5% oil recovery after 1000 days. In contrast, models relying solely on initial hydraulic fractures exhibit limited heating (< 60% recovery) due to restricted steam pathways.
2. Daily oil/gas production declines rapidly in models without fracture evolution (e.g., from 36.92 t/d to 14.6 t/d in Model 1), whereas models incorporating weak plane activation sustain higher yields by forming new steam flow channels. Notably, doubling hydraulic fractures (Model 3 vs. Model 1) improves cumulative production by 44%, highlighting the importance of initial fracture design.
3. Energy return rates (ERR) demonstrate divergent trends: models excluding fracture evolution exhibit early peaks (ERR = 5.79–8.44) followed by exponential decay, while models with weak plane activation maintain ERR > 5 for over a year. However, doubling hydraulic fractures only

marginally increases peak ERR (1.46×), emphasizing the trade-off between steam input and recovery gains.

4. Field applications should prioritize hydraulic fracturing to create interconnected fracture networks while leveraging natural weak planes to maximize convective heating. This dual strategy optimizes both technical performance (recovery > 90%) and economic viability (sustained ERR), offering a scalable solution for deep oil shale exploitation.

Data availability statement

The datasets generated and/or analyzed during this study are available from the corresponding author upon reasonable request.

Acknowledgments

This study was supported by the Open Fund of the State Center for Research and Development of Oil Shale Exploitation, the Basic Research Program of Shanxi Province (grant No. 20210302123177), and the National Key Research and Development Program of China (grant No. 2019YFA0705501). We acknowledge the use of Deep Seek for language editing and proofreading of this manuscript. AI assistance was used to improve grammar, clarity, and readability. All intellectual contributions, data interpretation, and conclusions remain the sole responsibility of the authors. The publication costs of this article were partially covered by the Estonian Academy of Sciences.

References

1. Guo, W., Pan, J., Yang, Q., Li, Q., Deng, S., Zhu, C. Study of the residual carbon oxidation trigger mechanism in fractured oil shale formation under real condition. *International Communications of Heat and Mass Transfer*, 2025, **160**, 108369. https://doi.org/10.1016/j.icheatmasstransfer.2024.108369
2. Yang, D., Wang, L., Zhao, Y., Kang, Z. Investigating pilot test of oil shale pyrolysis and oil and gas upgrading by water vapor injection. *Journal of Petroleum Science and Engineering*, 2021, **196**, 108101. https://doi.org/10.1016/j.petrol.2020.108101
3. Lei, Z., Zhang, Y., Yang, Z., Shi, Y., Zhang, H., Li, X. et al. Numerical simulation of oil shale in-situ exploration productivity comparison between steam injection and electrical heating. *Applied Thermal Engineering*, 2024, **238**, 121928. https://doi.org/10.1016/j.applthermaleng.2023.121928
4. Kang, Z., Zhao, Y., Yang, D. Review of oil shale in-situ conversion technology. *Applied Energy*, 2020, **269**, 115121. https://doi.org/10.1016/j.apenergy.2020.115121

5. Saif, T., Lin, Q., Gao, Y., Al-Khulaifi, Y., Marone, F., Hollis, D. et al. 4D *in situ* synchrotron X-ray tomographic microscopy and laser-based heating study of oil shale pyrolysis. *Applied Energy*, 2019, **235**, 1468–1475. https://doi.org/10.1016/j.apenergy.2018.11.044
6. Zhang, Y., Zhao, X., Wang, Q., Che, Y., Liu, H., Mu, R. et al. A study on the structures and primary reaction products of kerogens in Longkou oil shale with different densities through supercritical ethanolysis. *Journal of Molecular Structure*, 2024, **1309**, 138151. https://doi.org/10.1016/j.molstruc.2024.138151
7. Kibodeaux, K. R. Evolution of porosity, permeability, and fluid saturations during thermal conversion of oil shale. In *SPE Annual Technical Conference and Exhibition*, October 27–29, 2014, Amsterdam, The Netherlands. https://doi.org/10.2118/170733-ms
8. Xiao, H., Hu, T., Pang, X., Ding, C., Xu, Y., Zhang, S. et al. A novel method for identifying oil content and moveable thresholds in heterogeneous shales. *Fuel*, 2025, **397**, 135473. https://doi.org/10.1016/j.fuel.2025.135473
9. Li, Q., Wei, H., Zhang, Y., Han, L., Han, S., Ding, N. The variations on thermal conductivity and structures of silty clay modified by waste fly ash and oil shale ash after freeze–thaw cycles. *Construction and Building Materials*, 2020, **260**, 119954. https://doi.org/10.1016/j.conbuildmat.2020.119954
10. Wang, G., Yang, D., Liu, S., Fu, M., Wang, L. Experimental study on the anisotropic mechanical properties of oil shales under real-time high-temperature conditions. *Rock Mechanics and Rock Engineering*, 2021, **54**, 6565–6583. https://doi.org/10.1007/s00603-021-02624-7
11. Baqain, M., Neshumayev, D., Konist, A. TG-MS analysis and kinetic study of co-combustion of ca-rich oil shale with biomass in air and oxy-like conditions. *Carbon Capture Science & Technology*, 2024, **10**, 100162. https://doi.org/10.1016/j.ccst.2023.100162
12. Huang, H. W., Yu, H., Xu, W. L., Lyu, C. S., Micheal, M., Xu, H. Y. et al. A coupled thermo-hydro-mechanical-chemical model for production performance of oil shale reservoirs during in-situ conversion process. *Energy*, 2023, **268**, 126700. https://doi.org/10.1016/j.energy.2023.126700
13. Liu, Y., Xue, L., Ma, J., Peng, C., Bai, F., Li, Y. et al. Three-dimensional numerical simulation, energy efficiency and economic benefit estimation of oil shale in situ pyrolysis process. *Geoenergy Science and Engineering*, 2023, **227**, 211804. https://doi.org/10.1016/j.geoen.2023.211804
14. Kang, Z., Xie, H., Zhao, Y., Zhao, J. The feasibility of in-situ steam injection technology for oil shale underground retorting. *Oil Shale*, 2020, **37**(2), 119–139. https://doi.org/10.3176/oil.2020.2.03
15. Wang, G., Liu, S., Yang, D., Fu, M. Numerical study on the in-situ pyrolysis process of steeply dipping oil shale deposits by injecting superheated water steam: a case study on Jimsar oil shale in Xinjiang, China. *Energy*, 2022, **239**, 122182. https://doi.org/10.1016/j.energy.2021.122182
16. Zhang, Z., Montilla, M. J. B., Xie, Z., Li, S., Hu, Y., Li, X. Comparative analysis of wellbore electrical heating, low-frequency heating, and steam injection for

in-situ conversion in continental shale oil reservoirs. *Case Studies in Thermal Engineering*, 2024, **64**, 105512. https://doi.org/10.1016/j.csite.2024.105512

17. Zhu, J., Yi, L., Yang, Z., Li, X. Numerical simulation on the in situ upgrading of oil shale reservoir under microwave heating. *Fuel*, 2021, **287**, 119553. https://doi.org/10.1016/j.fuel.2020.119553
18. Zhu, J., Yi, L., Yang, Z., Duan, M. Three-dimensional numerical simulation on the thermal response of oil shale subjected to microwave heating. *Chemical Engineering Journal*, 2021, **407**, 127197. https://doi.org/10.1016/j.cej.2020.127197
19. Lou, X., Wang, J., Liu, H. Numerical simulation on in-situ modification of oil shale electric heating based on off-grid photovoltaic power supply. *Renewable Energy*, 2025, **242**, 122511. https://doi.org/10.1016/j.renene.2025.122511
20. Tian, W., Xu, R., Zeng, K., Chen, J., Yu, R., Jiang, P. Energy evolution during in-situ conversion of low-maturity shales. *Energy*, 2025, **317**, 134593. https://doi.org/10.1016/j.energy.2025.134593
21. Zheng, S., Liu, B., Mohammadian, E., Liu, Y., Tian, S. Sustainable in-situ steam injection approach for shale oil extraction in Xinjiang, China: a technical and economic analysis. *Energy*, 2024, **308**, 132986. https://doi.org/10.1016/j.energy.2024.132986
22. Zhang, Z., Montilla, M. J. B., Li, S., Xu, T., Li, Y., Xie, Z. et al. Evaluating heating strategies for efficient in-situ shale oil conversion: a numerical approach using THC coupled modeling. *Applied Thermal Engineerin*g, 2025, **270**, 126203. https://doi.org/10.1016/j.applthermaleng.2025.126203
23. Salimzadeh, S., Paluszny, A., Nick, H. M., Zimmerman, R. W. A three-dimensional coupled thermo-hydro-mechanical model for deformable fractured geothermal systems. *Geothermics*, 2018, **71**, 212–224. https://doi.org/10.1016/j.geothermics.2017.09.012
24. Wang, G., Yang, D., Kang, Z., Zhao, J., Lv, Y. Numerical investigation of the in situ oil shale pyrolysis process by superheated steam considering the anisotropy of the thermal, hydraulic, and mechanical characteristics of oil shale. *Energy & Fuels*, 2019, **33**(12), 12236–12250. https://doi.org/10.1021/acs.energyfuels.9b02883
25. Wang, G., Yang, D., Zhao, Y., Kang, Z., Zhao, J., Huang, X. Experimental investigation on anisotropic permeability and its relationship with anisotropic thermal cracking of oil shale under high temperature and triaxial stress. *Applied Thermal Engineering*, 2019, **146**, 718–725. https://doi.org/10.1016/j.applthermaleng.2018.10.005
26. Zhang, Y., Wang, L., Yang, D., Kang, Z., Zhao, J., Huang, X. et al. CT imaging to study meso-structure evolution of fractured oil shale during in-situ pyrolysis by high-temperature water vapor injection. *Geoenergy Science and Engineering*, 2024, **241**, 213104. https://doi.org/10.1016/j.geoen.2024.213104
27. Huang, X., Kang, Z., Zhao, J., Wang, G., Zhang, H., Yang, D. Experimental investigation on micro-fracture evolution and fracture permeability of oil shale heated by water vapor. *Energy*, 2023, **277**, 127677. https://doi.org/10.1016/j.energy.2023.127677

28. Huang, X., Yang, D., Wang, G., Zhang, K., Zhao, J. Evolution patterns and anisotropic connectivity characteristics of pores and fissures in oil shale after steam heating at different temperatures. *Natural Resources Researc*h, 2024, **34**, 409–425. https://doi.org/10.1007/s11053-024-10406-5
29. Huang, X., Yang, D., Kang, Z. Three-phase segmentation method for organic matter recognition in source rocks via CT images: a case study on oil shale pyrolyzed by steam. *Energy & Fuels*, 2021, **35**(12), 10075–10085. https://doi.org/10.1021/acs.energyfuels.1c00917
30. Yang, D., Zhao, Y., Kang, Z. Numerical simulation of in situ exploitation of oil shale by injecting high-temperature steam. *Oil Shale*, 2019, **36**(4), 483–500. https://doi.org/10.3176/oil.2019.4.03

Oil Shale, 2026, 43, 2, 228–240 https://doi.org/10.3176/oil.2026.2.05

Methylation of kukersite kerogen – estimation of the content of free hydroxyl groups

Kristi Rõuk[(a)]*, Mariliis Kimm[(a)], Kristiina Kaldas[(a)], Ivo Heinmaa[(b)], Tõnis Pehk[(b)], Estelle Silm[(a)], Margus Lopp[(a)]

[(a)] Industrial Chemistry Laboratory, Department of Chemistry and Biotechnology, School of Science, Tallinn University of Technology, Ehitajate tee 5, 19086 Tallinn, Estonia

[(b)] National Institute of Chemical Physics and Biophysics, Akadeemia tee 23, 12618 Tallinn, Estonia

Received 25 October 2025, accepted … 2026, available online … 2026

Abstract. *Derivatization of the kerogen backbone changes its chemical reactivity profile. In this study, kukersite kerogen was methylated with dimethyl carbonate. The substance was analyzed before and after processing by Fourier transform infrared spectroscopy, ^{13}C cross-polarization/magic angle spinning nuclear magnetic resonance spectroscopy, and elemental analysis. It was observed that kukersite kerogen can be readily methylated with dimethyl carbonate. Based on mass balance and the Lille-Blokker model, an average of 19 methyl groups were added to the kerogen unit. It was concluded that about half of the hydroxyl groups in Estonian kukersite kerogen are "free" and accessible to methylation.*

Keywords: *kukersite, kerogen, methylation, hydroxyl group, dimethyl carbonate, FTIR, NMR.*

1. Introduction

Kukersite is a sedimentary rock found in northern Estonia that contains about 30–50% of organic matter called kerogen [1, 2]. Throughout the 20th century, kukersite was mainly used for energy production through combustion and for oil extraction via thermal cracking [3]. However, it is now widely accepted that the traditional uses of oil shale have exhausted their potential and fail to meet contemporary environmental and efficiency standards. Instead, kukersite could be used as a versatile source of organic matter and various chemical structures.

* Corresponding author, kristi.rouk@taltech.ee

It is generally accepted that Estonian kukersite, formed during the Ordovician period over 450 million years ago, originates from colonies of *Gloeocapsomorpha prisca* which were rich in resorcinolic units [4]. Building on this, Lille proposed in 1999 that the resorcinolic units form the structural backbone of kukersite kerogen [5]. Two structural models of kerogen have since been independently proposed by Blokker et al. [6] and Lille et al. [1, 7]. More recently, a new model based on the Lille model was developed by Chu et al. (here Lille–Chu model) [8] and a generalized Lille–Blokker model, which integrates elements of both original frameworks, was proposed by our group [9]. However, the number of free hydroxyl groups per kerogen unit is not exactly defined in any of these models. The content of free hydroxyl groups is 24% in the Blokker model [6], 43% in the Lille model [1, 7], 47% in the Lille–Chu model [8], and 50% in the generalized Lille–Blokker model [9]. Yet, the hydroxyl group is a crucial functionality that strongly influences the chemical properties and reactivity of kukersite kerogen. Thus, the information regarding the amount of free hydroxyl groups in kukersite is essential.

Such knowledge may be obtained through the chemical alteration of kerogen, examined in a recent review [10]. However, few papers investigate the chemical reactions of kukersite kerogen systematically. In contrast, this topic has been extensively studied in lignin, a wood-derived biopolymer [11–13], and other natural materials [14–16]. Given the structural similarities between lignin and kerogen, such as shared functional groups and low solubility [17, 18], lignin studies may offer valuable insights for kerogen derivatization.

Alkylation, particularly methylation, is one of the most common chemical reactions for protecting hydroxyl groups. This has been extensively studied

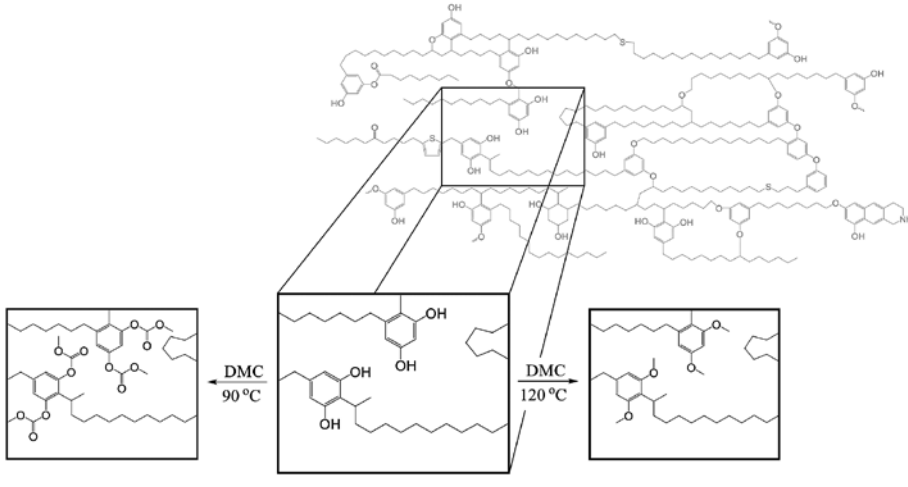

Fig. 1. Treating kerogen with dimethyl carbonate (DMC) could result in methoxycarbonylation at 90 °C and methylation at 120 °C or higher [25].

in lignin, employing methylating agents such as alkyl halides [19], dimethyl sulfate [20], trimethyl phosphate [21], and dimethyl carbonate [22, 23]. However, only one attempt to alkylate kukersite kerogen has been reported [24].

In this paper, we present our work on the methylation of kerogen using an eco-friendly methylating agent, dimethyl carbonate (DMC). DMC has dual reactivity: at 90 °C, it methoxycarbonylates hydroxyl groups, whereas at 120 °C and above, methylation occurs [25]. Kukersite was subjected to both reaction conditions (see Fig. 1). The resulting derivatized kerogen was analyzed by using Fourier transform infrared spectroscopy (FTIR), ^{13}C cross-polarization/magic angle spinning nuclear magnetic resonance spectroscopy (^{13}C CP MAS NMR), and elemental analysis. The number of free hydroxyl groups in a kerogen fragment was quantitatively estimated based on the Lille–Blokker model.

2. Materials and methods

2.1. Materials

All experiments were carried out on kukersite kerogen concentrate powder (91.3% kerogen content, particle size ≥ 45 μm), obtained from the Oil Shale Competence Center in Kohtla-Järve, Estonia. The material was dried at 105 °C to constant mass before use. Additional details regarding the preparation method of the kerogen concentrate are available in an article previously published by our research group [26]. All other chemicals were used as purchased without any further treatment or purification.

2.2. Experimental procedures

2.2.1. Methylation of kerogen: general procedure

The methylation method of Sen et al. [22] was applied with slight modifications.

The reactions were carried out in a 100 mL pressure reactor (stainless steel 4566C, Parr Instrument Company, Moline, Il, USA).

To the reactor with 1.0 g of kerogen and solid 0.5 g of NaOH (12.5 mmol), 25 mL of DMC (297.8 mmol) was added. The reactor was heated to 200 °C under a nitrogen atmosphere while stirring at 250 rpm. The reaction time was measured from the moment the temperature reached 190 °C. After a defined reaction time (5 h and 24 h), the reactor was cooled to room temperature, depressurized, and the liquid phase was separated by centrifugation. To the remaining solid phase, 50 mL of a 1:2 acetone–water mixture was added, and the mixture was centrifuged. This washing step was repeated three times until the pH reached 6–7, and the solid was dried to constant mass.

2.2.2. Methylation of kerogen: quantitative procedure

To the reactor with 1.000 g of kerogen and 0.5 g of NaOH (12.5 mmol), 25 mL of DMC (297.8 mmol) was added. The reaction mixture was heated to 200 °C under a nitrogen atmosphere while stirring at 250 rpm for 24 h. Then the reactor was cooled to room temperature, depressurized, and the phases were separated by centrifugation. The liquid phase was orange-brown in color. It was suggested that the kerogen slightly degraded at 200 °C and the resulting organic matter leached to the liquid phase.

The solid phase was washed with 4 × 15 mL DMC and separated by centrifugation. The combined liquid phases were concentrated to yield 33.2 mg of dark brown oil. The solid phase was further washed with 4 x 50 mL of distilled water, until the pH reached 6–7, and separated by centrifugation. To minimize the loss of methylated product, the liquid phase was additionally filtered when necessary. The obtained solid mass and the oily mass from DMC extraction were combined and dried to constant mass on a rotary evaporator, yielding 1.043 g of methylated kerogen.

2.2.3. Methoxycarbonylation of kerogen

To the pressure reactor with 1.0 g of kerogen and 0.5 g of NaOH (12.5 mmol), 25 mL of DMC (297.8 mmol) was added. The reaction mixture was heated to 90 °C under a nitrogen atmosphere while stirring at 250 rpm for 24 h. Then the reactor was cooled to room temperature and depressurized. The reaction mixture was filtered, and the obtained solid was sequentially washed with distilled water, ethanol, and diethyl ether. Finally, it was dried under vacuum to constant mass.

2.3. Analytical methods

The FTIR spectra were recorded on an IRTracer-100 FTIR spectrophotometer (Shimadzu, Japan). Transmission spectra (KBr pellets with kerogen 100:1) were measured in the range 400–4000 cm^{-1} with a resolution of 2 cm^{-1} by accumulating 30 scans. The same parameters were used in attenuated total reflectance mode.

^{13}C CP MAS NMR spectra were recorded on a Bruker AVANCE-II spectrometer at a 14.1 T magnetic field using a home-built double resonance magic-angle-spinning probe for 4 × 25 mm Si_3N_4 rotors. The spinning speed of the sample was set to 12.5 kHz with an ordinary cross-polarization (CP) pulse sequence, where the duration of the ramped polarization transfer pulse was 2 ms, and the relaxation delay between the excitations was 5 s. The intensities in the spectra were normalized to the weight of the sample and to the number of accumulations.

The CHNS elemental analysis was conducted with an Elementar vario MICRO cube.

3. Results and discussion

3.1. FTIR spectra

FTIR spectra of the kukersite kerogen concentrate powder were recorded using both transmission and attenuated total reflectance (ATR) modes. The obtained spectra were similar and closely resembled those reported by Derenne et al. [27, 28] and Blokker et al. [6]. Although the ATR technique yields weaker signals, it was selected for subsequent measurements due to its simplicity and lower sensitivity to moisture, which enables more accurate monitoring of changes in hydroxyl peak intensity.

Methylated kerogen was prepared according to the general procedure. FTIR spectra were recorded for samples of initial kerogen (a), and methylated kerogen from 5 h (b) and 24 h (c) reactions (Fig. 2). Considerable differences were observed in the spectra of the methylated samples compared to the initial kerogen. Most importantly, in spectrum (b), the characteristic absorption band at 3400 cm^{-1}, corresponding to hydroxyl groups, had significantly diminished. Additionally, a decrease in the bands at 1350 cm^{-1} and 1020 cm^{-1} was observed, further confirming the loss of hydroxyl groups. A new band at 1265 cm^{-1}, attributed to the newly formed phenyl methyl ether bonds, was also noted. In addition, a symmetric C–H stretching band characteristic of methoxy

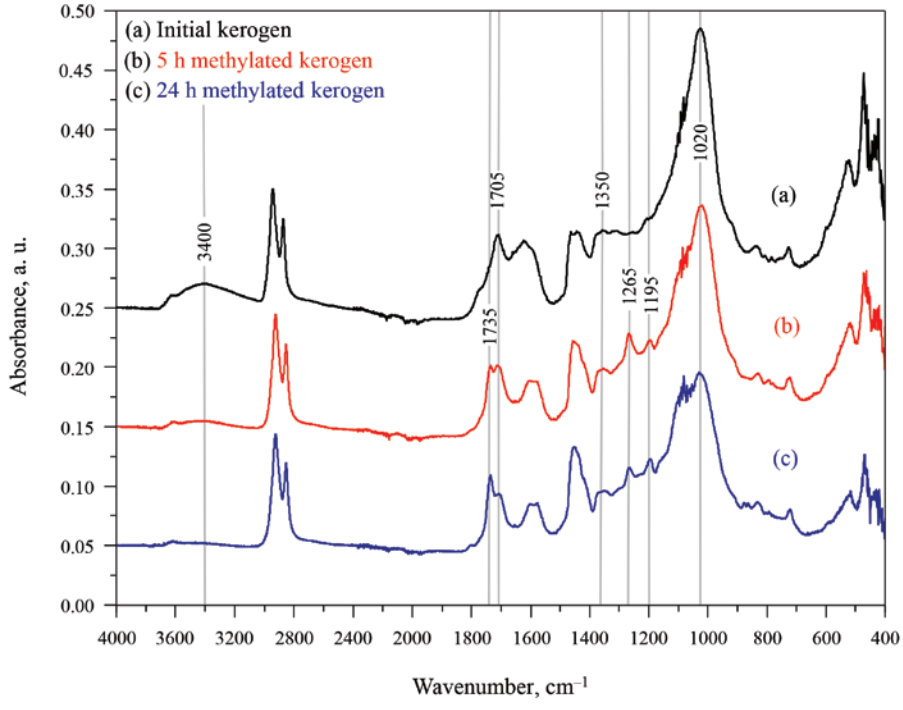

Fig. 2. ATR-FTIR spectra of Estonian kukersite kerogen concentrate measured before, after 5 h, and after 24 h of methylation.

groups at 2840–2820 cm^{-1} and an aliphatic C–O stretching band at 1050–1010 cm^{-1} were expected [29]. However, those bands were likely masked by the relatively more intense bands of the kerogen structure. Similarly, the band at 1705 cm^{-1}, corresponding to carboxyl and carbonyl groups, had slightly decreased in both spectra, and new bands appeared in the 1735 cm^{-1} and 1195 cm^{-1} regions, which may correspond to the formation of aliphatic esters. These changes were even more pronounced in spectrum (c).

Titration data reported by Aarna and Lippmaa [24] suggest that one kerogen "molecule" contains ~0.8 carboxyl groups. Therefore, the ester bands may correspond to the esterified native carboxyl groups. However, the methoxycarbonylation of kerogen could also account for these absorption bands. This theory was tested in a separate experiment, further discussed in the next paragraph. Another possible explanation for the appearance of these bands is degradation of the kerogen structure, which may lead to side reactions and the formation of methyl esters. While rapid kerogen degradation typically occurs at 320–340 °C, it can begin as early as 170–180 °C – well below our reaction temperature of 200 °C [30–32]. Indeed, the liquid phase of the reaction mixture had an orange-brown hue and, upon concentration, produced a small amount of brown, oily substance – likely resulting from degradation – which was not analyzed further. Beyond this observation, no further evidence of degradation was detected, suggesting that although some pyrolysis occurred, its extent was minimal and did not have a significant effect on the results. It may be concluded that ATR-FTIR is a simple and convenient method to track the methylation of kerogen and qualitatively estimate the depth of the process.

3.2. ^{13}C CP MAS NMR spectra

^{13}C CP MAS NMR spectra were recorded for both the initial Estonian kukersite kerogen concentrate and the 5 h and 24 h methylated samples (Fig. 3). It was observed that the spectra of the native Estonian kukersite kerogen resemble those reported by Derenne et al. [27] and Lille et al. [7]. Numerous signals were observed in the region of aliphatic carbon, with a maximum at 30 ppm. The signals at 75 ppm correspond to various non-aromatic carbons adjacent to oxygen atoms, such as oxy-methylene, oxy-methine, and oxy-quaternary carbons. In the region of aromatic carbons, a peak observed at 109 ppm is attributed to the carbons within an aromatic ring adjacent to an oxygen-bearing carbon. The peak at 141 ppm is assigned to aromatic carbons at branching, while the peak at 156 ppm is assigned to carbons within aromatic rings bearing oxygen substituents. The peak at 208 ppm belongs to carbonyl carbons. The asterisks denote the spinning sidebands from the main peaks at 156 and 141 ppm.

The integral number of aliphatic carbons accounts for 74% of the total carbon content, leaving 26% to aromatic carbons, with resorcinols as the main

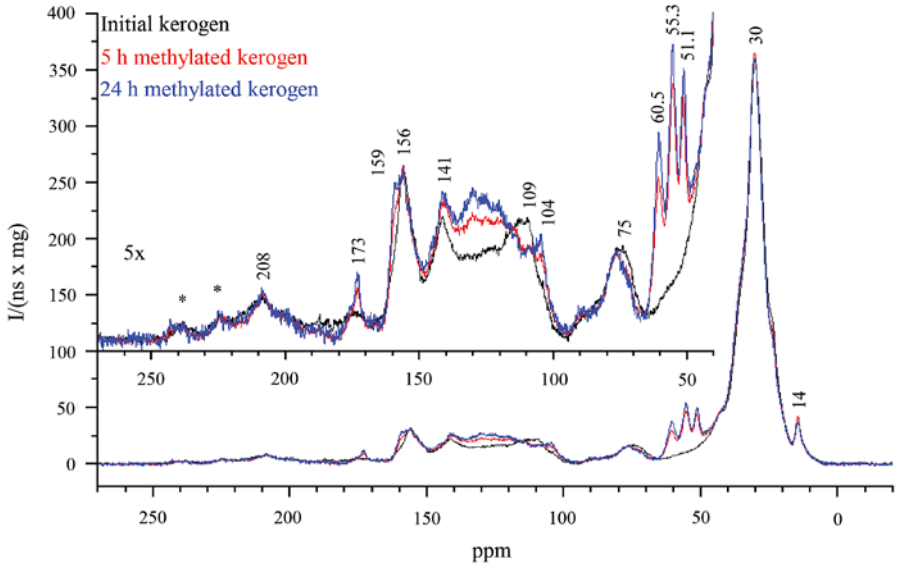

Fig. 3. ^{13}C CP MAS NMR spectra of Estonian kukersite kerogen before and after methylation.

aromatics in kerogen. The latter value is slightly higher than the estimate previously reported by Aarna and Lippmaa (19%) [24] and comparable to that of Lille et al. (24%) [33].

The spectra of 5 h and 24 h methylated kerogen show several changes compared to initial kerogen, which can be traced by calculating and comparing the chemical shifts for simple molecule models (Fig. 4). In the region of aliphatic carbons, three new peaks were observed at 51.1, 55.3, and 60.5 ppm, which should belong to the newly formed methoxy groups. Namely, the peak at 51.1 ppm may be assigned to methylated aliphatic and non-hindered aromatic carboxyl groups, and the peaks at 55.3 and 60.5 ppm to the methylated resorcinolic hydroxyl groups. Specifically, the peak at 55.3 ppm corresponds to sterically unhindered methoxy groups, whereas the peak at 60.5 ppm arises from methoxy groups that are sterically hindered due to ortho-disubstitution on the aromatic ring.

In the region of aromatic carbons, we noticed that the peak at 104 ppm had grown, while the peak at 109 ppm had diminished. In addition, a new shoulder for the peak at 156 ppm, denoting methoxy-substituted aromatic carbons, had appeared at 159 ppm. Both changes can be attributed to the changes in the chemical environment brought on by the added methyl groups. The peak at 173 ppm, initially assigned to carboxyl carbons, had also grown, possibly due to the formation of esters.

The 24 h methylated kerogen spectrum shows the same changes that were observed for 5 h methylated kerogen; however, the peaks are slightly more

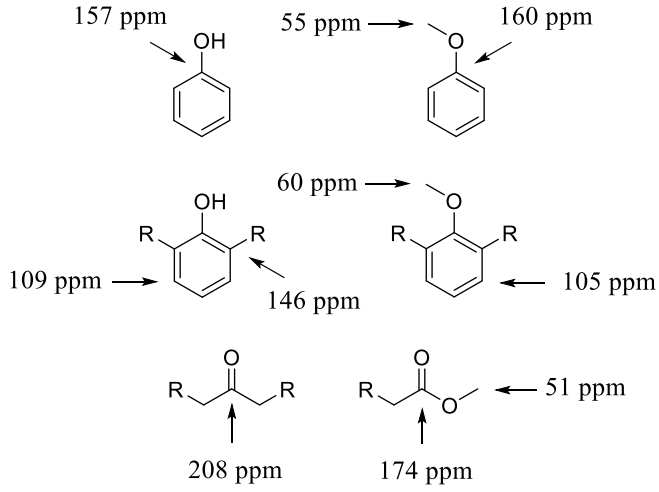

Fig. 4. Calculated chemical shifts of phenols and methylated phenols.

developed. This is a strong indication that the reaction has almost completed within 5 h and matured within 24 h. The NMR spectra also confirm the methylation of kerogen and indicate that both resorcinolic and acidic hydroxyl groups were methylated.

To elucidate the appearance of the methyl ester signals in both IR and NMR spectra, the possibility of kerogen methoxycarbonylation with dimethyl carbonate was investigated. In the product obtained after 24 h of heating at 90 °C, almost no changes were observed in the FTIR spectrum. The expected bands at 1750–1730 cm^{-1} and 1280–1240 cm^{-1} [34, 35] did not appear, and only a slight decrease of the hydroxyl band was observed. Similarly, the characteristic peaks of the methoxycarbonylated product at 157 and 55 ppm were absent from the NMR spectrum. The main changes observed were two sharp peaks at 172.1 and 167.7 ppm, along with a small bump at ~180 ppm, which could not be attributed to methoxycarbonylation.

The obtained results suggest that the methoxycarbonylation reaction proceeds only to a very small extent, if at all.

3.3. Elemental analysis

The elemental composition of the initial Estonian kukersite kerogen concentrate aligned relatively well with our previous measurements [26] as well as previously published results [36]. The elemental compositions of both the native and the methylated kerogens treated for 5 h and 24 h are presented in Table 1.

Table 1. Elemental composition of both native and methylated kerogens after 5 h and 24 h of treatment

	N, %	C, %	H, %	S, %
Native kerogen*	0.30 ± 0.01	66.42 ± 0.21	8.03 ± 0.09	1.41 ± 0.07
5 h methylated kerogen*	0.22 ± 0.01	67.78 ± 0.02	8.08 ± 0.05	1.35 ± 0.10
24 h methylated kerogen*	0.25 ± 0.01	71.03 ± 0.08	8.49 ± 0.01	0.97 ± 0.02

* Mean value of three measurements.

Compared to the elemental composition of the initial kerogen, the carbon and hydrogen contents of the 5 h methylated kerogen were markedly higher. The carbon content had increased by 1.36%, while the hydrogen content had increased by 0.05%. In the 24 h methylated kerogen sample, the carbon and hydrogen contents had increased even more, by 4.61% and 0.46%, respectively. These results are consistent with the changes we expected to occur during methylation.

3.4. Calculation of the number of hydroxyl groups in a kerogen molecule – comparison of the different kerogen structural models

Based on the assumption that the reaction had completed in 24 h, it is possible to calculate the number of hydroxyl groups per "molecule" of kerogen. However, all existing models – the Lille model [7], the Blokker model [6], the Lille–Chu model [8], and the Lille–Blokker model [9] – assign slightly different molecular masses to the kerogen "molecule": 6581 Da, 5312 Da, 5131 Da, and 5650 Da, respectively.

We obtained 1.043 g of methylated product from 1.000 g of starting material. The starting material, with a kerogen content of 91.3%, contained 0.913 g of organic matter and 0.087 g of inorganic matter. Assuming that the latter is inert, the treated sample contains 0.956 g of methylated kerogen. The added methyl groups (actual added mass of CH_2) have a molar mass of 14.027 g/mol. Thus, as shown in equation (1), the amount of added methyl groups is 3.044 mmol. The amount of initial kerogen, calculated using the molecular mass assigned by the Lille–Blokker model, is 0.162 mmol, and the number of methyl groups added to one kerogen "molecule" is 19.

$$n_{\mathrm{CH_3}} = \frac{m_{\mathrm{CH_3}}}{M_{\mathrm{CH_3}}} = \frac{0.956\ \mathrm{g} - 0.913\ \mathrm{g}}{(1 \times 12.011 + 2 \times 1.008)\ \mathrm{g/mol}} \times 1000 = 3.044\ \mathrm{mmol} \quad (1)$$

Similar calculations using the Lille, Blokker, and Lille–Chu models result in 22, 18, and 19 hydroxyl groups per kerogen "molecule," respectively (Table 2).

Table 2. Quantification of free hydroxyl groups: model vs. experimental

	Empirical formula	Free hydroxyl groups counted from the model	Free hydroxyl groups calculated from methylation data for the model
Blokker model	$C_{351}H_{548}O_{34}$	8	18
Lille model	$C_{420}H_{636}O_{44}S_4ClN$	19	22
Lille–Chu model	$C_{366}H_{548}O_{35}S_3ClN$	20	19
Lille–Blokker model	$C_{367}H_{567}NO_{35}S_3$	16	19

These results show that all four models slightly underestimate the number of free hydroxyl groups in kerogen. Moreover, approximately half of the oxygen atoms in the kerogen "molecule" are accessible to methylation. Given that there is only ~1 carboxyl group present per kerogen "molecule," its contribution to methyl group consumption is minimal. The content of "free" hydroxyl groups is quite well represented in the Lille, Lille–Chu, and Lille–Blokker models.

4. Conclusions

In this paper, we have demonstrated that kukersite kerogen can be readily and almost quantitatively methylated using dimethyl carbonate, an environmentally benign methylating agent. No evidence of relevant side reactions, namely methoxycarbonylation, was observed. The study also revealed that all existing structural models of kukersite kerogen might slightly underestimate the amount of free hydroxyl groups in kerogen. Our experiments showed that free hydroxyl groups account for nearly half of the oxygen atoms present in a kerogen "molecule." This selective methylation reaction of kerogen hydroxyl groups paves the way for further studies of other derivatization reactions and potential applications of kukersite derivatives in future valorization efforts.

Data availability statement

The authors confirm that the data supporting the findings of this study are contained within the article. Additional information and original spectra are available on request from the authors.

Acknowledgments

This work was co-funded by the European Union and the Estonian Research Council via project TEM-TA128, supported by the Ministry of Education and Research Centers of Excellence grant TK228 (Center of Excellence in the Circular Economy for Strategic Mineral and Carbon Resources), by Estonian Research Council grant PRG1702, and by Tallinn University of Technology. The authors also thank Angelika Närep and Kati Muldma for conducting elemental analysis measurements, and other colleagues at the Industrial Chemistry Laboratory, Tallinn University of Technology, for their support. The publication costs of this article were partially covered by the Estonian Academy of Sciences.

References

1. Lille, Ü. Current knowledge on the origin and structure of Estonian kukersite kerogen. *Oil Shale*, 2003, **20**(3), 253–263. https://doi.org/10.3176/oil.2003.3.03
2. Veiderma, M. Estonian oil shale – resources and usage. *Oil Shale*, 2003, **20**(3S), 295–303. https://doi.org/10.3176/oil.2003.3S.02
3. Oja, V., Suuberg, E. M. Oil shale processing, chemistry and technology. In *Encyclopedia of Sustainability Science and Technology* (Meyers, R. A., ed.). Springer, New York, NY, 2017, 1–38. https://doi.org/10.1007/978-1-4939-2493-6_102-3
4. Hutton, A. C. Organic petrography of oil shales. In *Composition, Geochemistry and Conversion of Oil Shales* (Sanpe, C., ed.). Vol. 455. Springer Netherlands, NATO ASI Series, Dordrecht, 1995, 17–33. https://doi.org/10.1007/978-94-011-0317-6_2
5. Lille, Ü. On the origin of 5-alkyl-1,3-benzenediols in the retort oil of Estonian kukersite. *Oil Shale*, 1999, **16**(3), 231–237. https://doi.org/10.3176/oil.1999.3.04
6. Blokker, P., van Bergen, P., Pancost, R., Collinson, M. E., de Leeuw, J. W., Sinninghe Damste, J. S. The chemical structure of *Gloeocapsomorpha prisca* microfossils: implications for their origin. *Geochimica et Cosmochimica Acta*, 2001, **65**(6), 885–900. https://doi.org/10.1016/S0016-7037(00)00582-2
7. Lille, Ü., Heinmaa, I., Pehk, T. Molecular model of Estonian kukersite kerogen evaluated by ^{13}C MAS NMR spectra. *Fuel*, 2003, **82**(7), 799–804. https://doi.org/10.1016/S0016-2361(02)00358-7
8. Chu, W., Cao, X., Schmidt-Rohr, K., Birdwell, J. E., Mao, J. Investigation into the effect of heteroatom content on kerogen structure using advanced ^{13}C solid-state nuclear magnetic resonance spectroscopy. *Energy Fuels*, 2019, **33**(2), 645–653. https://doi.org/10.1021/acs.energyfuels.8b01909
9. Mets, B., Kaldas, K., Uustalu, J. M., Lopp, M. The Lille-Blokker model – an excellent tool to describe the structure of kukersite. *Oil Shale*, 2023, **40**(3), 234–243. https://doi.org/10.3176/oil.2023.3.04

10. Lopp, M., Kaldas, K. Possibilities of the direct chemical transformation of kukersite kerogen: a critical review. *ACS Omega*, 2025, **10**(36), 40740–40749. https://doi.org/10.1021/acsomega.5c04675
11. Eraghi Kazzaz, A., Hosseinpour Feizi, Z., Fatehi, P. Grafting strategies for hydroxy groups of lignin for producing materials. *Green Chemistry*, 2019, **21**, 5714–5752. https://doi.org/10.1039/c9gc02598g
12. Laurichesse, S., Avérous, L. Chemical modification of lignins: towards biobased polymers. *Progress in Polymer Science*, 2014, **39**(7), 1266–1290. https://doi.org/10.1016/j.progpolymsci.2013.11.004
13. Suota, M. J., Kochepka, D. M., Ganter Moura, M. G., Pirich, C. L., Matos, M., Magalhães, W. L. E. et al. Lignin functionalization strategies and the potential applications of its derivatives – a review. *BioResources*, 2021, **16**(3), 6471–6511. https://doi.org/10.15376/biores.16.3.Suota
14. Elnaggar, E. M., Abusaif, M. S., Abdel-Baky, Y. M., Ragab, A., Omer, A. M., Ibrahim, I. et al. Insight into divergent chemical modifications of chitosan biopolymer: review. *International Journal of Biological Macromolecules*, 2024, **277**, 134347. https://doi.org/10.1016/j.ijbiomac.2024.134347
15. Jahani, A., Jazayeri, M. H. Tailoring cellulose: from extraction and chemical modification to advanced industrial applications. *International Journal of Biological Macromolecules*, 2025, **309**, 142950. https://doi.org/10.1016/j.ijbiomac.2025.142950
16. Haq, F., Yu, H., Wang, L., Teng, L., Haroon, M., Khan, R. U. et al. Advances in chemical modifications of starches and their applications. *Carbohydrate Research*, 2019, **476**, 12–35. https://doi.org/10.1016/j.carres.2019.02.007
17. Wang, Z., Deuss, P. J. The isolation of lignin with native-like structure. *Biotechnology Advances*, 2023, 68, 108230. https://doi.org/10.1016/j.biotechadv.2023.108230
18. Guo, L., Gao, Q., Ding, J., Xiong, Z., Chen, S., Li, X. et al. Lignin: dissolution, modification, and derived materials. *International Journal Biological Macromolecules*, 2025, **309**, 142748. https://doi.org/10.1016/j.ijbiomac.2025.142748
19. Beaudoin, D., Palus, E., Konduri, M. K. R., Gagné, A. Methylation of softwood and hardwood kraft lignins with chloromethane. *RSC Advances*, 2024, **14**(4), 2293–2299. https://doi.org/10.1039/D3RA08404C
20. Sadeghifar, H., Cui, C., Argyropoulos, D. S. Toward thermoplastic lignin polymers. Part 1. Selective masking of phenolic hydroxyl groups in kraft lignins via methylation and oxypropylation chemistries. *Industrial & Engineering Chemistry Research*, 2012, **51**(51), 16713–16720. https://doi.org/10.1021/ie301848j
21. Duval, A., Avérous, L. Mild and controlled lignin methylation with trimethyl phosphate: towards a precise control of lignin functionality. *Green Chemistry*, 2020, **22**(5), 1671–1680. https://doi.org/10.1039/C9GC03890F
22. Sen, S., Patil, S., Argyropoulos, D. S. Methylation of softwood kraft lignin with dimethyl carbonate. *Green Chemistry*, 2015, **17**(2), 1077–1087. https://doi.org/10.1039/C4GC01759E

23. Xiong, S.-J., Pang, B., Zhou, S.-J., Li, M.-K., Yang, S., Wang, Y.-Y. et al. Economically competitive biodegradable PBAT/lignin composites: effect of lignin methylation and compatibilizer. *ACS Sustainable Chemistry & Engineering*, 2020, **8**(13), 5338–5346. https://doi.org/10.1021/acssuschemeng.0c00789
24. Aarna, A. J., Lippmaa, E. T. О структуре керогена прибалтийского горючего сланца (On the structure of the Baltic oil shale kerogen). *Transactions of the Tallinn Polytechnic Institute, Series A*, 1955, **63**, 3–50.
25. Tundo, P., Selva, M. The chemistry of dimethyl carbonate. *Accounts of Chemical Research*, 2002, **35**(9), 706–716. https://doi.org/10.1021/ar010076f
26. Kaldas, K., Preegel, G., Muldma, K., Lopp, M. Wet air oxidation of oil shales: kerogen dissolution and dicarboxylic acid formation. *ACS Omega*, 2020, **5**(35), 22021–22030. https://doi.org/10.1021/acsomega.0c01466
27. Derenne, S., Largeau, C., Casadevall, E., Sinninghe Damsté, J. S., Tegelaar, E. W., de Leeuw, J. W. Characterization of Estonian kukersite by spectroscopy and pyrolysis: evidence for abundant alkyl phenolic moieties in an Ordovician, marine, type II/I kerogen. *Organic Geochemistry*, 1990, **16**(4–6), 873–888. https://doi.org/10.1016/0146-6380(90)90124-I
28. Derenne, S., Largeau, C., Landais, P., Rochdi, A. Spectroscopic features of *Gloeocapsomorpha prisca* colonies and of interstitial matrix in kukersite as revealed by transmission micro-FT-i.r.: location of phenolic moieties. *Fuel*, 1994, **73**(4), 626–628. https://doi.org/10.1016/0016-2361(94)90049-3
29. Smith, B. C. The C-O bond III: ethers by a knockout. *Spectroscopy*, 2017, **32**(5). https://www.spectroscopyonline.com/view/c-o-bond-iii-ethers-knockout (accessed 2025-10-24).
30. Kogerman, P., Luts, K., Hüsse, I. *The Chemistry of Estonian Oil Shale*. Goshimtexizdat, Moscow, Leningrad, 1934.
31. Tiikma, L., Zaidentsal, A., Tensorer, M. Formation of thermobitumen from oil shale by low-temperature pyrolysis in an autoclave. *Oil Shale*, 2007, **24**(4), 535–546. https://doi.org/10.3176/oil.2007.4.05
32. Shi, J., Ma, Y., Li, S., Wu, J., Zhu, Y., Teng, J. Characteristics of Estonian oil shale kerogen and its pyrolysates with thermal bitumen as a pyrolytic intermediate. *Energy & Fuels*, 2017, **31**(5), 4808–4816. https://doi.org/10.1021/acs.energyfuels.7b00054
33. Lille, Ü., Heinmaa, I., Müürisepp, A.-M., Pehk, T. Investigation of kukersite structure using NMR and oxidative cleavage: on the nature of phenolic precursors in the kerogen of Estonian kukersite. *Oil Shale*, 2002, **19**(2), 101–116. https://doi.org/10.3176/oil.2002.2.02
34. Smith, B. C. The C=O bond, part VI: esters and the rule of three. *Spectroscopy*, 2018, **33**(7). https://www.spectroscopyonline.com/view/co-bond-part-vi-esters-and-rule-three (accessed 2025-10-24).
35. Smith, B. C. The C=O bond, part VII: aromatic esters, organic carbonates, and more of the rule of three. *Spectroscopy*, 2018, **33**(9). https://www.spectroscopyonline.com/view/co-bond-part-vii-aromatic-esters-organic-carbonates-and-more-rule-three (accessed 2025-10-24).
36. Kogermann, P. N. *On the Chemistry of the Estonian Oil Shale Kukersite*. Tartu, 1931.

PUBLISHER
Estonian Academy Publishers
Kohtu 6
10130 Tallinn, ESTONIA
info@eap.ee
www.eap.ee

EDITORIAL OFFICE
Kohtu 6
10130 Tallinn, ESTONIA
hedi.tonso@eap.ee
www.eap.ee/oilshale

Subscription information is available at www.eap.ee/subscription

Subscription orders should be sent to subscription@eap.ee

ISBN 0208 189X (print)
ISSN 1736-7492 (electronic)